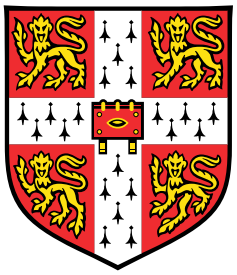

Motion of filaments induced by molecular motors: from individual to collective dynamics

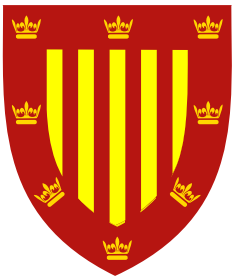

Gabriele De Canio

Department of Applied Mathematics and Theoretical Physics
University of Cambridge

This dissertation is submitted for the degree of
Doctor of Philosophy

Peterhouse

September 2018

To my parents,
with immense gratitude and all my love

"Considerate la vostra semenza:
fatti non foste a viver come bruti,
ma per seguir virtute e canoscenza."
(Consider well the seed that gave you birth:
you were not made to live as brutes,
but to follow virtue and knowledge.)
Dante Alighieri, Divina Commedia, Canto XXVI, vv. 112-120

Declaration

I hereby declare that except where specific reference is made to the work of others, the contents of this dissertation are original and have not been submitted in whole or in part for consideration for any other degree or qualification in this, or any other university. This dissertation is my own work and contains nothing which is the outcome of work done in collaboration with others, except as specified in the text and Acknowledgements.

Gabriele De Canio
September 2018

Acknowledgements

I believe that my time as a PhD student has been the most challenging, yet rewarding so far. I would like to express my gratitude to all those who have supported me during these years.

Above all, I would like to thank my supervisors Prof. Eric Lauga and Prof. Ray Goldstein, who helped and encouraged me during the hardest times. They have been an immense source of knowledge and inspiration over the years. It has been a pleasure working with them, exchanging ideas, and receiving their guidance. I am also very grateful to the whole Biophysics group for useful discussions and insights, especially to Dr Lyndon Koens, Julius Kierkegaard, and Dr Pierre Haas. I would also like to thank “The Players" –Justas Dauparas, Dr Debasish Das, and Dr Maciej Lisicki– with whom I had big laughs both at work and outside. During my PhD I also had the opportunity to visit Prof. Mike Shelley at the Flatiron Institute, part of the Simons Foundation (USA). My sincere thanks go to him, the foundation, and his group. It was a tremendous experience in which I exchanged ideas and received really valuable feedback and advice on my project.

I am also particularly grateful to Giovanni Crostarosa who believed in me and helped me secure part of the funding for my first year through the Alumni RUI Association. I would further like to thank the Department of Applied Mathematics and Theoretical Physic at Cambridge and EPSRC for funding my PhD. Special thanks go to Peterhouse for being an amazing place to live in and its generous financial support. Many are the memories of my life in College with my fellow Petreans that I will bring with me forever.

Thanks also go to all my friends in the Cambridge community, especially the Men’s Blues of the Cambridge University Volleyball Club. During three years of trainings and matches I had the chance to truly enjoy myself. I also would like to thank my old friends from Politecnico di Milano, Torrescalla, Imperial College London, and Netherhall House, who, despite the distance, showed me their presence. Among them I would like to thank Paolo Figallo, Alessandro Damonte, Alessandro Bronzin, Matteo Cunial, and Michelangelo Corelli for always being there whenever I needed them. Morever, I would like to thank Anna, Katherine, and Giulia for accompanying me at different stages of my PhD. Their presence and constant support have been fundamental.

Last, but not least, my greatest thanks go to my parents, my sister, my grandparents, and all my relatives. They have always been there with their love over the years. In particular, I would like to deeply thank my parents for always believing in me and looking after me during the health problems I had. Their renounces and efforts have allowed me to become the first person to go to university and study at the highest levels. This thesis is mainly for them.

All these people showed an incredible support to me. Without them this thesis would not be possible.

Chapter 1 contains, in part, introductory material printed in De Canio, G., Lauga, E. & Goldstein, R. E. (2017) Journal of the Royal Society Interface 14, 20170491. The dissertation author was the primary investigator and author of this manuscript.

Chapter 2 is a reprint of De Canio, G., Lauga, E. & Goldstein, R. E. (2017) Journal of the Royal Society Interface 14, 20170491. The dissertation author was the primary investigator and author of this manuscript.

Chapter 3 contains, in part, findings printed in De Canio, G., Lauga, E. & Goldstein, R. E. (2017) Journal of the Royal Society Interface 14, 20170491. The dissertation author was the primary investigator and author of this manuscript.

Part of Chapter 3 and Chapters 4 and 5 are in preparation for being submitted as *Collective dynamics of elastic filaments actuated by follower forces* De Canio, G., Goldstein, R. E. & Lauga, E. (2018). The dissertation author is the primary investigator and author of this manuscript.

Abstract

In cellular phenomena, such as cytoplasmic streaming, molecular motors translocate along microtubules carrying cargoes which entrain fluid. The piconewton forces that motors produce can be sufficient to bend or buckle the filaments. When large numbers of such forced filaments interact through the surrounding fluid, as seen in particular stages of oocyte development in *Drosophila melanogaster*, complex dynamics arise, but the mechanism underlying them has remained unclear.

Motivated by these observations, through a combination of theoretical analysis and numerical simulations, we study a simplified microtubules-molecular motor system. Microtubules are modelled as elastic inextensible two-dimensional filaments, and the molecular motor-cargo ensemble as a point force. The analysed dynamics result from the interplay between the forcing, elasticity, and hydrodynamic stresses associated with the motion in a viscous fluid.

First, we study a single filament subject to a localised force acting tangentially at its tip. We show that when the external forcing exceeds a finite threshold, the system undergoes a Hopf bifurcation, which results in flapping motion, reminiscent of spermatozoa beating. We elucidate the nature of such instability using a lower-dimensional 'two-link' model and linear stability analysis. Then, we generalize the model to describe the real biological system more accurately. In particular, we include the fluid flow created by the molecular motor-cargo ensemble while it is walking along the microtubules, we allow the molecular motor to be located anywhere along the filament, and extend the framework to the case of many motors.

Inspired by experiments, in which many filaments interact with one another, we apply these extensions to the multi-filament case, with the aim of studying the collective dynamics of flapping filaments. We consider two distinct scenarios: an array of filaments on a planar wall, and a multitude of filaments inside a sphere. By exploiting asymptotic approximations and parallel computing, we show that an array of filaments can synchronise their motion or reach a final steady bent configuration. Moreover, we shed light on the role of confinement, which proves to be crucial in spontaneously breaking the symmetry in the filament configuration, as experimentally observed.

Our results form the basis for the deeper physical understanding of the role of fluid-structure interactions during the oocyte development in *Drosophila*. By employing a range of models of increasing complexity, we have been able to capture the wave-like filament motion observed in experiments, paving the way for future research involving more physiological details.

Table of contents

List of figures

List of tables

Chapter 1

Introduction

The biological world includes a broad range of phenomena in which transport in a fluid plays a central role. Among these is the fundamental issue of cell polarity arising during development, studied historically using the model organism *Drosophila melanogaster*. The polarity of its oocyte is known to be induced by the translocation of mRNAs by motor proteins along a dense microtubule cytoskeleton. This translocation process also induces cytoplasmic streaming. Recent experimental observations have revealed the remarkable fluid-structure interactions that occur as the streaming flows back-react on the microtubules [1].

Such dynamics have been experimentally studied by several authors in the biology community [see 2, and references therein]. However, a precise formulation and analysis of these problems from a biophysical standpoint has been lacking. This thesis aims at presenting such an analysis by studying a simplified model, which, despite its reductionist nature, is still able to capture the essence of the experimental observations.

In the remainder of chapter 1, we will discuss some examples of complex dynamics arising from the action of motor proteins (Sec. 1.1). We then focus on the specific case of cytoplasmic streaming in *Drosophila* (Sec. 1.2). We describe how motor proteins and microtubules have been modelled from both a fluid and solid mechanics perspective in Sec. 1.3, and outline the structure of this thesis in Sec. 1.4.

1.1 Filament motion induced by motor proteins

Molecular motors are molecules that are responsible for transporting biological materials inside cells. Among them are motor proteins that bind to polarized cytoskeletal filaments and translocate steadily along them. They do so by repeated cycles of ATP hydrolysis, thus converting chemical energy into mechanical work, while carrying cargoes (Fig. 1.1) [3, 4].

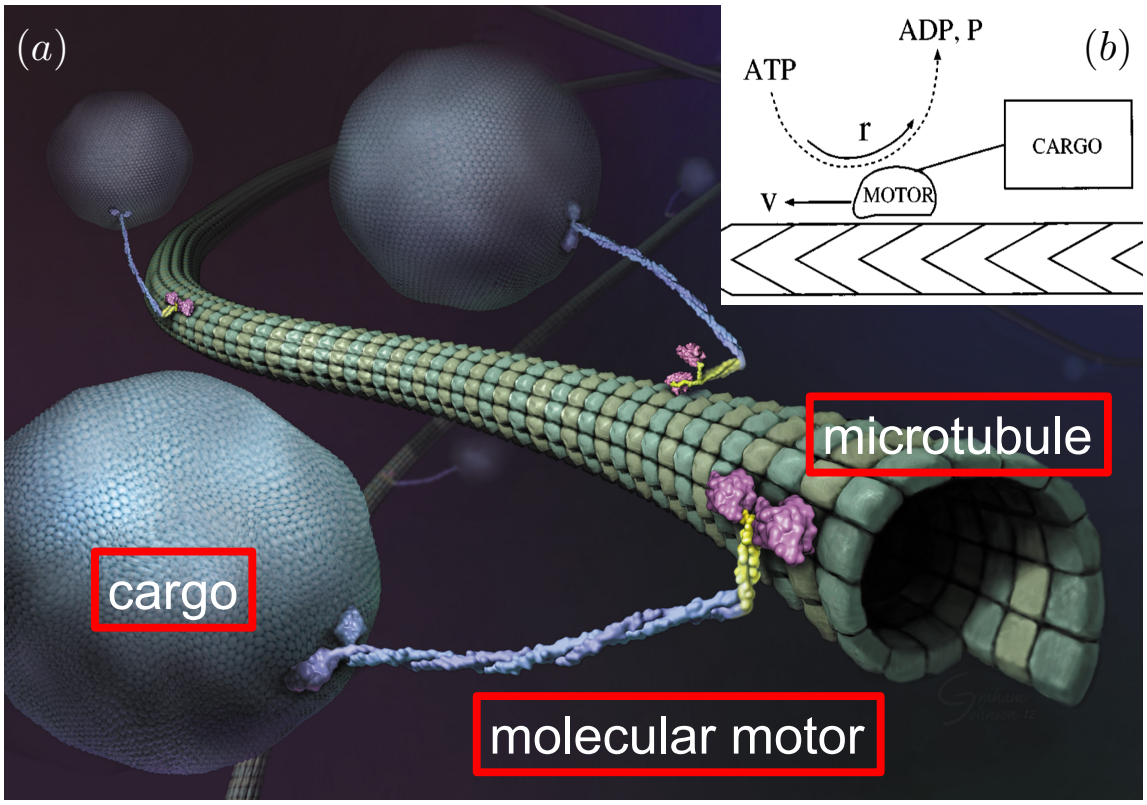

Fig. 1.1 (a) Diagram of translocating motor proteins along MTs while carrying cargoes. (Adapted from [5].) (b) Schematic of a motor protein moving with velocity v while transporting a cargo. The motor is able to walk by converting chemical energy into mechanical work by hydrolysing ATP to ADP and phosphate (P). (Adapated from [6].)

Motor proteins are ubiquitous in eukaryotic cells and differ in the type of cargo carried, the direction of motion and the type of filament they bind to (either actin or microtubules). Some motor proteins carry organelles or vesicles and transport them to specific locations in the cell [4]; while others cause sliding of adjacent filaments which results in phenomena such as ciliary beating and muscle contraction [4]. Myosins use actin filaments as cytoskeletal tracks, while dyneins and kinesins move along microtubules (MTs) [7]. Motor proteins move at speeds of the order of fractions of microns/sec and are able to exert forces on the surrounding fluid on the piconewton scale, $F_{\text{motor}} \approx 1$ pN [7]. These forces are sufficient to bend or buckle a MT, which typically has length $L \approx 10 - 20\,\mu$m and bending modulus, $A \approx 10^{-23}$ N m^2 [8], thus giving rise to complex dynamics. This can be easily shown through a simple scaling argument: the ratio of the external force to the elastic force, namely $F_{\text{motor}}/(A/L^2)$, is in fact greater than one.

Among the many examples of filament deformation induced by molecular motors [9–14], we recall that in the context of "motility assays" it has been observed that single filaments

forced by carpets of motors on a surface can undergo a variety of buckling instabilities, particularly when one end is pinned by a 'defect' in the monolayer of motors [15, 8]. Similar instabilities were also observed in microtubules gliding in axoplasm, in which the MTs would undergo 'serpentine' movements when encountering an obstacle [16].

Another example of complex dynamics induced by molecular proteins is the phenomenon of cytoplasmic streaming. Discovered first in aquatic plants in 1774 by Bonaventura Corti [17], it is now known to occur in a broad spectrum of aquatic and terrestrial organisms [18]. In each case of motor protein-filament pairs –typically myosin-actin in plants and kinesin-microtubules in animals– cargo carried along by the motors entrains cytoplasmic fluid, creating flows whose degree of organization reflects the architecture of the filament network. While in mature plants the filaments tend to be anchored along the interior cell wall, in young developing plant cells, and also in mature cells whose cytoskeleton has been transiently chemically disrupted, there is strong evidence of self-organization processes [19] which likely involves filament buckling and alignment by the very flows created by the moving motors [20]. In the case of animals, the paradigm is oogenesis in the fruit fly *Drosophila* [21], in which a dense network of microtubules emanates from the entire periphery of the oocyte, so that one end of each filament is anchored at the oocyte boundary while the distant end is free within the cellular interior. Direct visualizations [1] of the streaming flows (by means of endogenous tracer particles) and the microtubules (fluorescently labelled) show that the flows are disordered on the scale of the oocyte and are time-dependent on the scales ranging from seconds to many minutes. While the long-time variation reflects changes in the composition of the cytoskeletal fluid, the short-term variations arise from the motion of the filaments in response to the streaming flows. We note that streaming is also present in neuronal contexts, but there the filaments are often strongly cross-linked by microtubule-associated proteins [22].

1.2 Cytoplasmic streaming in *Drosophila*

Drosophila is one of the most widely used organisms in genetics and experimental biology owing to its small dimensions, short generation time, and facility to be grown in the laboratory [23]. Several studies have been conducted using it as a model to study the process of formation of a mature egg cell, called oogenesis. In *Drosophila*, this lasts approximately 80 hours and has been divided in 14 stages depending on the morphology of the egg chamber [24, 25]. The egg chamber is surrounded by follicle cells and composed of an oocyte and 15 nurse cells. Nurse cells are connected to the oocyte via bridge-like structures called ring canals (Fig. 1.2a) [2].

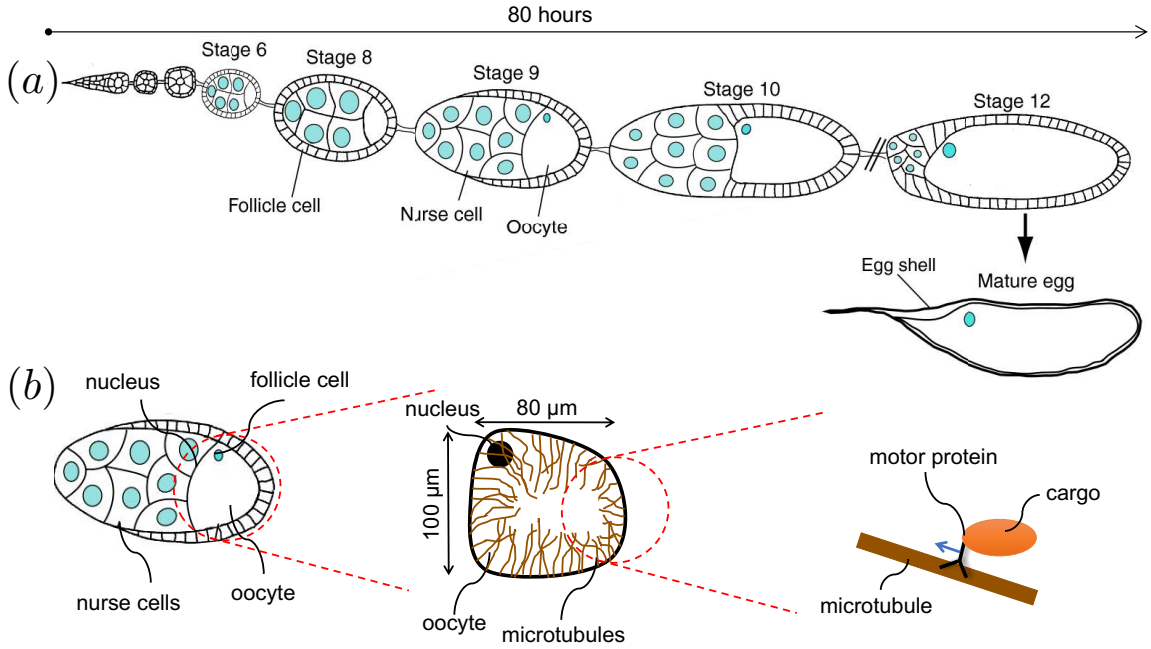

Fig. 1.2 (a) Oogenesis of *Drosophila melanogaster*. The entire process lasts about 80 hours and has been divided in 14 stages depending on the morphology of the egg chamber [24, 25]. The egg chamber is surrounded by follicle cells and composed of an oocyte and 15 nurse cells. (Adapted from [2].) (b) Cartoon of the MT meshwork inside the oocyte. Along each MT, motor proteins translocate while carrying cargoes such as mRNAs, vesicles and nutrients.

Being a eukaryote, *Drosophila* possesses the nucleus, which houses the DNA, and the cytoplasm, which consists of a suspension of organelles in a liquid-like medium called cytosol. Since cells need to interact mechanically with the environment as well as organise themselves, their internal components must be able to rearrange during their lives. In eukaryotes, this is mediated by a system of filaments contained inside the cell: the cytoskeleton [26].

1.2.1 Origin of cell polarity

Essential during oogenesis is the transport of proteins, organelles and mRNAs from the nurse cells to the oocyte. This process takes places by exploiting molecular motors which translocate along the cytoskeleton carrying cargoes (Fig. 1.2b) [2]. After reaching the oocyte, these cargoes have to be transported to specific regions to accomplish their functions and therefore allow the oocyte to continue its development. *Myosins*, *dyneins* and *kinesins* are the three motor proteins responsible for actively transporting cargoes, converting the chemical energy into mechanical work to bind to the cytoskeleton and move along the filaments [7]. Different models for describing the underlying walking mechanism, which differs between the motors, have been proposed, but an explanation about their high efficiency in

transforming energy into work remains unclear [5]. The active transport mediated by the motors entrains the surrounding fluid, giving rise to an advective movement of cytoplasm, known as *cytoplasmic streaming* [27–29].

The cytoskeleton, which evolves during oogenesis, is constituted by three main types of filaments: actin filaments, necessary for the whole-cell locomotion, intermediate filaments, for providing mechanical strength, and microtubules (MTs), for organising organelles and directing intracellular transport [26]. Actin filaments are composed of a subunit called G-actin and their diameter is typically 9 nm. MTs are made of 13 parallel protofilaments, each formed from alternating α- and β-tubulins, which create a hollow cylinder whose outer diameter is 25 nm [26]. The succession of α- and β-tubulins sets an intrinsic polarity to the MT, thus defining a minus- and a plus-end. MTs are extremely dynamic: their ends alternatively experience *catastrophes*, the change from growth to shrinkage, and *rescues*, from shrinkage to growth. These processes stochastically modify both their shape and length, by a succession of binding and hydrolysis events [26, 30, 31]. For this, MTs are said to undergo 'dynamic instability'. Rescues and catastrophes do not occur sequentially one after the other; after slowly growing, MTs abruptly shrink. If we were to plot how the MTs length varies in time, we would observe a sawtooth-like function.

The typical growth and shrinkage rates of mammalian bovine brain MTs *in vitro* are about 30 nm/s and 300 nm/s, respectively [32]. *In vivo* experiments performed on the *Xenopus laevis* revealed a growth rate of about 500 nm/s [33], suggesting that the dynamic instability occurs differently among the species and that *in vivo* and *in vitro* studies can lead to quantitatively different results. In *Drosophila* oocytes, no studies have been conducted on the dynamic instability of MTs.

mRNAs are actively transported by *dynein* and *kinesin* motors, which walk along MTs towards the minus- end and the plus-end, respectively. The localisation of mRNAs to specific regions in the *Drosophila* oocyte establishes the anteroposterior (AP) and dorsoventral (DV) body axes of the embryo [34]. The embryo therefore becomes polarised already at stage 9, but a late-phase of mRNA localisation occurs at stage 11, as described below. Cell polarity is fundamental for normal cell function as well as the development of the egg chamber [35–40]. Recent studies have shown that the loss of polarity is also a key feature in the formation of tumours [41].

1.2.2 Streaming and MTs

Being interested in the motors-induced dynamics, this study focuses on the evolution of the oocyte between stage 9 and 11 only. At stage 9, the oocyte is roughly hemispherical, being approximately 100 μm in length along the DV axis and 80 μm along the AP axis.

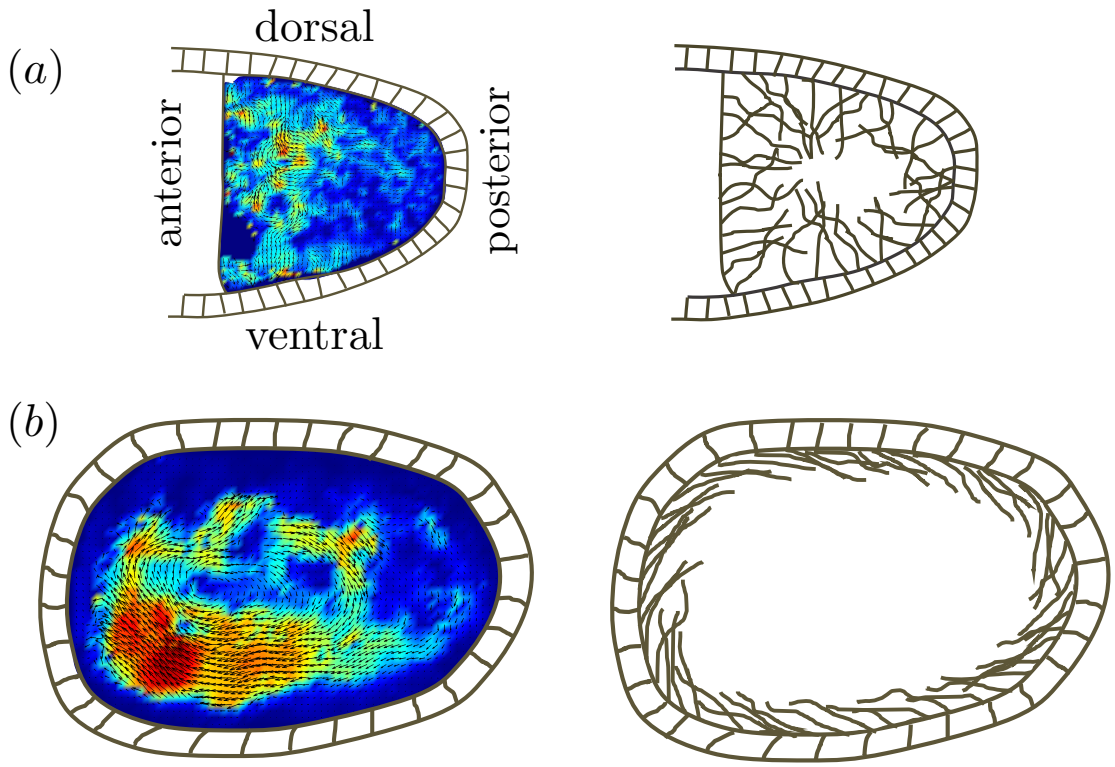

Fig. 1.3 Fluid flows and MT meshwork at stage 9 and 11. The velocity fields, superimposed to the cartoons of the oocyte, were obtained by performing Particle Image Velocimetry (PIV) on a set of images taken by Dr. Maik Drescher using PIVLab [46]. (a) At stage 9, MTs are highly entangled and undergo waving motion, while the fluid flow is mainly localised to the anterior side of the oocyte. (b) At stage 11, MTs form long bundles close to the boundary of the oocyte, and the fluid flow exhibits a circulatory pattern that covers the entire oocyte.

Both the actin and MT meshwork are present. Actin filaments are randomly oriented, but homogeneously distributed inside the oocyte. The dense, short-filaments-made actin mesh results in a high dynamic viscosity, about 1.38 Pa s [1]. MTs are nucleated from the entire boundary of the oocyte and are anchored at their minus-ends. They point to the centre of the cell and exhibit a steep gradient in their local density moving from the anterior towards the posterior pole (Fig. 1.3a) [42–44]. They measure 20-40 μm and assume entangled configuration while undergoing wave-like motions [1]. The cytoplasmic streaming appears to be slow (5-10 nm/s), unsteady, and spatially inhomogeneous [45], as it is indeed primarily localised in the anterior half of the oocyte (Fig. 1.3a) [1]. *Dyneins* and *kinesins* walk on the MT meshwork to conclude mRNAs localisation initiated at stage 8 [42].

During stage 10, the follicle cells migrate from the anterior to the posterior pole, the actin meshwork dissolves, and the nurse cells contract and pump their contents to the oocyte through the ring canals, making the oocyte grow in size. At stage 11, the MTs form long

bundles close to the boundary of the oocyte while the cytoplasmic flow becomes vigorous and fast (120-130 nm/s), covers the entire oocyte, and shows a circulatory pattern (Fig. 1.3b)[45]. This fast streaming enhances the localisation of mRNA, thus constituting the late-phase of mRNA localisation [47, 48].

1.2.3 Open questions

Flows at stages 9 and 11 are not only topologically, but also quantitatively different. Moreover, also the underlying MT meshwork exhibits a significant difference, specifically in its orientation. Despite the importance of cell polarity, that has led to several studies focussed on mRNAs localisation and stage 9 of *Drosophila* oogenesis, research on the transition between slow to fast streaming is scarce and solely experimental [2].

Serbus and colleagues exploited mutants of *Drosophila* to show that *kinesin* is capable of driving a coherent circulatory fast streaming before stage 11, but *dynein* and the actin meshwork can repress such premature onset [45]. They speculated that the actin cytoskeleton is responsible for the shift from slow to fast streaming by inhibiting *dynein*, which competes in a tug-of-war manner with *kinesin*. However, a clear picture of the underlying mechanism is still missing [45]. In addition, the question of why MTs undergo waving motion at stage 9 and transition to statically laying down on the surface of the oocyte remains unanswered. Theoretical instantiations of this behaviour can be difficult however due to the complex mathematics involved.

1.3 The mathematical modelling of filaments and motors

As previously discussed, *kinesin* and *dynein* motors are responsible for transporting molecular cargoes inside the oocyte: *kinesins* move towards the plus-end of the MT, while *dyneins* towards the minus-end. The effect of walking along MTs transporting mRNAs, nutrients, and other organelles results in setting up a fluid flow. This active transport together with the advective transport of cargoes inside the oocyte give rise to cytoplasmic streaming, whose typical speed at stage 9 is $U \approx 10$ nm/s. The size of the oocyte measures $L_\mathrm{o} \approx 100\,\mu$m and the cytoplasm is primarily constituted of water ($\sim$80%). Experimentally, it was shown that the dynamic viscosity at stage 9 is three orders of magnitude higher than water. However, as a conservative estimation, we can assume the kinematic viscosity of the fluid being approximately equal to that of water, $\nu \approx 10^{-6}$ m^2/s.

In a fluid, the ratio of inertial forces to viscous forces is given by the Reynolds number, $\mathrm{Re} = UL_\mathrm{o}/\nu$, where U is the velocity scale, L_o the length scale of the system, and ν the

kinematic viscosity of the fluid. The Reynolds number for this biological fluid system is $\mathrm{Re} \approx 10^{-6}$, thus implying that inertia is negligible and viscous forces dominate. In this regime, the dynamics of the fluid is governed by the incompressible Stokes equations, which read

$$\boldsymbol{\nabla} p = \mu \nabla^2 \boldsymbol{u} + \rho \tilde{\boldsymbol{f}}\,, \tag{1.1}$$

$$\boldsymbol{\nabla} \cdot \boldsymbol{u} = 0\,, \tag{1.2}$$

where p is the dynamic pressure, $\boldsymbol{u}$ the velocity of the fluid, μ and ρ its dynamic viscosity and density, and $\tilde{\boldsymbol{f}}$ the external body force per unit mass. Depending on the boundary conditions and on the external force, the velocity and pressure fields can be computed either analytically or numerically. Notably, these equations are time independent and linear.

Because of the several applications in a variety of instances, of particular interest is the case of determining the fluid flow generated by a point force, i.e. a force applied at a certain point in the fluid. Examples include the flow due to the motion of small particles in a suspension [49] and boundary-integral representations to derive boundary-integral equations [50, 51]. The velocity field $\boldsymbol{u}(\boldsymbol{x})$ created by a point force at $\boldsymbol{x}_0$ in an unbounded domain corresponds to the one resulting from the slow motion of a small particle in a fluid otherwise at rest. Mathematically this corresponds to solving the equations

$$\boldsymbol{\nabla} p = \mu \nabla^2 \boldsymbol{u} + \boldsymbol{F}\,\delta(\boldsymbol{x} - \boldsymbol{x}_0)\,, \tag{1.3}$$

$$\boldsymbol{\nabla} \cdot \boldsymbol{u} = 0\,, \tag{1.4}$$

where $\boldsymbol{F}$ represents the direction and magnitude of the point force and δ is the three-dimensional delta function. The velocity field is then given by

$$\boldsymbol{u}(\boldsymbol{x}) = \frac{1}{8\pi\mu}\boldsymbol{G}(\boldsymbol{x};\boldsymbol{x}_0)\cdot\boldsymbol{F} = \frac{1}{8\pi\mu}\frac{\boldsymbol{I} + \hat{\boldsymbol{R}}\hat{\boldsymbol{R}}}{|\boldsymbol{R}|}\cdot\boldsymbol{F}\,, \tag{1.5}$$

where $\boldsymbol{G}(\boldsymbol{x};\boldsymbol{x}_0)$ is the Green's function, $\boldsymbol{I}$ the identity tensor, $\boldsymbol{R} = \boldsymbol{x} - \boldsymbol{x}_0$ is the vector pointing from the location of the point force to that of the desired point in the domain, and $\hat{\boldsymbol{R}}$ its unit vector. This fundamental singularity is called the 'stokeslet'. Other fundamental singularities such as stresslets and rotlets can be obtained by taking derivatives of the stokeslet [52].

1.3.1 Hydrodynamics of slender filaments in creeping flows

MTs, similarly to flagella, are slender filaments, as their width b is much smaller than their length L, $L \gg b$. In Stokes flows, also called creeping flows, their motion can be

mathematically described by two different theories: resistive-force theory (RFT) [53] and slender-body theory [54–57].

Resistive-force theory (RFT) was initially proposed by Gray and Hancock to describe the swimming of sea urchin spermatozoa [53]. This model assumes that a slender filament, defined by $\boldsymbol{r}$, can be locally approximated by a rod, thus providing a local relation between its velocity $\boldsymbol{r}_t \equiv \frac{\partial \boldsymbol{r}}{\partial t}$ and the hydrodynamic force per unit length exerted by the surrounding fluid $\boldsymbol{f}_{\mathrm{h}}$. When a background flow $\boldsymbol{u}$ is present, this reads

$$\boldsymbol{f}_{\mathrm{h}} = -\left(\zeta_{\parallel}\hat{\boldsymbol{t}}\hat{\boldsymbol{t}} + \zeta_{\perp}\hat{\boldsymbol{n}}\hat{\boldsymbol{n}}\right)\cdot(\boldsymbol{r}_t - \boldsymbol{u})\,, \tag{1.6}$$

where $\hat{\boldsymbol{t}}$ and $\hat{\boldsymbol{n}}$ are the local tangent and normal unit vectors to the centreline, and $\zeta_{\perp}$, $\zeta_{\parallel}$ are the drag coefficients in the perpendicular and parallel direction [58] and are given by

$$\zeta_{\parallel} = \frac{2\pi\mu}{\ln(L/b) - \frac{1}{2}}\,, \tag{1.7}$$

$$\zeta_{\perp} = \frac{4\pi\mu}{\ln(L/b) + \frac{1}{2}}\,. \tag{1.8}$$

The drag coefficients express the anisotropy of the viscous forces experienced by the filament, noticeable for instance when dragging a slender body in a high-viscosity medium. Such anisotropy plays a paramount role in the swimming problem at low Reynolds number as it is required for drag-based thrust [see 59, and references therein]. Depending on the shape of the body more accurate expressions for the two coefficients may be derived [60, 57, 55]. By Newton's third law, the force acting *on* the filament *by* the fluid is the drag force, which trivially reads $\boldsymbol{f}_{\mathrm{d}} = -\boldsymbol{f}_{\mathrm{h}}$. RFT can capture the essential physics of a system. However, it is valid for filaments that are 'exponentially thin' as it is accurate to order $(1/\ln(L/2b))^2$.

When accuracy is required, slender-body theory (SBT) should be exploited. SBT, initially developed by Hancock [61], is based on the idea of taking advantage of the slenderness of the filament and placing a line of fundamental singularities along its centreline. The kernel of the resulting line integral is expanded in two domains determined by which length scale dominates, either the thickness of the body or the centreline length. To then compute the velocity field at the surface of the body, the two domains are matched asymptotically [60]. Many authors proposed different formulations [54, 55, 57]. Among them, Johnson derived an improved version of SBT in order to account for the ends of the body [56].

1.3.2 Solid mechanics of slender filaments

In this section, we derive the solid mechanics equations for a MT. As previously discussed, MTs can easily bend and buckle, so elasticity must be included in the mathematical formulation. Moreover, they shrink and grow, thus modifying their length. For simplicity, we neglect these changes and assume they have constant fixed length. The governing equations for a slender elastic inextensible filament can be derived using either force and moment balance on an infinitesimal element bounded by two cross-sections or from energy functional [62]. In the following, we consider the latter approach. The elastic energy $\mathscr{E}_{\text{el}}$ of a slender bent filament of length L and curvature $\kappa(s)$ with constant circular cross-section, parametrised by the arclength s, is

$$\mathscr{E}_{\text{el}} = \frac{A}{2}\int_0^L \kappa(s)^2 \,\mathrm{d}s\,, \tag{1.9}$$

where A is the bending modulus, which is defined as $A = EI$, E being the Young's modulus and I the moment of inertia. Here, no intrinsic curvature was assumed [62, 63]. Interestingly, the bending modulus can also be expressed in terms of the persistence length L_{p} as $A = k_{\text{B}}TL_{\text{p}}$, with k_{B} the Boltzmann constant and T the absolute temperature. Inextensibility can be imposed through the Lagrangian multiplier $\Lambda(s)$ [64]. The energy functional associated with the local arclength conservation $\mathscr{E}_{\text{ten}}$ reads

$$\mathscr{E}_{\text{ten}} = -\frac{1}{2}\int_0^L \Lambda(s)\,\mathrm{d}s\,, \tag{1.10}$$

hence the total energy functional for an elastic inextensible filament will be $\mathscr{E} = \mathscr{E}_{\text{el}} + \mathscr{E}_{\text{ten}}$.

From the energy functional, the Lagrange equation, in its general formulation, can be used to obtain the governing equations. Defining $\mathscr{L}$ the Lagrangian and $\boldsymbol{Q}(s)$ the forces acting on the filament that cannot be expressed through a potential, i.e. nonconservative force, the Lagrange equation of motion reads

$$\frac{\mathrm{d}}{\mathrm{d}t}\frac{\partial \mathscr{L}}{\partial \boldsymbol{r}_t(s)} - \frac{\partial \mathscr{L}}{\partial \boldsymbol{r}(s)} = \boldsymbol{Q}(s)\,. \tag{1.11}$$

At low Reynolds number inertia is negligible, hence the Lagrangian includes only the terms arising from the potential energy functional $\mathscr{E}[\boldsymbol{r}]$, namely $\mathscr{L} = -\mathscr{E}$. The equation of motion can therefore be rewritten in terms of functional derivatives as

$$-\frac{\delta \mathscr{E}}{\delta \boldsymbol{r}(s)} = \boldsymbol{Q}(s)\,. \tag{1.12}$$

Repeated integration by parts leads to

$$\delta\mathscr{E} = \delta\mathscr{E}_{\text{el}} + \delta\mathscr{E}_{\text{ten}} \tag{1.13}$$

$$= A\int_0^L \boldsymbol{r}_{ss}\cdot\delta\boldsymbol{r}_{ss}\,\mathrm{d}s - \int_0^L \boldsymbol{r}_s\cdot\delta\boldsymbol{r}_s\,\Lambda\,\mathrm{d}s \tag{1.14}$$

$$= A\boldsymbol{r}_{ss}\cdot\delta\boldsymbol{r}_s\Big|_0^L - A\boldsymbol{r}_{sss}\cdot\delta\boldsymbol{r}\Big|_0^L + A\int_0^L \boldsymbol{r}_{ssss}\cdot\delta\boldsymbol{r}\,\mathrm{d}s$$
$$-\Lambda\boldsymbol{r}_s\cdot\delta\boldsymbol{r}\Big|_0^L + \int_0^L (\boldsymbol{r}_{ss}\Lambda + \boldsymbol{r}_s\Lambda_s)\cdot\delta\boldsymbol{r}\,\mathrm{d}s\,, \tag{1.15}$$

where subscripts indicate differentiation. Depending on the boundary conditions, the "surface terms" may vanish. If one end of a filament is clamped, we must have $\boldsymbol{r}=\boldsymbol{0}$ there, and also $\boldsymbol{r}_s=\boldsymbol{0}$, since its direction cannot change. If the end is hinged, the filament cannot move, but its direction can change; this corresponds to the conditions $\boldsymbol{r}=\boldsymbol{0}$ and $\boldsymbol{r}_{ss}=\boldsymbol{0}$. Lastly, if the filament has a free end, both the force and the moment there must be zero, thus giving the conditions $A\boldsymbol{r}_{ss}=A\boldsymbol{r}_{sss}=\boldsymbol{0}$ and $\Lambda=0$. Notice that if a concentrated force or moment were applied at the free end, the force and moment would equal these external load and torque instead. If we consider the case of a filament clamped at $s=0$ and free at $s=L$, then we have that in Eq. (1.15) the terms $\delta\boldsymbol{r}|_{s=0}=\delta\boldsymbol{r}_s|_{s=0}=\boldsymbol{0}$ as well as $\boldsymbol{r}_{ss}|_{s=L}=\boldsymbol{r}_{sss}|_{s=L}=\boldsymbol{0}$ and $\Lambda|_{s=L}=0$. In other words, all surface terms will vanish. After computing the functional derivative, Eq. (1.12) becomes

$$-A\boldsymbol{r}_{ssss} - (\Lambda\boldsymbol{r}_s)_s = \boldsymbol{q}\,, \tag{1.16}$$

where the RHS is the nonconservative force per unit length and LHS represents the well-known result coming from Euler-Bernoulli beam theory [65].

1.3.3 Modelling molecular motors

Molecular motors are complicated micromachines that play a central role in several biological processes [4]. For this reason many authors in the biophysics community have developed models to describe how they function [6]. Motors are characterised by unidirectional motion. Crucially, while translocating along the MTs they exert a tangential force on the filaments and push the surrounding fluid, thus inducing a flow.

Because of their small size, Brownian motion is perpetually present and their directed movement can be described by appropriate Langevin equations [66]. Motors have one end attached to the cargo and the other to the MT, to which they bind and unbind at different rates [67, 68]. These events have been typically modelled as Poisson processes in the literature

(e.g. [69]). For kinesins, depending on the ATP concentration, the steps they walk along the MT vary with the ATP concentration and the load applied, thus making the description of the linkage between the cargo and the MT via a spring, acting through the motor, suitable [70]. A similar approach was proposed by Huxley in his seminal work on muscles structure and their contraction [71]. In addition, motors move at velocities that almost linearly decrease with the external force applied, until stopping when reaching a certain stall force (in the piconewton range) [72]. To study the collective properties of motors, different approaches have been proposed [73]. A model that has become popular for its simplicity while still providing physical insights, consists in treating the motors rigidly coupled to the backbone [74].

1.3.4 Modelling assumptions

Inspired by a recent study which has shown that in *Drosophila* MT cytoskeleton is the essential driver of mRNA localisation [75], and by the experimental findings which revealed the remarkable interplay between cytoplasmic streaming and MT meshwork both in the wild type and in mutants [1, 76], we have developed and implemented a theoretical framework to address the questions mentioned above based on a mechanism of fluid-structure interactions at low Reynolds number. In fact, the cytoplasmic streaming rearranges both the microtubular meshwork and the location of motor proteins, since these are anchored to the MTs. Consequently, the fluid flow created by the motors at the new location will be different, affecting again the configuration of the MTs. The approach is therefore based on studying the dynamics and the feedback of the MTs on the fluid flow and vice versa.

The model presented in this thesis aims at capturing the physics underlying both the waving motion of the MTs and the transition from entangled to disentangled MT meshwork with the corresponding circulatory fluid flow, by exploiting a reductionist approach. To this aim, we should consider only the main features possessed by each constituent in the real *Drosophila* oocyte that may contribute to driving the physical phenomena observed.

- The *oocyte*'s geometry changes considerably during the transition consequently to the nurse cell dumping. We assume the oocyte to have spherical shape, constant and fixed volume, and neglect the flow coming from the boundary, i.e. the no-slip condition applies. At stage 11, the cytoplasmic flow describes a circulatory, coherent motion that covers the whole oocyte and the MTs lay down on its surface with every section of the oocyte parallel of its mid-plane exhibiting a similar microtubular meshwork and fluid flow topology. To simplify the mathematical model and considerably reduce the computational cost, we constrain the MTs to move on the mid-plane of the sphere since

3D effects would just enhance the perturbations on the plane, quantitatively affecting the results but not qualitatively.

- *Motor proteins* are ubiquitous in the oocyte. However, it is known that among them kinesins, which move from the periphery towards the centre, are the ones able to trigger the transition from stage 9 to 11 [45]. Potential tug-of-war mechanisms between kinesins and dyneins in pulling cargoes [77, 78], as well as the possible hydrodynamic interactions arising from the motion of motors that entrain fluid thus helping other motors move [79] will be neglected. Molecular motors will be rigidly connected to both cargoes on one end (the motor-cargo ensemble will be treated as a single entity hereafter), and MTs on the other end. Lastly, the motion of the motors regulated by ATP hydrolysis and the stochastic events of binding and unbinding to the MTs will be completely neglected, thus the bound state will be assumed throughout.

- *MTs* are the tracks for kinesins. Their growth-and-shrink dynamics as well as the friction between them will not be included.

- *Actin filaments* are homogeneously distributed in the whole oocyte. In this work their potential visco-elastic rheology is neglected, and the fluid is assumed to be Newtonian at the relevant shear rates [1].

Summary of the assumptions

To summarise, the assumptions our model is based on are the following:

i. The oocyte will be treated as a spherical container with no-slip boundary conditions. MTs will only be placed in its mid-plane so that the contribution of the fluid flow in the direction perpendicular to the plane from the top and the bottom halves will cancel out because of incompressibility.

ii. The motor-cargo ensemble is stationary and always anchored to the MT. Its effect of compressing the filament while entraining fluid is translated into approximating the ensemble with a point force.

iii. MTs are elastic filaments with fixed length. In order to reduce the complexity of the analysis and the computational cost, we constrain the MTs to move on a plane and a 2D description is sufficient to model their dynamics.

iv. The actin meshwork does not enter the model directly as its contribution is included via the viscosity.

1.4 Thesis structure

This thesis is dedicated to addressing the questions related to the complex dynamics induced by molecular motors observed in *Drosophila* oocytes during particular stages of its development. With this aim, we study models with increasing complexity to describe more accurately, yet with simplicity, the real biological system using a combination of theory and simulations.

The thesis can be divided into two parts: in the first part (Chapters 2 and 3), we investigate the individual dynamics of a filament subject to a compressive force; in the second part (Chapters 4 and 5), we explore the resulting dynamics arising when multiple of such filaments hydrodynamically interact. Specifically:

- Chapter 2 treats a single MT under the compression of a single stationary motor-cargo. The resulting dynamics, reminiscent of the MT waving motion observed in the oocyte, is fully characterised and physically explained with the help of a lower dimensional dynamical system.

- Chapter 3 extends the theoretical framework, analytically and computationally, to more realistic cases. These are the instances in which the motor is not located at the tip, it can also entrain fluid flow, and a multitude of motors are present.

- Chapter 4 studies the collective dynamics of an array of filaments. In particular, it shows that synchronous motion is possible.

- Chapter 5 explores how confinement can affect the collective dynamics of the filaments: the mechanical coupling between the fluid motion and the orientation of the microtubules can lead to a transition to coherent motion within the oocyte. This is a remarkable qualitative agreement with the experimental observations.

Finally, Chapter 6 summarises the main results of this thesis and discusses future extensions and explorations that this work has made possible.

Chapter 2

The dynamics of a single filament

In this chapter, we present a precise formulation and analyses of perhaps the simplest possible model appropriate to streaming in order to fully understand the underlying physics. We study a single filament hosting a molecular motor, with one filament end attached to a wall and the other free. Interestingly, a similar setup has also been considered in a recent computational model based on a representation of the filament by a string of passive beads, with an active bead at its tip [80].

Unlike in motility assays [8], a filament responding to the forces produced by motors moving along it corresponds to a motor-induced force that is always tangential to the filament. Known in the mechanics literature as a "follower force" [81], this type of problem is intrinsically different from conventional Euler buckling where opposing thrusting forces are applied along a fixed axis, independent of the filament configuration. As a consequence, the follower-force problem is intrinsically non-variational. Prior studies of this dynamics were primarily in the context of macroscopic systems for which damping is minimal [82, 83]. In such systems, there is a well-known *flutter instability* that can occur for sufficient forcing. This idea has recently been incorporated into a model for eukaryotic flagellar motion [84] as a novel explanation for the origin of the beating waveform, and the work in this chapter is very much in the same spirit.

In Sec. 2.1 we formulate the simplest low Reynolds number follower-force problem, in which the motor exerts a force on the filament but does not itself produce flow, and demonstrate numerically the existence of a Hopf bifurcation when the force exceeds a finite threshold. This threshold is determined through a linear stability analysis in Sec. 2.2. A simplified 'two-link' model of the kind used in inertial problems is solved in Sec. 2.3 to elucidate the nature of the instability, while in Sec. 2.4 a physical interpretation is presented. Finally, Sec. 2.5 presents a discussion of the results achieved.

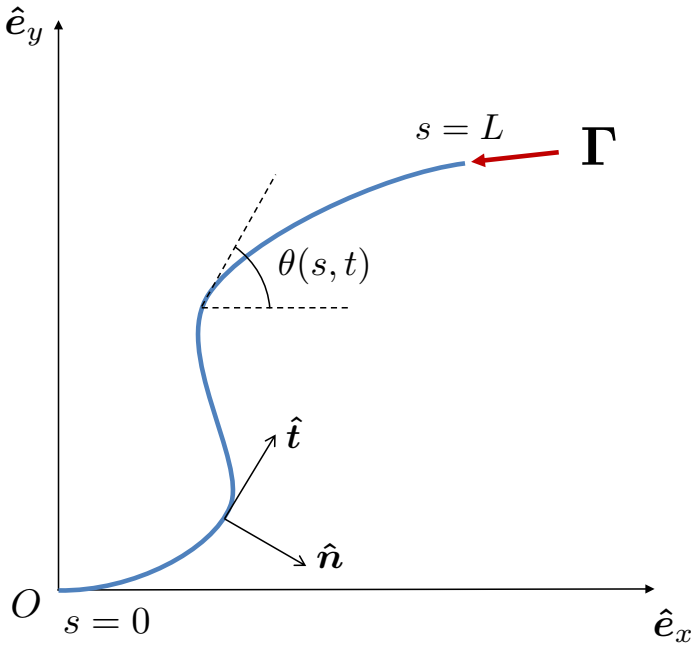

Fig. 2.1 Schematic of a horizontal flexible filament clamped at one end with a follower force $\boldsymbol{\Gamma}$ applied at its tip. The filament position is defined by $\boldsymbol{r}(s,t)$, with $0 \leq s \leq L$ being the arclength, or, equivalently, by the tangent angle $\theta(s,t)$, providing the coordinates of the clamped end. The local tangent and unit vectors are $\hat{\boldsymbol{t}}(s,t)$ and $\hat{\boldsymbol{n}}(s,t)$, respectively.

2.1 Elastohydrodynamics

Here we derive the low Reynolds number equations of motion for a slender elastic filament, clamped at one end and subject to a compressive follower force $\boldsymbol{\Gamma}$, with constant magnitude Γ, moving in a Newtonian fluid of viscosity μ, and confined to the plane $z = 0$. It has length L, diameter b, with $L/b = 50$, constant circular cross-section, and bending modulus A. We parametrise the filament shape $\boldsymbol{r}(s,t)$ by its arclength $0 \leq s \leq L$ (Fig. 2.1). In Table 2.1 we summarise the names, the values and the reference from the literature of the parameters used throughout the text. Note that the filament could have been modelled as either clamped or hinged as both conditions can be found in real biological systems. Though we chose to focus on the case of a clamped filament, the dynamics obtained from the following analysis also occurs for a filament hinged at one end.

2.1.1 Governing equations

The derivation of the governing equations follows the energy functional approach presented in Chapter 1. We assume the standard elastic energy associated with a bent filament, expressed in terms of its curvature $\kappa(s,t)$ as $\mathscr{E}_{\text{el}} = \frac{A}{2}\int_0^L \kappa^2(s,t)\,\mathrm{d}s$, with a vanishing intrinsic curvature

Parameter name	Symbol	Value	Reference
Filament length	L	$10-20\ \mu$m	Ganguly et al., 2012 [1]
Bending modulus of the filament	A	10^{-23} N m^2	Gittes et al., 1993 [85]
Viscosity of the fluid	μ	1 Pa s	Ganguly et al., 2012 [1]
Force of molecular motor	F	$3-5$ pN	Svoboda and Block, 1994 [72]

Table 2.1 Summary of names, values and references from the literature of the parameters used in the thesis.

[63], thus neglecting shearing stresses. Inextensibility is imposed through the Lagrangian multiplier $\Lambda(s,t)$ and the energy functional associated with the local arclength conservation reads $\mathscr{E}_{\text{ten}} = -\frac{1}{2}\int_0^L \Lambda(s,t)\,\mathrm{d}s$ [64]. After computing functional derivatives of the total energy (cf. Sec. 1.3.2), we obtain the classical elastic force per unit length for an inextensible filament, $\boldsymbol{f}_{\text{e}}$, as

$$\boldsymbol{f}_{\text{e}} = -A\boldsymbol{r}_{ssss} - (\Lambda \boldsymbol{r}_s)_s\,, \tag{2.1}$$

where subscripts in italic indicate differentiation. At the clamped end we have the boundary conditions

$$\boldsymbol{r}(0,t) = \boldsymbol{0} \quad \text{and} \quad \boldsymbol{r}_s(0,t) = \hat{\boldsymbol{e}}_x\,, \tag{2.2}$$

as the filament is fixed and horizontal, while at the free end

$$A\boldsymbol{r}_{ss}(L,t) = \boldsymbol{0}\,, \tag{2.3}$$

$$-A\boldsymbol{r}_{sss}(L,t) - \Lambda(L,t)\,\boldsymbol{r}_s(L,t) = -\Gamma\,\boldsymbol{r}_s(L,t)\,, \tag{2.4}$$

which capture the fact the filament is torque-free and that the force at the tip and the external force must balance. Since the follower force acts tangentially, it is nonconservative. It is this feature that gives rise to the complex dynamics in this problem. For a filament hinged at one end, instead of requiring that its direction at $s=0$ must not change (i.e. the tangent to be parallel to the horizontal axis), we would have that the moment of the forces must be zero, namely $\boldsymbol{r}_{ss}(0,t) = \boldsymbol{0}$, thus allowing changes in its direction.

The drag force acting on the filament from the surrounding flow is dissipative, i.e. nonconservative, and therefore belongs to the RHS of Eq. (1.12). In the Stokesian regime, it is classically given in the slender limit by resistive-force theory (RFT) [53, 55]. As discussed in Chapter 1, when no background flow is present, we have

$$\boldsymbol{f}_{\text{h}} = -\left(\zeta_{\parallel}\hat{\boldsymbol{t}}\hat{\boldsymbol{t}} + \zeta_{\perp}\hat{\boldsymbol{n}}\hat{\boldsymbol{n}}\right)\cdot\boldsymbol{r}_t\,, \tag{2.5}$$

where $\hat{\boldsymbol{t}}$ and $\hat{\boldsymbol{n}}$ are the local tangent and normal unit vectors, and $\zeta_\perp$, $\zeta_\parallel$ (with $\zeta_\perp = 4\pi\mu/[\ln(L/b)+1/2]$ [86] and $\zeta_\perp/\zeta_\parallel \to 2$ as $L/b \to \infty$) are the drag coefficients in the perpendicular and parallel direction, respectively [53, 55]. For simplicity, we assume $\eta \equiv \zeta_\perp/\zeta_\parallel = 2$, even if more accurate expression can be used [57], but for the sake of generality we write explicitly η throughout the thesis. While slender-body theory [61, 55, 60], which consists of a more accurate treatment of the drag force to include nonlocal effects, could be used, RFT has been shown to be a valid alternative for single filaments that are not too highly deformed, and its use significantly reduces the complexity of the mathematical formulation [87, 64, 88–92].

Using Lagrange equation, the governing equations are obtained by equating the functional derivative of the total energy to the forces that cannot be expressed through a potential, equivalent to considering the instantaneous balance of forces for the filament when inertia is neglected, given by $\boldsymbol{f}_\mathrm{e} + \boldsymbol{f}_\mathrm{h} = \boldsymbol{0}$. Hence we have

$$-A\boldsymbol{r}_{ssss} - (\Lambda \boldsymbol{r}_s)_s = \left(\zeta_\parallel \hat{\boldsymbol{t}}\hat{\boldsymbol{t}} + \zeta_\perp \hat{\boldsymbol{n}}\hat{\boldsymbol{n}}\right) \cdot \boldsymbol{r}_t \,. \tag{2.6}$$

Exploiting the two-dimensional Frenet-Serret equations, $\hat{\boldsymbol{t}}_s = -\kappa\hat{\boldsymbol{n}}$ and $\hat{\boldsymbol{n}}_s = \kappa\hat{\boldsymbol{t}}$, this can be rewritten as

$$\boldsymbol{r}_t = \frac{1}{\zeta_\perp}\left[A\left(\kappa_{ss} - \kappa^3\right) + \kappa\Lambda\right]\hat{\boldsymbol{n}} + \frac{1}{\zeta_\parallel}\left(3A\kappa\kappa_s - \Lambda_s\right)\hat{\boldsymbol{t}} \,. \tag{2.7}$$

[Note that the form of the elastic component of the normal force often seen in the literature [64], $A(\kappa_{ss} + (1/2)\kappa^3)$, is equivalent to that in (2.7) under the redefinition of the Lagrange multiplier: $\Lambda \to \Lambda + (3/2)A\kappa^2$.]

If we rescale lengths by L, time by the relaxation time $\zeta_\perp L^4/A$, and the Lagrangian multiplier by the elastic force A/L^2, then in dimensionless units Eq. (2.7) becomes

$$\boldsymbol{r}_t = \left(\kappa_{ss} - \kappa^3 + \kappa\Lambda\right)\hat{\boldsymbol{n}} + \eta\left(3\kappa\kappa_s - \Lambda_s\right)\hat{\boldsymbol{t}} \,. \tag{2.8}$$

If we now differentiate (2.8) with respect to arclength, separate the normal and tangent components, and notice that $\boldsymbol{r}_s \cdot \boldsymbol{r}_{ts} = 0$ to ensure local inextensibility ($\boldsymbol{r}_s \cdot \boldsymbol{r}_s = 1$), we obtain the coupled equations describing the evolution of the tangent angle, θ, and the tension, Λ,

$$\theta_t = -\theta_{ssss} - \left[\Lambda - 3\left(\eta+1\right)\theta_s^2\right]\theta_{ss} - \left(\eta+1\right)\Lambda_s\,\theta_s \,, \tag{2.9}$$

$$\Lambda_{ss} - \eta^{-1}\theta_s^2\Lambda = -\eta^{-1}\theta_s^4 + 3\theta_{ss}^2 + \left(3+\eta^{-1}\right)\theta_s\,\theta_{sss} \,, \tag{2.10}$$

in which we have used the relation $\theta_s = \kappa$.

It is important to note that in differentiating Eq. (2.8) with respect to the arclength, the boundary condition $\boldsymbol{r}(0,t) = \mathbf{0}$ is lost. One may naively try to retrieve it using some integral condition. For instance, for the Lagrange multiplier at the clamped end taking the dot product of Eq. (2.8) with the tangent unit vector, then integrating over the arclength, and finally imposing the boundary condition for Λ at the free end. However, this would not be a valid boundary condition, because it is simply the result of evaluating the governing equations and imposing a boundary condition known somewhere else. To restore the missing boundary condition physical insight is required. At $s = 0$, the filament is not only fixed, but, trivially, it has zero velocity, i.e. $\boldsymbol{r}_t(0,t) = \mathbf{0}$. This consideration then leads to the boundary conditions for $\theta(0,t)$ and $\Lambda(0,t)$ when directly evaluating Eq. (2.7) at $s = 0$. These are

$$\theta_{sss}(0,t) - \theta_s(0,t)^3 + \theta_s(0,t)\Lambda(0,t) = 0\,, \tag{2.11}$$

and

$$\Lambda_s(0,t) - 3\,\theta_s(0,t)\,\theta_{ss}(0,t) = 0\,, \tag{2.12}$$

respectively. The condition $\boldsymbol{r}_s(0,t) = \hat{\boldsymbol{e}}_x$ becomes $\theta(0,t) = 0$, while Eq. (2.3), $\theta_s(1,t) = 0$, and Eq. (2.4), $\theta_{ss}(1,t) = 0$ and $\Lambda(1,t) = \sigma$, where

$$\sigma \equiv \frac{\Gamma L^2}{A}\,, \tag{2.13}$$

is the dimensionless ratio between the strength of the force at the tip and the elastic force and is the one relevant parameter governing the dynamics of the filament. Note that since the force is compressive ($\Gamma > 0$), σ is always positive.

2.1.2 Dynamical features of a follower force

The nonvariational form of the follower force differs intrinsically from conventional Euler buckling in which the compressive force is always in a given direction. Examination of the equations of motion linearized around the straight filament, studied in much more detail in Sec. 2.2, reveals important physical insights into the expected dynamics. If y denotes the y component of the position of the filament, the linearized nondimensional form of Eq. (2.8) is classically given by

$$y_t = -y_{xxxx} - \Lambda y_{xx}\,. \tag{2.14}$$

If we calculate the rate of change of the (nondimensional) bulk energy

$$\mathscr{E} = \frac{1}{2}\int_0^1 \left(y_{xx}^2 - \Lambda y_x^2\right) \mathrm{d}x, \tag{2.15}$$

then repeated integrations by parts and imposition of the boundary condition (2.4) yields the result

$$\mathscr{E}_t^e = -\int_0^1 (y_{xxxx} + \Lambda y_{xx})^2 \, \mathrm{d}x - \sigma y_t(1)\, y_x(1)\,. \tag{2.16}$$

The integral term is clearly negative semi-definite, and absent the final term (as in Euler buckling) it would drive the energy monotonically downward. The boundary term arises from the fact that the follower force always acts tangentially, and it is clear that depending on its sign, the follower force either removes or injects energy into the system, eventually giving rise to persistent motion as discussed below.

2.1.3 Buckling and Flapping

The governing equations, Eqs. (2.9) and (2.10) together with the corresponding boundary conditions, were uniformly discretized using second-order centred finite differences in the bulk and one-sided differences at the edges. The resulting nonlinear system of algebraic equations was solved using Newton's method. To overcome the constraint of the time step arising from the stiff nature of Eq. (2.9), a backward Euler method, which is an implicit A-stable numerical scheme, was used [93]. The equations were decoupled using the values at the previous time step [94].

Numerical results for a horizontal filament to which a small perturbation was initially introduced identify three different dynamical behaviours depending on the value of σ, as illustrated in Fig. 2.2. For $\sigma \lesssim 20.4$, the filament returns monotonically to its original straight configuration (illustrated for $\sigma = 15$ as the blue solid line). In the interval $20.4 \lesssim \sigma \lesssim 37.5$, the filament displays decaying oscillations (the case with $\sigma = 33$ is shown in red dashed line). Finally, above the threshold $\sigma \gtrsim 37.5$, we find that any perturbation grows and the motion settles into a finite-amplitude periodic oscillation (see inset of Fig. 2.2 in the case $\sigma = 80$).

Inspecting in more detail the dynamics of the filament for $\sigma \gtrsim 37.5$ as shown in Fig. 2.3, we see that after a transient whose duration diminishes as the value of σ increases (Figs. 2.3a-b), the filament traces a self-sustained wave, reminiscent of the waving of spermatozoa flagella [95]. Interestingly, recent research [84] has shown that a follower force model could be used to explain such a wave-like beating of flagellates. The origin of such a waving motion however differs from the results presented here as it arises from the collective dynamics of the molecular motors against the flagellar load which cause sliding of adjacent filaments.

The filament buckles as the external force keeps compressing it in the tangential direction while both the elastic restorative force and the drag force oppose it, giving rise to this *flapping dynamics*. It is worth stressing that this novel dynamics arises from the presence of the fluid in the low Reynolds number regime. For an inertial filament with no fluid, the dynamics is

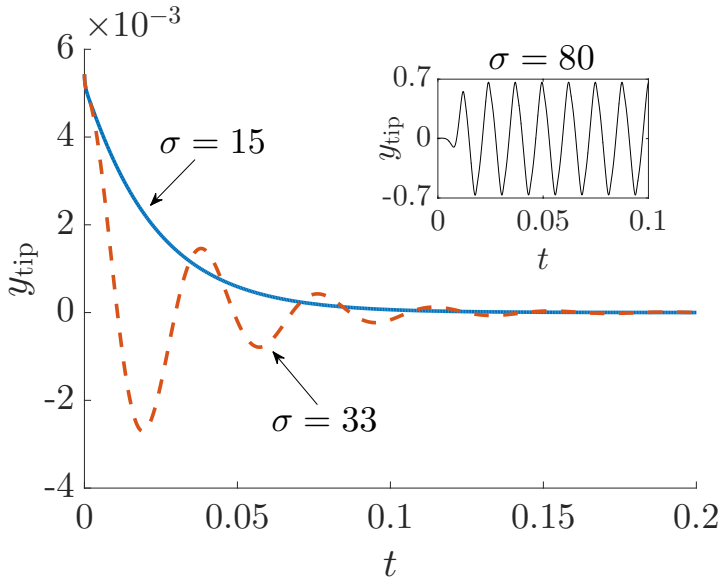

Fig. 2.2 Tip displacement as a function of time for three different values of σ. Blue solid line, $\sigma = 15$: the filament returns monotonically to its original shape. Red dashed line, $\sigma = 33$: after a transient, the oscillation dies out as the filament straightens. Inset: for $\sigma = 80$ the filament shows a sustained periodic oscillation.

indeed different [96]. We next plot in Fig. 2.3c the amplitude of the oscillations as a function of σ. The tip displacement shows a clear Hopf bifurcation before reaching a plateau (a consequence of the finite length of the filament). The frequency of oscillation, which was computed applying the FFT to the time evolution of the tip displacement, grows roughly linearly with σ (Fig. 2.3d).

2.2 Linear Stability Analysis

The numerical results in the previous section reveal that increasing values of σ are accompanied by a transition from stability to decaying oscillations, and finally a Hopf bifurcation to flapping dynamics. We now turn to a theoretical analysis of this transition.

In order to study buckling instabilities, linear stability analysis has been exploited in several contexts, spanning from column buckling under compression – a variant of Euler buckling – with different boundary conditions (e.g. clamped-free, hinged-free, hinged-hinged, clamped-clamped) [62, 96], to filament buckling in linear shear flow [92] or extensional flows [91, 90, 97, 98]. Because the follower force compresses the filament, a certain critical value above which the filament buckles is expected to exist. Here, linear stability analysis is used to analytically compute the critical compression force.

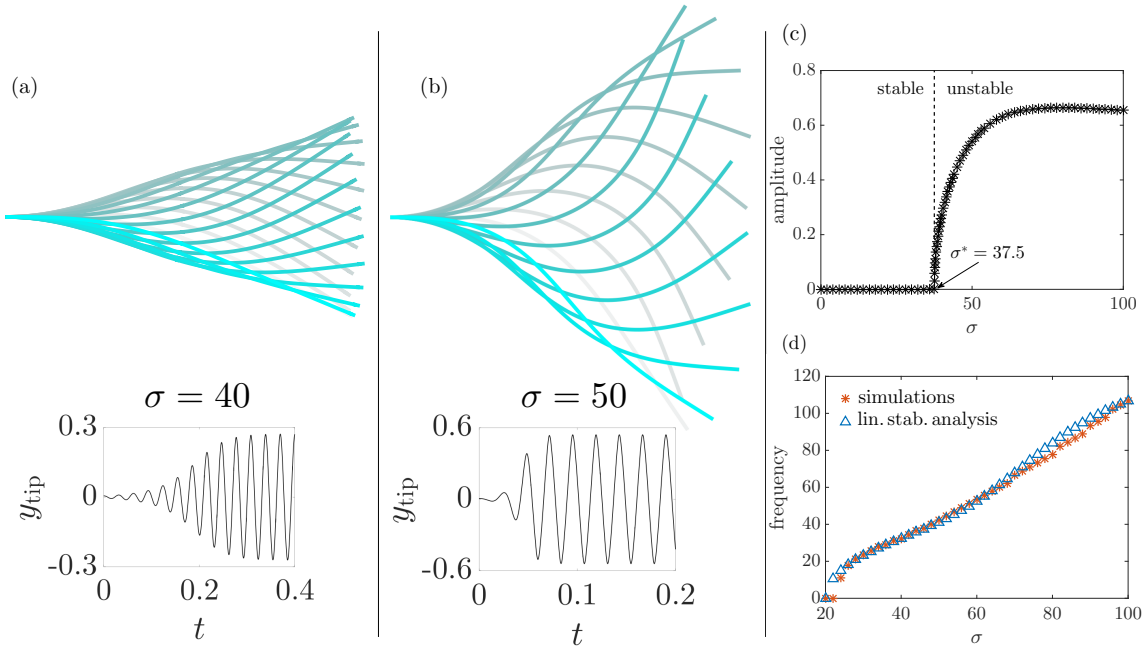

Fig. 2.3 Time-lapse of the flapping filament over a period and time evolution of the tip displacement (inset) for different values of σ as obtained numerically; (a): $\sigma = 40$, (b): $\sigma = 50$. The transient required to reach the finite-amplitude periodic oscillations decreases while the amplitude of the oscillations increases with σ. (c): Amplitude of the tip displacement as function of σ. At $\sigma \approx 37.5$, the system becomes unstable and exhibits self-sustained oscillations. (d): Comparison between the frequency of oscillation of the filament for different values of σ obtained from the numerical simulations (red stars) and linear stability analysis (blue triangles).

Assuming small deviations from the initial, straight configuration, Eq. (2.6) simplifies as $x \approx s$, $\hat{\boldsymbol{t}} \approx (1, y_x)$, and $\hat{\boldsymbol{n}} \approx (y_x, -1)$. The problem then turns from solving the two coupled nonlinear equations (2.9) and (2.10) to $\Lambda_x = 0$, with $\Lambda(1,t) = \sigma$, which leads to $\Lambda(x,t) = \sigma$, and

$$y_t = -y_{xxxx} - \Lambda y_{xx}\,, \tag{2.17}$$

with the boundary conditions

$$y(0,t) = y_x(0,t) = y_{xx}(1,t) = y_{xxx}(1,t) = 0\,. \tag{2.18}$$

Euler firstly studied the buckling of an ideal column with centrally applied load and computed the critical load by studying the behaviour of the column when subject to a small oscillation [99]. In order to study buckling of a slender column subject to an axial load other approaches are also possible. One can assume the existence of a buckled shape for the column, for which the displacement of the free end is defined to be h. In dimensionless form,

the relation between the curvature and the bending moment is

$$y_{xx} = \sigma\,(h-y)\,, \tag{2.19}$$

which is to be solved with the boundary conditions $y(0) = y_x(0) = 0$ and requiring $y(1) = h$. This is satisfied when

$$\cos\sqrt{\sigma} = 0\,, \tag{2.20}$$

leading to the well-known critical value $\sigma_{\rm cr} = \pi^2/4$.

Another method consists in studying the alternate form of the differential equation that expresses the curvature of the slender column in terms of the bending moment, namely

$$y_{xxxx} + \Lambda y_{xx} = 0\,, \tag{2.21}$$

as lateral loads vanish [65]. The general solution is

$$y(x) = C_1 \sin\sqrt{\sigma}x + C_2\cos\sqrt{\sigma}x + C_3 x + C_4\,, \tag{2.22}$$

where C_j, with $j = 1,2,3,4$, are the integration constants. In this case, there are four boundary conditions to be imposed that lead to four equations. At the clamped end we have $y(0) = y_x(0) = 0$, while at the free end $y_{xx}(1) = 0$ and $y_{xxx}(1) + \sigma y_x(1) = 0$, which translate into the conditions that the bending moment and the shearing force must be zero. By solving the linear system of four equations in four unknowns, we obtain again the condition $\cos\sqrt{\sigma} = 0$, thus showing agreement between all different approaches presented thus far.

If these analyses were to be applied to the case of a follower force, a few important aspects should be noted. (i) Since the follower force is nonconservative, the final buckled shape depends on the path taken to get there. Hence, it is not possible to consider the buckled configuration of the filament and compute the critical load via the condition at the free end. (ii) The boundary conditions $y(0,t) = y_x(0,t) = y_{xx}(1,t) = y_{xxx}(1,t) = 0$ lead to four equations that are satisfied only when the four coefficients C_j are equal to zero, which corresponds to the straight configuration. The aforementioned approaches, which can be defined as static since they do not consider the dynamics of the system, prove to be inadequate for nonconservatice forces [65, 96].

For systems with nonconservative forces in inertia-dominated problems, the critical value at which the beam buckles and becomes unstable has been computed using a dynamic criterion [100, 65]. Here, we extend the analysis to the viscous-dominated regime.

We start by assuming a solution to the linearised problem, Eq. (2.17), of the form

$$y(x,t) = \hat{y}(x)\,\mathrm{e}^{\omega t}\,, \tag{2.23}$$

where ω is the growth rate. This leads to the ordinary differential equation (ODE)

$$\hat{y}_{xxxx} + \sigma\hat{y}_{xx} + \omega\hat{y} = 0\,, \tag{2.24}$$

whose general solution is given by

$$\hat{y}(x) = C_1\cosh\alpha_1 x + C_2\sinh\alpha_1 x + C_3\cos\alpha_2 x + C_4\sin\alpha_2 x\,, \tag{2.25}$$

with

$$\alpha_1 = \sqrt{\sqrt{\frac{\sigma^2}{4} - \omega} - \frac{\sigma}{2}}\,, \tag{2.26}$$

$$\alpha_2 = \sqrt{\sqrt{\frac{\sigma^2}{4} - \omega} + \frac{\sigma}{2}}\,. \tag{2.27}$$

The values of the constants C_j are obtained by imposing the boundary conditions in Eq. (2.18), leading to a standard 4×4 matrix whose determinant is required to be zero. After some simplifications, the equation for the growth rate, ω, can be shown to read

$$\sigma^2 - 2\omega\,(1+\cosh\alpha_1\cos\alpha_2) + \sigma\sqrt{-\omega}\sinh\alpha_1\sin\alpha_2 = 0\,, \tag{2.28}$$

which, with the α_i defined in (2.27), does not have a closed-form solution, but can be easily solved numerically.

Alternatively, we can also solve Eq. (2.24) numerically, viewed either as a boundary value problem or as an eigenvalue problem. In the former case, a shooting method is used with the appropriate initial guess in the neighbourhood of the first transition ($\sigma \approx 20.05$). In the latter, the problem turns into solving $\mathscr{L}\hat{y} = \omega\hat{y}$. The operator $\mathscr{L} \equiv -\mathrm{d}^4/\mathrm{d}x^4 - \sigma\mathrm{d}^2/\mathrm{d}x^2$ is discretized using centred finite differences in the bulk of the stencil and sided differences at the ends, and the eigenvalues are determined with the QR algorithm. Both methods were implemented and used to test the results obtained from the numerical solution of Eq. (2.28), showing excellent agreement.

The linear stability results identify three different behaviours as a function of the value of σ. These are illustrated in Fig. 2.4 where we plot the real part (blue triangles) and imaginary part (red stars) of the computed growth rate, ω. The former represents the rate of growth

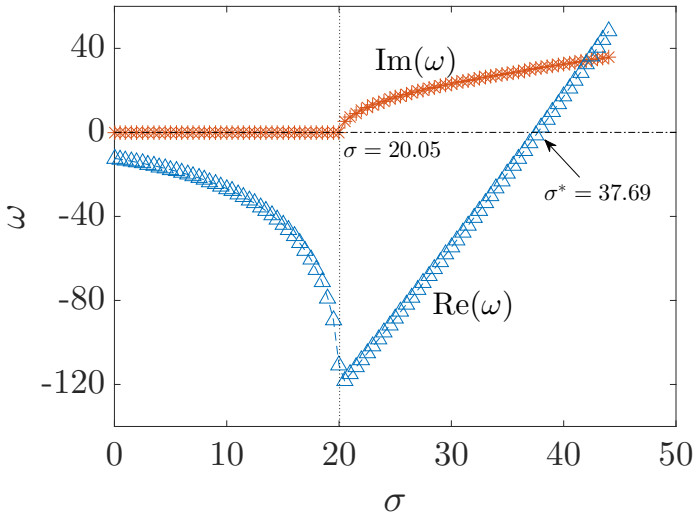

Fig. 2.4 Imaginary part (corresponding to the frequency of oscillation) and real part (associated with the rate of growth of the perturbation) of ω as function of σ. The frequency becomes complex at $\sigma \approx 20.05$, giving rise to oscillations in the filament dynamics. The real part remains negative (stability) until $\sigma \approx 37.69$, after which it becomes positive (instability).

(or decay) of the perturbation, while the latter the frequency of oscillation, which is also the frequency of beating. When $\sigma \lesssim 20.05$, the growth rate is negative and $y(x,t)$ decays exponentially. Starting at $\sigma \gtrsim 20.05$, the growth rate becomes complex, but its real part remains negative, consistent with the numerical results from the previous section showing oscillatory decay. The real part of the growth rate finally becomes positive at a critical value, $\sigma^* \approx 37.69$ (Fig. 2.4), indicating the onset of the instability and the bifurcation to oscillations about the horizontal, straight configuration.

The comparison between the numerical results and linear stability analysis shows a very good agreement not only for the critical value of σ at which the oscillations arise ($\sigma = 20.4$ vs. 20.05) and at which the system becomes unstable ($\sigma^* = 37.5$ vs. 37.69), but also for the frequency of oscillations (see Fig. 2.3b). Notably, the frequencies are in good agreement also for large values of σ when linear stability analysis does not strictly apply. The reason for the effectiveness of linear stability analysis can be that the onset of the instability is computed considering a slightly perturbed shape around the straight configuration, hence nonlinear effects are minimal.

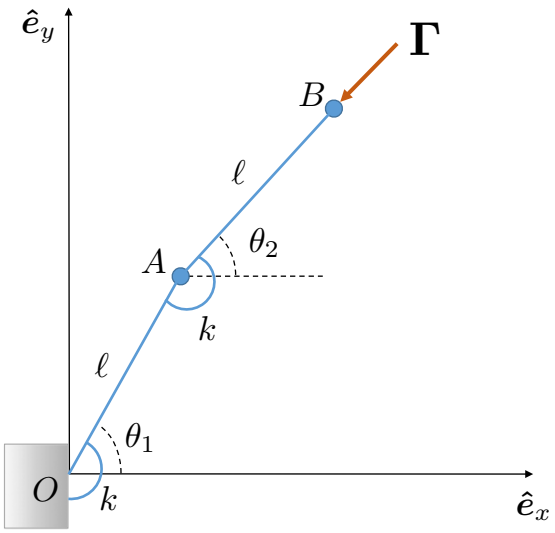

Fig. 2.5 Discrete model: Two links of length ℓ rotate with degrees of freedom θ_1 and θ_2 around torsional springs of strength k and are acted upon by a follower force $\boldsymbol{\Gamma}$.

2.3 Two-link filament model

Having shown that the linear stability analysis of the elastohydrodynamic PDEs can explain the onset of the flapping dynamics, we now consider a simpler two-link filament model, in a manner similar to the case in which damping is negligible [101, 81], with the aim of illustrating in a low-dimensional dynamical system the origin of oscillatory motion.

We consider a simple discrete model for an elastic filament composed of two rigid links of length ℓ joined together at point A and constrained to remain in the plane $z = 0$ (see Fig. 2.5). Elasticity is included by introducing two torsional springs, each with spring constant k. The two degrees of freedom of the system are the angles $\theta_1(t)$ and $\theta_2(t)$ that define the configuration of the links. They are zero when both rods are horizontal and increase in the clockwise direction. The follower force, $\boldsymbol{\Gamma}$, acts at the tip of the second rod, always pointing tangentially along it. The filament moves in a creeping flow and its drag force is assumed to be concentrated at points A and B only.

For this model, the locations of points A and B are

$$\boldsymbol{r}_A = A - O = \ell\,(\cos\theta_1, \sin\theta_1)\,, \tag{2.29}$$

$$\boldsymbol{r}_B = B - O = \ell\,(\cos\theta_1 + \cos\theta_2, \sin\theta_1 + \sin\theta_2)\,, \tag{2.30}$$

and their velocities are

$$\boldsymbol{v}_A = \dot{\boldsymbol{r}}_A = \ell\,\dot{\theta}_1(-\sin\theta_1, \cos\theta_1)\,, \tag{2.31}$$

$$\boldsymbol{v}_B = \dot{\boldsymbol{r}}_B = \ell\,[\dot{\theta}_1(-\sin\theta_1, \cos\theta_1) + \dot{\theta}_2(-\sin\theta_2, \cos\theta_2)]\,, \tag{2.32}$$

where the dot denotes time derivative. The follower force is defined as $\boldsymbol{\Gamma} = -\Gamma\hat{\boldsymbol{t}}$, with $\Gamma > 0$ its magnitude and $\hat{\boldsymbol{t}} = (\cos\theta_2, \sin\theta_2)$ the unit tangent vector joining A and B. Under the assumption of creeping flow, the drag forces are $\boldsymbol{F}_A = -\zeta\boldsymbol{v}_A$ and $\boldsymbol{F}_B = -\zeta\boldsymbol{v}_B$, with ζ some effective drag coefficient, while the restoring moments due to the torsion springs acting on the two rods are $-k\theta_1$ at point O and $-k(\theta_2 - \theta_1)$ at point A.

The equations of motion are obtained applying the principle of virtual work

$$\boldsymbol{\Gamma}\cdot\delta\boldsymbol{r}_B + \boldsymbol{F}_B\cdot\delta\boldsymbol{r}_B + \boldsymbol{F}_A\cdot\delta\boldsymbol{r}_A - k\theta_1\delta\theta_1 - k(\theta_2-\theta_1)(\delta\theta_2 - \delta\theta_1) = 0\,, \tag{2.33}$$

where $\delta\boldsymbol{r}_B, \delta\boldsymbol{r}_A, \delta\theta_1$ and $\delta\theta_2$ are the virtual displacements. Substituting the terms with their aforementioned definitions, we end up with a scalar equation where we can group the terms multiplied by $\delta\theta_1$ and $\delta\theta_2$. Invoking their arbitrariness, we obtain

$$\Sigma\sin(\theta_1-\theta_2) - [2\dot{\theta}_1 + \dot{\theta}_2\cos(\theta_1-\theta_2)] - 2\theta_1 + \theta_2 = 0\,, \tag{2.34}$$

$$-\dot{\theta}_1\cos(\theta_1-\theta_2)\dot{\theta}_2 + \theta_1 - \theta_2 = 0\,, \tag{2.35}$$

where time was rescaled by $\tilde{t} = kt/\zeta\ell^2$, and we introduced the controlling dimensionless number, $\Sigma = \Gamma\ell/k$, playing a role similar to σ in the previous section. Note that if we enforce $\theta_1 = \theta_2 = \theta$, then the previous equations reduce to

$$3\dot{\theta} + \theta = 0\,, \tag{2.36}$$

which shows that the follower force, which always points inward, does not play any role and that θ decays exponentially, as we would expect.

We solved Eqs. (2.34)-(2.35) numerically using the Matlab ODE solver 'ode45', which is based on an explicit Runge-Kutta (4,5) formula and is suitable in this case as the equations are non-stiff [102]. The initial conditions are random, small perturbations to both angles.

Our numerical results, shown in Fig. 2.6, indicate that, again, three different dynamics are possible. With increasing values of Σ, the system goes from asymptotic stability ($\Sigma < 2$), to stability with oscillations ($2 \leq \Sigma < 3$), to exhibiting stable, self-sustained oscillations ($\Sigma \geq 3$).

In order to capture these transitions, we may again take advantage of linear stability. By linearising the equations of motion about the equilibrium configuration $\theta_1 = \theta_2 = 0$, and

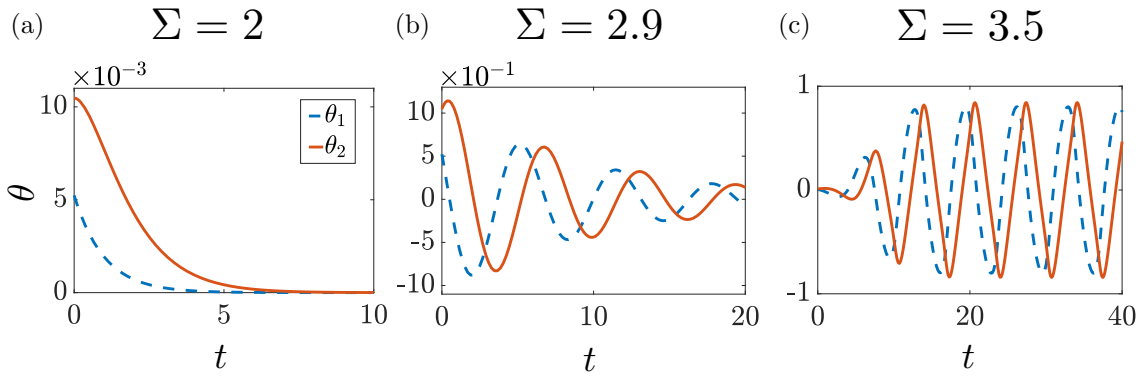

Fig. 2.6 Time evolution of θ_1 (blue dashed line) and θ_2 (red solid line) obtained by solving numerically the nonlinear equations of motion. (a): The system is asymptotically stable ($\Sigma = 2$); (b): Stability with oscillations ($\Sigma = 2.9$); (c): Stable, self-sustained oscillations ($\Sigma = 3.5$).

assuming solutions of the form $\theta_j = \hat{\theta}_j e^{\omega \tilde{t}}$ we obtain

$$\Sigma(\hat{\theta}_1 - \hat{\theta}_2) - \omega(2\hat{\theta}_1 + \hat{\theta}_2) - 2\hat{\theta}_1 + \hat{\theta}_2 = 0, \tag{2.37}$$

$$-\omega(\hat{\theta}_1 + \hat{\theta}_2) + \hat{\theta}_1 - \hat{\theta}_2 = 0, \tag{2.38}$$

and non-trivial solutions are found when the determinant of the corresponding matrix is zero, namely $\omega^2 + 2(3-\Sigma)\omega + 1 = 0$, whose solutions are

$$\omega_\pm = \Sigma - 3 \pm \sqrt{(\Sigma - 4)(\Sigma - 2)}. \tag{2.39}$$

We may then use Eq. (2.39) to predict the dynamics, and we obtain five different cases:

a. if $\Sigma \leq 2$, then $\omega_\pm < 0$, and the system is stable;

b. for $2 < \Sigma < 3$, $\mathrm{Re}(\omega_\pm) < 0$ and $\mathrm{Im}(\omega_\pm) \neq 0$, so the perturbations die away in an oscillatory manner,

c. if $\Sigma = 3$, then $\mathrm{Re}(\omega_\pm) = 0$ and $\mathrm{Im}(\omega_\pm) \neq 0$, hence the system is stable and shows periodic oscillations with constant amplitude;

d. for $3 < \Sigma < 4$, $\mathrm{Re}(\omega_\pm) > 0$ and $\mathrm{Im}(\omega_\pm) \neq 0$, and thus we obtain exponentially-growing oscillations;

e. when $\Sigma \geq 4$, $\omega_\pm > 0$, i.e. the system is unstable and θ_1, θ_2 simply diverge.

In cases d-e, the linear instability saturates to nonlinear self-sustained oscillations when the full nonlinear equation is considered. Once again, linear stability is thus in good agreement with the results from the nonlinear equations of motion.

In conclusion, the two-link model studied in this section captures the dynamics of the full nonlinear elastohydrodynamic problem. In particular, we have shown that when $\Sigma = \Gamma\ell/k \geq 3$, which represents, analogously to σ, the ratio between the strength of the follower force and the elastic force, self-sustained oscillations are indeed possible.

2.4 Physical interpretation

The analysis in Sec. 2.1.2 showed that the boundary term of the RHS of Eq. (2.16) arises from the nonvariational nature of the follower force. Here we simulate the full nonlinear elastohydrodynamics equations and demonstrate that it is indeed the term responsible for the self-sustained motion observed.

Choosing the value $\sigma = 37.8$ allows the tip oscillations to remain small. We plot in Fig. 2.7a the values of the tip velocity, $y_t(1)$, slope, $y_s(1)$, and their product. Over the period of oscillation T, which is defined such that the tip displacement is maximum at $t = 0$, the tip reaches the minimum at $t = T/2$ and crosses the x-axis twice, with minimum and maximum speeds at $t = T/4$ and $t = 3T/4$, respectively. In contrast, the filament tangent at the tip, $y_s(1)$, has its maximum value at about $t = T/8$ and minimum at about $t = 5T/8$, becoming zero slightly before $t = 3T/8$ and $t = 7T/8$.

While the term $-\sigma y_t(1)\, y_s(1)$ is positive, it injects energy into the system until the tangent at the tip crosses the x-axis. At this point, it becomes negative and it therefore withdraws energy until the tip reaches its minimum displacement. Afterwards, it becomes positive again and the cycle repeats, but with the mirrored configuration ($T/2 < t < T$). For reference, we show in Fig. 2.7b the filament configuration over a half-period.

In order to better understand this dynamics, we may also exploit the two-link model previously studied, with dynamics illustrated Fig. 2.7c for $\Sigma = 3.5$. Initially, the follower force compresses the two-link structure and the links are pushed downward ($0 < t < T/4$). Then, the first link reaches its lowest point (i.e. highest restorative moment) and stops moving, while the second link keeps rotating ($t = 3T/8$). By doing so, the follower force, which has followed the second link, exerts a lower moment and the restorative effect becomes predominant. Hence, the first link moves upwards and the second link downwards until stopping and inverting its motion ($t = T/2$). This dynamics repeat periodically and prevents the establishment of a steady state.

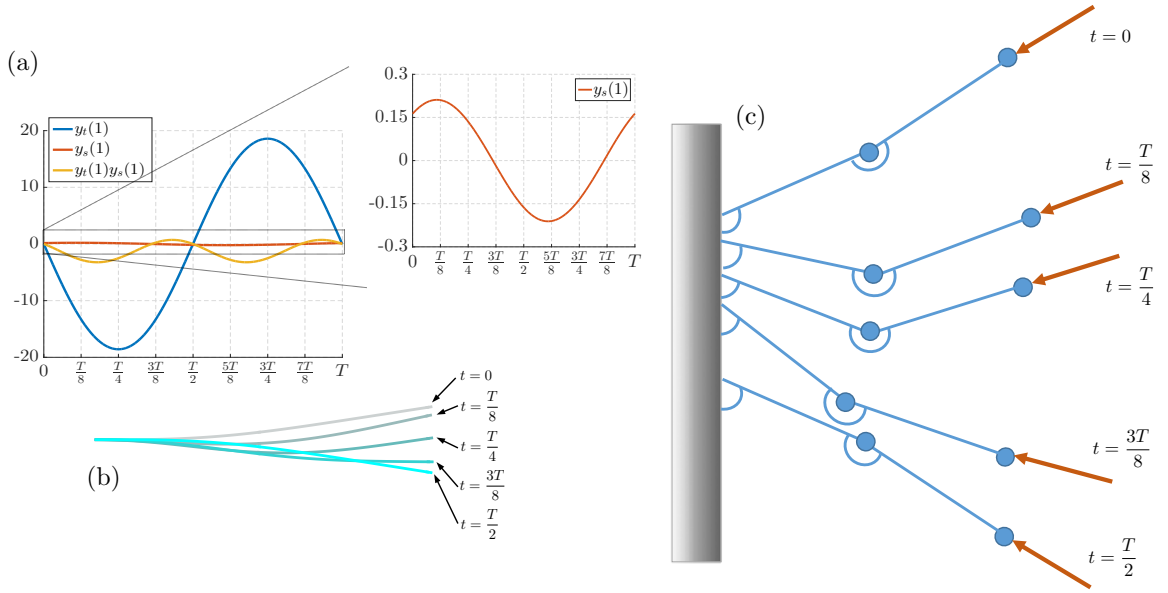

Fig. 2.7 Nonvariational aspects of flapping motion. (a) Time evolution of the tip velocity, $y_t(1)$, its derivative with respect to the arclength, $y_s(1)$, (zoomed in the inset) and their product, $y_t(1)\,y_s(1)$ over the period of oscillation T for $\sigma = 37.8$. The term $y_t(1)\,y_s(1)$ changes sign four times over a cycle: the presence of the follower force both removes and injects energy into the system, giving rise to self-sustained, periodic oscillations. (b) Filament configuration over a half-period. (c) Schematic of the two-link model at different times over a half-period for $\Sigma = 3.5$. The follower force compresses the two-link structure and the links are pushed downward ($0 < t < T/4$). Then, the first link reaches its lowest point (i.e. highest restorative moment) and stops moving, while the second link keeps rotating ($t = 3T/8$). By doing so, the follower force, which has followed the second link, exerts a lower moment and the restorative effect becomes predominant. Hence, the first link moves upwards and the second link downwards until stopping and inverting its motion ($t = T/2$). The cycle then repeats.

By examining both the continuous and discrete models, we thus see that the effect of the follower force is to constantly inject and remove energy into the system, thus preventing any stable configuration to be reached and giving rise to periodic, self-sustained oscillations.

2.5 Discussion

Inspired by experimental observations of persistent waving motion of MTs driven by molecular motors, particularly during oocyte development in *Drosophila* [1], we have explored the simplest model of motor-driven filament motion. In this "follower-force" model, a compressive motor force $\mathbf{\Gamma}$ acts tangentially at the free end of the filament whose shape is found by balancing the forcing with elasticity and low-Reynolds number fluid drag. Numerical

studies of the full nonlinear elastohydrodynamics equations led to the discovery of a flapping instability that arises as the control parameter, $\sigma = \Gamma L^2/A$, is varied. As is typically the case in a Hopf bifurcation, the linearized filament dynamics first develops damped oscillations at an intermediate value of σ before exhibiting self-sustained limit cycle motion beyond some critical value, σ^*, both of which are also well captured by a linear stability analysis.

Motivated by these findings, we then proposed as a simplified model a discrete two-link system in which elasticity was included via two torsion springs. Linear stability analysis of this simpler dynamical system identified five different regions depending on the value of the control parameter $\Sigma = \Gamma\ell/k$, in full agreement with the results of numerical simulations.

Lastly, we were able to shed light on the physics underlying such oscillations by analysing the linearized equations of motion.

2.6 Conclusions

Despite capturing the essence of the waving motion observed in experiments, this minimalistic fluid-structure interaction model lacks of some key features possessed by the real biological system. Namely, motors are not necessarily located at the end of the tip, they are typically in large number on each MT, and while moving, they set a fluid flow. These extensions will be tackled in Chapter 3.

Chapter 3

Model extensions to the individual dynamics

In this chapter, we extend the framework presented in Chapter 2 to more realistic instances appropriate to *Drosophila* oocytes streaming. In Sec. 3.1, we include the flow generated by the motors, essential in giving rise to cytoplasmic streaming. Since motors constantly translocate along MTs, their position is likely to be somewhere other than the filament tip. We develop a suitable theoretical model and present its numerical implementation in Sec. 3.2. Finally, Sec. 3.3 tackles the problem of having a multitude of motors along a filament, a scenario that is much more plausible in reality than the case of a single motor.

3.1 Fluid-entraining follower force

When molecular motors translocate along MTs they not only exert a force on the filament, but also entrain fluid as they carry cargo. While the motor-induced force on the filament was included in the analysis of Chapter 2, the fluid flow created by the motor and the associated drag on the filament were neglected. Here we include these effects by approximating cargo-motor assembly as a point force located at the tip of the filament, so that the three-dimensional (3D) flow that arises is that of a stokeslet [58]. As at the tip we now have both a concentrated load acting on the filament (the follower force) and a concentrated force setting the flow, we refer to this combination as 'fluid-entraining' follower force (see illustration in Fig. 3.1).

3.1.1 Equations of motion

While walking along the MT towards its free end, the molecular motor-cargo ensemble creates a flow that follows its direction of motion while applying a force on the filament in

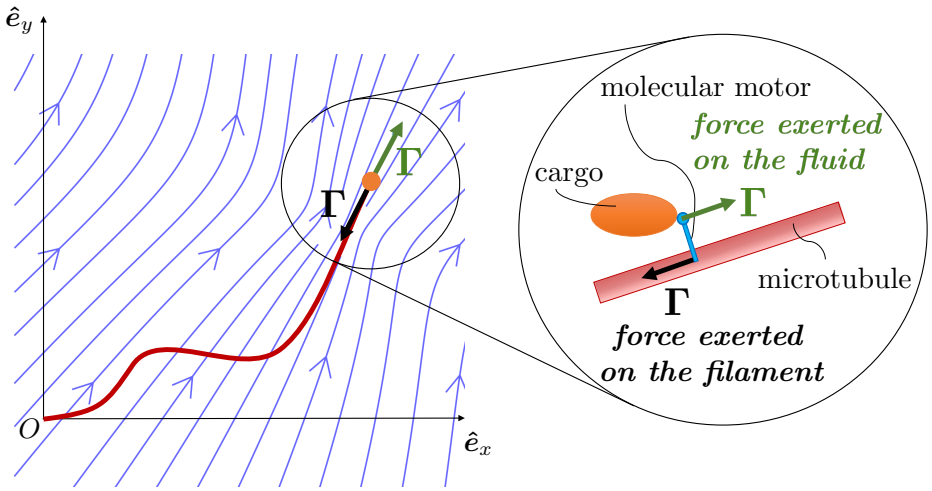

Fig. 3.1 A filament clamped on one side ($s = 0$) and subject to a 'fluid-entraining' follower force at the other end ($s = L$). At the tip, the compressive follower force acts on the filament (black arrow) while the moving cargo acts on the surrounding fluid as a point force (green) creating the flow with streamlines illustrated in blue. Inset: A detailed picture of the forces acting on the filament and the fluid.

the opposite direction. As specified in Chapter 1, we assume the link between the filament and the cargo to be rigid. Since the magnitude of the force exerted on the filament while the molecular motor walks along it is Γ, a simple force balance shows that the force exerted on the fluid also has strength Γ (inset of Fig. 3.1). The fluid flow on the filament centreline created by the point force at $s = L$ is therefore $\boldsymbol{u}(s) = (1/8\pi\mu)\,\boldsymbol{G}(s;L)\cdot\Gamma\hat{\boldsymbol{t}}(L)$, where $\boldsymbol{G}(s;L)$ is the Green's tensor (with dimensions of inverse length) appropriate to the boundary conditions imposed on the fluid equations. We consider the 3D fluid flow created by a point force in an unbounded domain, and thus ignore the presence of any boundary (though the analysis could be repeated in this case along the same lines).

To take into account the motion of the filament, we exploit again the RFT approximation where we neglect nonlocal effects to facilitate the mathematical treatment as accuracy is not the main objective of this study. Using such an approximation, the hydrodynamic force per unit length acting on the filament in the presence of a background flow is given by

$$\boldsymbol{f}_{\mathrm{h}} = -\left(\zeta_{\parallel}\hat{\boldsymbol{t}}\hat{\boldsymbol{t}} + \zeta_{\perp}\hat{\boldsymbol{n}}\hat{\boldsymbol{n}}\right)\cdot(\boldsymbol{r}_t - \boldsymbol{u})\,, \tag{3.1}$$

and thus the equations of motion become

$$-A\boldsymbol{r}_{ssss} - (\Lambda\boldsymbol{r}_s)_s = \left(\zeta_{\parallel}\hat{\boldsymbol{t}}\hat{\boldsymbol{t}} + \zeta_{\perp}\hat{\boldsymbol{n}}\hat{\boldsymbol{n}}\right)\cdot(\boldsymbol{r}_t - \boldsymbol{u})\,, \tag{3.2}$$

or, in dimensionless form,

$$\left(\eta^{-1}\hat{\boldsymbol{t}}\hat{\boldsymbol{t}}+\hat{\boldsymbol{n}}\hat{\boldsymbol{n}}\right)\cdot\left(\boldsymbol{r}_t-\xi\sigma\boldsymbol{u}\right)=-\boldsymbol{r}_{ssss}-\left(\Lambda\boldsymbol{r}_s\right)_s\,, \tag{3.3}$$

that can be rearranged as

$$\boldsymbol{r}_t=\left(\kappa_{ss}-\kappa^3+\kappa\Lambda\right)\hat{\boldsymbol{n}}+\eta\left(3\kappa\kappa_s-\Lambda_s\right)\hat{\boldsymbol{t}}+\xi\,\sigma\,\boldsymbol{u}\,, \tag{3.4}$$

where $\xi=\zeta_\perp/8\pi\mu$.

The Green's function for a point force in an unbounded domain is the stokeslet, presented in Sec. 1.3 which we here report for completeness, $\boldsymbol{G}(\boldsymbol{x};\boldsymbol{x}_0)=\frac{\boldsymbol{I}+\hat{\boldsymbol{R}}\hat{\boldsymbol{R}}}{|\boldsymbol{R}|}$. $\boldsymbol{I}$ is the identity tensor, $\boldsymbol{R}=\boldsymbol{x}-\boldsymbol{x}_0$ the vector pointing from the location of the point force to that of the point where we desire calculating the Green's function, and $\hat{\boldsymbol{R}}$ its unit vector. In 2D, it is a 2×2 matrix singular at the location of the point force, $\boldsymbol{x}=\boldsymbol{x}_0$, or, in terms of the arclength, at $s=L$. Clearly, a regularization is needed in order to avoid overestimating the magnitude of the velocity produced by the point force. To achieve this, we use the expression for a regularized Stokeslet derived by Cortez et al. [103, 104], characterized by a single regularization parameter ε.

In order to set the value of ε, we use the following physical argument. The velocity field at a distance r from a regularized point force with strength F decays as $u\sim F/8\pi\mu(r+\varepsilon)$. We require that the magnitude of the fluid flow at the location of the point force, $F/8\pi\mu\varepsilon$, be equal to the motor speed u_{motor}. In order to determine ε we thus need to know the magnitude of the point force, the speed of the molecular motor, and the viscosity of the medium. Typical speeds of molecular motors in animals are fractions of microns/sec, while the forces they exert are on the piconewton scale, as Svoboda & Block successfully measured [72]. In their work, they determined the force-velocity curve of single kinesin molecules using optical trapping interferometry by tracking their movement and applying pN-sized forces in an in vitro motility assay [72]. Our work was inspired by phenomena involving cytoplasmic streaming in *Drosophila* oogenesis, where the measured viscosity can reach $\mu\approx1$ Pa s [1], three orders of magnitude larger than water. Considering the full range of viscosities we obtain $\varepsilon\approx10^{-7}-10^{-4}$ m, the smaller values associated with the higher viscosities. Adopting the value 10^{-6} m as representative of the situation in *Drosophila*, we see that $\varepsilon/L\sim0.05-0.1$ as MTs are usually some $10-20$ μm long [1].

Let $\tilde{\boldsymbol{u}} = \tilde{\boldsymbol{G}}(s;1)\cdot\hat{\boldsymbol{t}}(1)$, with $\tilde{\boldsymbol{G}}(s;1)$ being the regularized Green's tensor [103, 104]. The generalization of Eqs. (2.9) and (2.10) to the fluid-entraining force is

$$\begin{aligned} \theta_t &= -\theta_{ssss} - \left[\Lambda - 3\,(\eta+1)\,\theta_s^2\right]\,\theta_{ss} - (\eta+1)\,\Lambda_s\,\theta_s - \xi\,\sigma\,\tilde{\boldsymbol{u}}_s\cdot\hat{\boldsymbol{n}}\,, \quad (3.5)\\ \Lambda_{ss} - \eta^{-1}\theta_s^2\Lambda &= -\eta^{-1}\theta_s^4 + 3\theta_{ss}^2 + \left(3+\eta^{-1}\right)\theta_s\,\theta_{sss} + \eta^{-1}\xi\,\sigma\,\tilde{\boldsymbol{u}}_s\cdot\hat{\boldsymbol{t}}\,. \quad (3.6)\end{aligned}$$

While the boundary conditions at the free end remain the same, an evaluation of Eq. (3.3) at $s=0$ shows that the presence of the background flow leads to the condition

$$\theta_{sss}(0,t) - \theta_s(0,t)^3 + \theta_s(0,t)\Lambda(0,t) + \xi\,\sigma\,\tilde{\boldsymbol{u}}(0,t)\cdot\hat{\boldsymbol{n}}(0,t) = 0\,, \quad (3.7)$$

for the tangent angle and

$$\Lambda_s(0,t) - 3\,\theta_s(0,t)\,\theta_{ss}(0,t) - \eta^{-1}\xi\,\sigma\tilde{\boldsymbol{u}}(0,t)\cdot\hat{\boldsymbol{t}}(0,t) = 0\,, \quad (3.8)$$

for the Lagrange multiplier. Note that while in this section we ignore the presence of any boundaries from a hydrodynamic standpoint, the value of $\tilde{\boldsymbol{u}}(0,t)$ would be set to zero if the Green's function used was the one which includes the presence of the wall at the clamped end to satisfy the no-slip boundary condition [105, 104, 106]. Fig. 3.2 shows this set-up, which we will refer to as 'fluid-entraining follower force with wall' throughout.

It should be noticed that the Green's function is written in Cartesian coordinates $\boldsymbol{R}(x,y)$. To calculate the background flow $\tilde{\boldsymbol{u}}$ for then solving Eqs. (3.5)-(3.6) with the corresponding boundary conditions, we need to transform the arclength in Cartesian coordinates. For this, we use the definitions

$$\frac{\mathrm{d}x}{\mathrm{d}s} = \cos\theta\,, \qquad \frac{\mathrm{d}y}{\mathrm{d}s} = \sin\theta\,, \quad (3.9)$$

which lead to

$$x(s) = x(0) + \int_0^s \cos\theta(s')\,\mathrm{d}s'\,, \qquad y(s) = y(0) + \int_0^s \sin\theta(s')\,\mathrm{d}s'\,. \quad (3.10)$$

3.1.2 Numerical implementation

To overcome the stiffness of the equations that dictates the constraint on the time step, implicit-explicit (IMEX) schemes can be adopted to stably solve the discretized equations of motion [107]. Among them, a second-order three level backward differentiation scheme, which will be referred to as SBDF (semi-implicit backward differentiation formula), was used. For its stability and accuracy, SBDF has become the standard scheme for fluid-structure interaction problems at low Reynolds number [94, 108, 109]. For completeness, we report

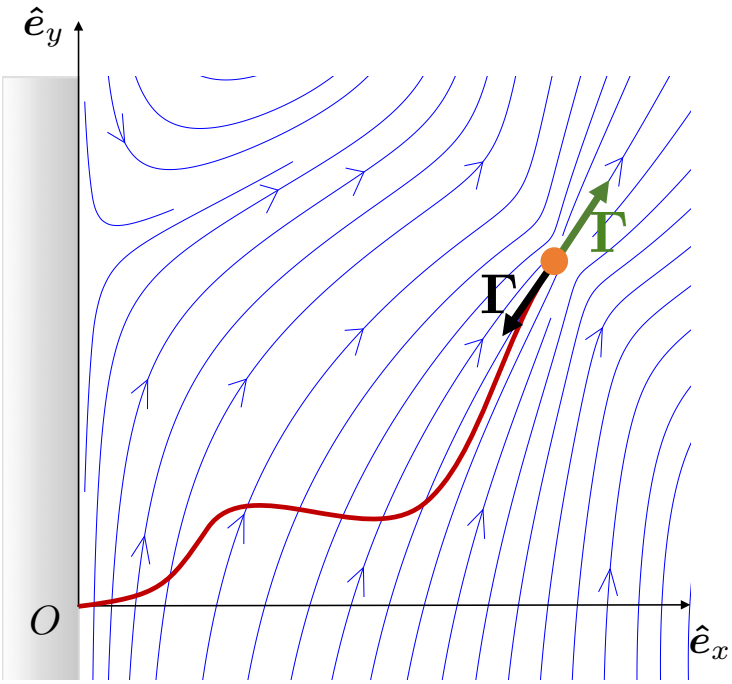

Fig. 3.2 Schematic of a filament clamped at $s = 0$ and subject to a fluid-entraining follower force with wall. The fluid flow created, whose streamlines are drawn in blue, is the solution of Stokes equations for a stokeslet near the wall [105].

here its formulation

$$\frac{1}{\Delta t}\left(\frac{3}{2}\theta^{n+1} - 2\theta^{n} + \frac{1}{2}\theta^{n-1}\right) = -\theta_{ssss}^{n+1} + 2g^{n} - g^{n-1}\,, \tag{3.11}$$

$$\Lambda_{ss}^{n} - \eta^{-1}\left(\theta_{s}^{n}\right)^{2}\Lambda^{n} = h^{n}\,, \tag{3.12}$$

where Δt is the time step, θ^n is the numerical approximation to $\theta(n\Delta t)$, and

$$g = -\left[\Lambda - 3\left(\eta+1\right)\theta_{s}^{2}\right]\,\theta_{ss} - \left(\eta+1\right)\Lambda_{s}\,\theta_{s} - \xi\,\sigma\,\tilde{\boldsymbol{u}}_{s}\cdot\hat{\boldsymbol{n}}\,, \tag{3.13}$$

$$h = -\eta^{-1}\theta_{s}^{4} + 3\theta_{ss}^{2} + \left(3+\eta^{-1}\right)\theta_{s}\,\theta_{sss} + \eta^{-1}\xi\,\sigma\,\tilde{\boldsymbol{u}}_{s}\cdot\hat{\boldsymbol{t}}\,. \tag{3.14}$$

Importantly, the high-order but linear term θ_{ssss} is treated implicitly, while the nonlinear but lower-order terms explicitly. The same approach was used for the nonlinear boundary conditions, Eq. (3.7), that becomes

$$\theta_{sss}(0)^{n+1} = \left(\theta_{s}(0)^{n}\right)^{3} - \theta_{s}(0)^{n}\Lambda(0)^{n} - \xi\,\sigma\,\tilde{\boldsymbol{u}}(0)^{n}\cdot\hat{\boldsymbol{n}}(0)^{n}\,. \tag{3.15}$$

The equations are uniformly discretized in space using second-order finite differences, centred and one-sided (cf. Sec. 2.1.3). With a sparse-matrix solver, the matrix equation for Λ^n on the spatial mesh in the arclength is solved first, followed by the one for θ^{n+1}. Importantly, at each time step, the background flow $\tilde{\boldsymbol{u}}^n$ is computed after integrating the tangent angle to obtain the filament configuration in Cartesian coordinates, through discretizing Eqs. (3.10), then calculating the Green's function, and finally taking the dot product with $\hat{\boldsymbol{t}}^n$. The SBDF implementation was compared to the backward Euler with Newton's method formulation for a no-fluid-entraining follower force showing a perfect agreement.

3.1.3 Linear stability analysis

Similarly to the analysis carried in Sec. 2.2, here we aim at using linear stability analysis to compute the critical value of the control parameter, σ, at which the filament becomes unstable and undergo self-sustained oscillations. By projecting Eq. (3.3) in the normal and tangent directions and after neglecting higher order terms, we obtain

$$\Lambda_x = \eta^{-1}\xi\sigma\tilde{u}\,, \tag{3.16}$$

and

$$y_t = -y_{xxxx} - \Lambda y_{xx} + \xi\sigma(\tilde{v} - \tilde{u}y_x)\,, \tag{3.17}$$

where $\tilde{u} = K_1 + K_2(x-1)^2$ and $\tilde{v} = K_1 y_x(1) + K_2(x-1)[y - y(1)]$ are the linearized components of the regularized nondimensional fluid flow $\tilde{\boldsymbol{u}}$, with

$$K_1 = \frac{(x-1)^2 + 2\varepsilon^2}{[(x-1)^2+\varepsilon^2]^{3/2}}\,,\quad K_2 = \frac{1}{[(x-1)^2+\varepsilon^2]^{3/2}}\,. \tag{3.18}$$

We note that far away from the point force ($|x-1| \gg \varepsilon$) the dominant flow component decays as that of a stokeslet, $\tilde{u} \sim 1/|x-1|$. Interestingly, the term $\Lambda_x y_x$ does not appear in Eq. (3.17) as the product $\hat{\boldsymbol{n}} \cdot \Lambda_x \boldsymbol{r}_x$ is identically zero. In other words, the fact that the tension varies along the filament length enters the equation only through Λ, but not its derivative.

We use again the dynamic criterion described in details in Sec. 2.2 to determine the value at which the filament buckles and becomes unstable. We compute the Lagrange multiplier first, requiring $\Lambda(1,t) = \sigma$, and then solve by finite differences the eigenvalue problem

$$-\hat{y}_{xxxx} - \Lambda\hat{y}_{xx} + \xi\sigma\{K_1\hat{y}_x(1) + K_2(x-1)[\hat{y} - \hat{y}(1)] - \hat{y}_x[K_1 + K_2(x-1)^2]\} = \omega\hat{y}\,, \tag{3.19}$$

Motors	Hydrodynamic case	Critical value
Single point force at the tip	no-fluid-entraining	$\sigma^* = 37.5$
	fluid-entraining with wall	$\sigma^* = 53.3$
	fluid-entraining with no wall	$\sigma^* = 67.7$

Table 3.1 Summary of the critical values of the control parameter for the onset of self-sustained oscillations for a filament subject to a single follower force at its tip.

with the boundary conditions $\hat{y}(0) = \hat{y}_x(0) = \hat{y}_{xx}(1) = \hat{y}_{xxx}(1) = 0$. Through the dynamics of the tip, the hydrodynamic point force changes position in time, and thus the resulting fluid flow is time-dependent. This is the origin of the terms containing $\hat{y}(1)$ and $\hat{y}_x(1)$ in (3.19). The numerical implementation of this eigenvalue problem is more challenging than in the absence of entrained flow and great care is needed, especially when discretising the boundary conditions and the local terms.

3.1.4 Results

The solution of the discretized equations of motion shows that, unsurprisingly, the filament dynamics has remained qualitatively unaltered compared to the no-fluid-entraining follower force of Chapter 2, as shown in Fig. 3.3a. Here again three dynamical regimes can be identified. The filament starts showing decaying oscillations at $\sigma \approx 32.4$ and becomes unstable undergoing a supercritical Hopf bifurcation at $\sigma^* \approx 67.7$ (Fig. 3.3b). The transition points between the different regimes are well captured by linear analysis which predicts the growth rate to become complex at $\sigma \approx 32.17$ (decaying oscillations) and to cross the imaginary axis at $\sigma^* \approx 67.92$ (Hopf bifurcation).

Why is the flow delaying the onset of self-sustained oscillations? The point force located at the tip of the filaments induces a fluid flow in the direction opposite to the compressive force, resulting in an added tension along the filament, and thus an effective compression which is lower than that of the no-fluid-entraining follower force case. Consequently, the transition from stable to unstable regime occurs at a larger value of σ.

Although the fluid-entraining follower better describes the real oocyte, an important aspect was neglected: the presence of the wall from a hydrodynamic perspective (Fig. 3.2). In fact, so far we had assumed that the filament was only attached at one end. But how would such a wall affect the critical value of the control parameter to give rise to self-sustained oscillations? For the sake of completeness, we have also computed σ^* for a filament subject to a fluid-entraining follower force in the presence of a hydrodynamic wall (Table 3.1), where we used the regularized Green's function proposed by Cortez et al. [104, 106] and chose the

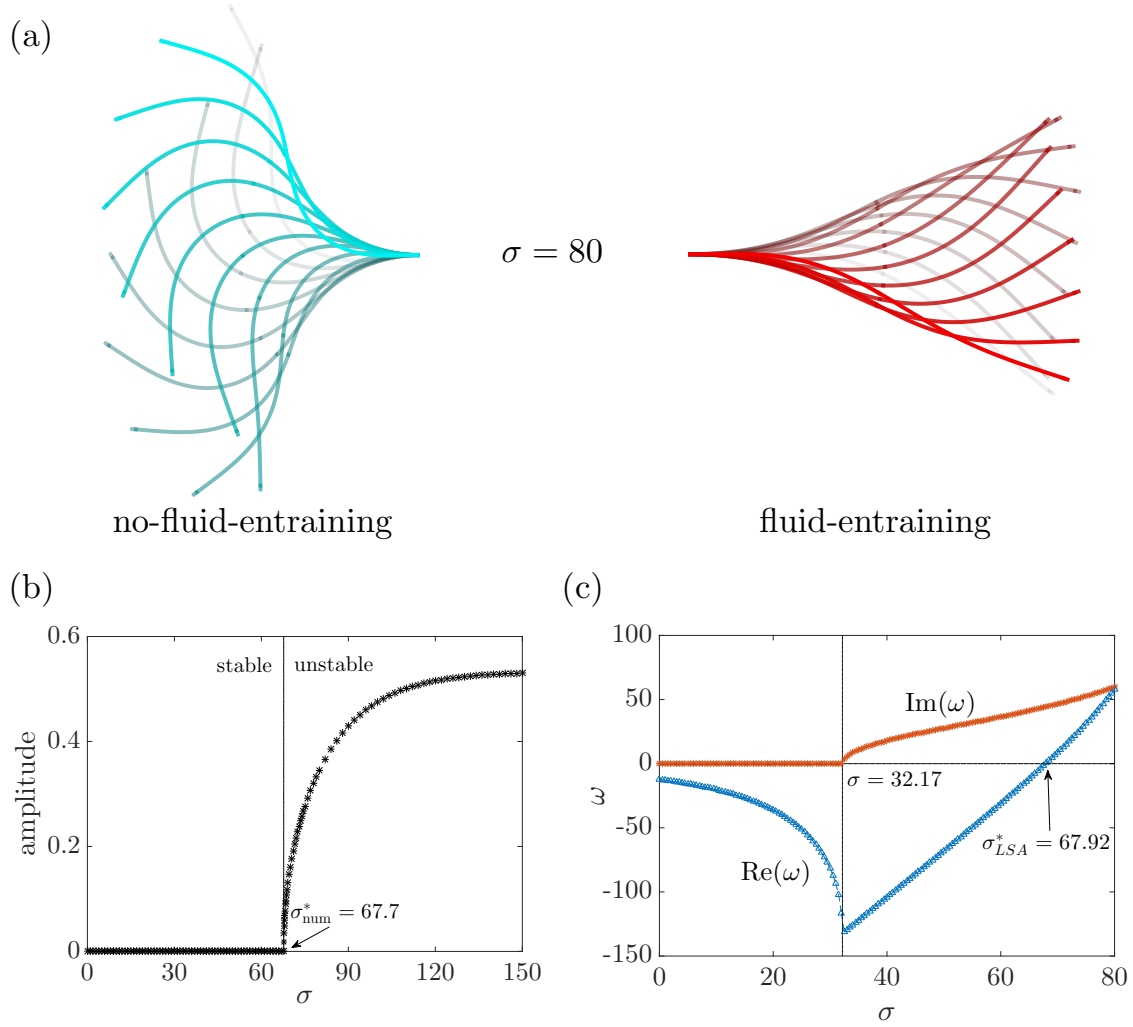

Fig. 3.3 (a) Time-lapse of filament flapping for the no-fluid-entraining follower force of Sec. 2.1.3 (blue) vs. the fluid-entraining follower force (red). The fluid flow reduces the tension on the filament, resulting in a delay of the instability and lower amplitude self-sustained oscillations. (b) The system undergoes a supercritical Hopf bifurcation at $\sigma^* \approx 67.7$. (c) Imaginary and real parts of the growth rate, ω, as function of σ. The growth rate becomes complex at $\sigma \approx 32.17$, thus giving rise to oscillations in the filament dynamics; its real part remains negative until $\sigma^* \approx 67.92$. For larger values of σ, the real part becomes positive, hence leading to instability.

regularization parameter ε in a similar fashion to a point force in an unbounded domain. We can notice that, as the velocity field decays faster compared to the stokeslet in free space, the tension exerted on the filament will be lower, thus requiring a smaller value of σ^* for the transition to occur.

3.1.5 Discussion

Having quantified the value for the onset of oscillations, it is important to relate it to the biological system which motivated its study, namely the *Drosophila* oocyte. Despite the model being an idealised version of the real system, in which many molecular motors move along the filament, a speculative comparison may still be made. The force exerted on the filaments by the molecular motors is known to be, as already discussed, on the order of piconewtons and MTs are approximately 20 μm in length. Despite the lack of information in the literature about the bending modulus of MTs in this specific context, we may estimate their rigidity from the direct measurements by Gittes et al. for a single MT *in vitro*, $A \approx 10^{-23}$ N m^2 [85]. With these numbers, we obtain that $\sigma \approx 120$, indicating that the forcing from molecular motors is large enough to lead to buckling and oscillations in the biological system. In addition, we may perform a first-order calculation to justify the assumption that the fluid-entraining follower force was stationary at the free end of the filament. Again, by considering the typical molecular motors speed, fractions of microns/sec, and the MTs length, we obtain that the time for the motor to walk along the filament is $t_{\text{walk}} \sim 2 \times 10^2$ s. For $\sigma \approx 120$, the beat frequency is ≈ 110, which corresponds to a nondimensional time of $\sim 4 \times 10^{-3}$. After rescaling for the relaxation time $\zeta_\perp L^4/A$, we find that the numerical dimensional time for the filament to undergo a half-cycle is comparable to t_{walk}. However, we should notice that: (i) the time coming from the numerical simulations is proportional to the viscosity (via $\zeta_\perp$), so if the viscosity was just one order of magnitude lower, we could separate the timescales; (ii) as stated in Sec. 1.3.4, motors undergo stochastic binding and unbinding event, so it is unlikely that the same motor would walk along the whole filament without unbinding; (iii) we also performed simulations where the fluid-entraining follower force could move along the filament, using the mathematical framework and numerical implementation presented in the next section, and the resulting qualitative dynamics was just unaltered.

3.2 Point force located anywhere along the filament

In a real *Drosophila* oocyte, the situation where the molecular motor is located elsewhere rather than at the filament tip, say $\boldsymbol{r}(s_0)$, is more likely to occur (Fig. 3.4a). To model this more realistic case, we should firstly notice that in the current framework, the action of the point force on the filament was described imposing the balance between the force at the tip and the external force. An equivalent representation consists in including the external force in the governing equations and imposing torque- and force-free boundary conditions at the

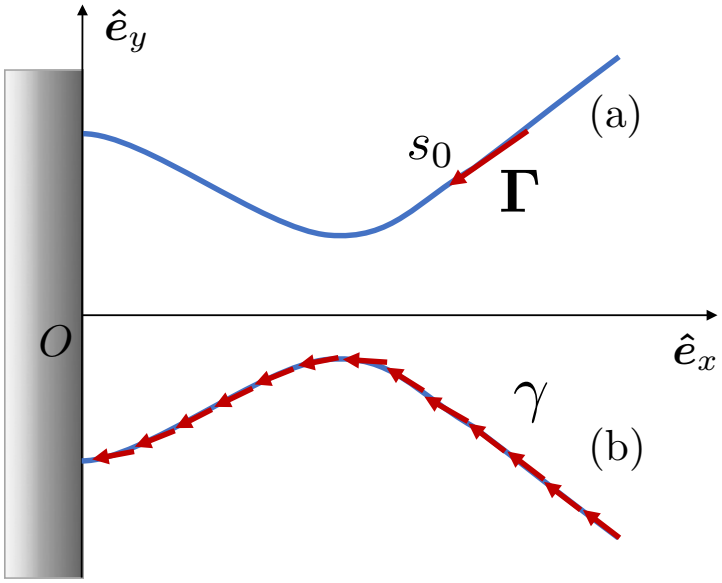

Fig. 3.4 (a) Filament subject to a follower force at $\boldsymbol{r}(s_0)$. (b) Line distribution of follower forces with force per unit length γ acting on the filament.

tip. In fact, Eq. (3.4) with boundary conditions

$$\boldsymbol{r}(0,t) = \boldsymbol{0}, \qquad \text{and} \qquad \boldsymbol{r}_s(0,t) = \hat{\boldsymbol{e}}_x, \tag{3.20a}$$

$$\boldsymbol{r}_{ss}(1,t) = \boldsymbol{0}, \qquad \text{and} \qquad -\boldsymbol{r}_{sss}(1,t) - \Lambda(1,t)\,\boldsymbol{r}_s(1,t) = -\sigma\,\boldsymbol{r}_s(1,t), \tag{3.20b}$$

is equivalent to

$$\boldsymbol{r}_t = \left(\kappa_{ss} - \kappa^3 + \kappa\Lambda\right)\hat{\boldsymbol{n}} + \eta\left[3\kappa\kappa_s - \Lambda_s - \sigma\,\delta(\boldsymbol{r} - \boldsymbol{r}_0)\right]\hat{\boldsymbol{t}} + \boldsymbol{u}, \tag{3.21}$$

with boundary conditions

$$\boldsymbol{r}(0,t) = \boldsymbol{0}, \qquad \text{and} \qquad \boldsymbol{r}_s(0,t) = \hat{\boldsymbol{e}}_x, \tag{3.22a}$$

$$\boldsymbol{r}_{ss}(1,t) = \boldsymbol{0}, \qquad \text{and} \qquad -\boldsymbol{r}_{sss}(1,t) - \Lambda(1,t)\,\boldsymbol{r}_s(1,t) = \boldsymbol{0}, \tag{3.22b}$$

where $\delta(\boldsymbol{r} - \boldsymbol{r}_0)$ is the Dirac delta function, and $\boldsymbol{r}_0 = \boldsymbol{r}(1)$ is the location of the point force, i.e. at the filament tip.

After differentiating with respect to the arclength and projecting the resulting equations in the normal and tangent directions, we obtain the following coupled nonlinear PDEs

$$\begin{aligned}\theta_t = &-\theta_{ssss} - \left[\Lambda - 3\,(\eta+1)\,\theta_s^2\right]\,\theta_{ss} \\ &- \left[(\eta+1)\,\Lambda_s + \eta\,\sigma\,\delta(s-s_0)\right]\,\theta_s - \boldsymbol{u}_s\cdot\hat{\boldsymbol{n}}\,, \qquad (3.23a)\\ \Lambda_{ss} - \eta^{-1}\theta_s^2\Lambda = &-\eta^{-1}\theta_s^4 + 3\theta_{ss}^2 + \left(3+\eta^{-1}\right)\theta_s\,\theta_{sss} \\ &- \sigma\,\delta_s(s-s_0) + \eta^{-1}\,\boldsymbol{u}_s\cdot\hat{\boldsymbol{t}}\,, \qquad (3.23b)\end{aligned}$$

where we have expressed the Dirac delta function in terms of the arclength. Similarly the boundary conditions for the filament configuration read

$$\theta(0,t) = 0\,, \qquad (3.24a)$$

$$\theta_{sss}(0,t) - \theta_s(0,t)^3 + \theta_s(0,t)\,\Lambda(0,t) + \boldsymbol{u}(0,t)\cdot\hat{\boldsymbol{n}}(0,t) = 0\,, \qquad (3.24b)$$

$$\theta_s(1,t) = 0\,, \qquad (3.24c)$$

$$\theta_{ss}(1,t) = 0\,, \qquad (3.24d)$$

and for the Lagrange multiplier

$$\Lambda_s(0,t) - 3\,\theta_s(0,t)\,\theta_{ss}(0,t) - \eta^{-1}\boldsymbol{u}(0,t)\cdot\hat{\boldsymbol{t}}(0,t) = 0\,, \qquad (3.25a)$$

$$\Lambda(1,t) = 0\,. \qquad (3.25b)$$

It is clear that the generality of such representation of the governing equations allows us to locate the point force anywhere along the filament ($\boldsymbol{r}_0 \in [\boldsymbol{r}(0),\boldsymbol{r}(1)]$). Despite this significant advantage, a major complication arises: Eqs. (3.23) include the delta function and its first derivative, which are singular at $s = s_0$. This fact leads to obvious difficulties when numerically solving the discretized PDEs, in particular 'how to deal with $\delta_s(s-s_0)$'?

Instead of treating the two singular terms explicitly, we split the domain into two subdomains: one from the base to slightly before the location of the point force, $s_{0_-} = s_0 - \varepsilon$, and one from slightly after, $s_{0_+} = s_0 + \varepsilon$, to the free end, namely $0 \le s \le s_{0_-}$ and $s_{0_+} \le s \le 1$. This yields to solving two separate sets of equations with no singular terms as these are cut off by construction. However, at this stage we only have six boundary conditions for the two fourth-order PDEs for θ and the two elliptic equations for Λ, which require twelve boundary conditions in total. The six missing conditions come from physical intuition as described below.

The point force exerts a tangential force on the filament. Hence, we expect the force in the normal direction to be continuous and the tension discontinuous across the singularity. In

particular, the jump in the Lagrange multiplier would be equal to the force applied. This can be easily seen when considering a straight filament. Eq. (3.23b) becomes $\Lambda_{ss} = -\sigma\,\delta_s(s-s_0)$, which can be trivially integrated from s_{0_-} to s_{0_+}, thus yielding to

$$[\![\Lambda]\!](s_0,t) = \Lambda(s_{0_+},t) - \Lambda(s_{0_-},t) = -\sigma\,, \tag{3.26}$$

where double-square brackets indicate the jump across s_0. In contrast, the force in the normal direction, which in dimensional form reads $[\![A\,\boldsymbol{r}_{sss}\cdot\hat{\boldsymbol{n}}]\!]$, must be continuous. Moreover, we notice that the point force does not affect neither the position and velocity nor the tangent and curvature of the filament across the singularity. Hence, we have $[\![\boldsymbol{r}_t]\!](s_0,t) = [\![\boldsymbol{r}]\!](s_0,t) = [\![\boldsymbol{r}_s]\!](s_0,t) = [\![\boldsymbol{r}_{ss}]\!](s_0,t) = \boldsymbol{0}$. When we express all these conditions in terms of the tangent angle, we obtain

$$[\![\theta]\!](s_0,t) = [\![\theta_s]\!](s_0,t) = [\![\theta_{ss}]\!](s_0,t) = 0\,. \tag{3.27}$$

The last two boundary conditions are obtained considering the jump between s_{0_-} and s_{0_+} of Eq. (3.21). After imposing continuity in both the background velocity field and the filament velocity and projecting the equations in $\hat{\boldsymbol{n}}$ and $\hat{\boldsymbol{t}}$, we obtain

$$[\![\theta_{sss}]\!](s_0,t) = -\sigma\,\theta_s(s_0,t) \quad \text{and} \quad [\![\Lambda_s]\!](s_0,t) = 0\,, \tag{3.28}$$

as the curvature is constant and the first spatial derivative of the Lagrange multiplier does not change across s_0 (the jump in the delta function is indeed zero).

To conclude, Eqs. (3.23) with Eqs. (3.24)-(3.25) solved in the region $0 \le s \le 1$ are equivalent to

$$\theta_t = -\theta_{ssss} - \left[\Lambda - 3\,(\eta+1)\,\theta_s^2\right]\,\theta_{ss} - (\eta+1)\,\Lambda_s\,\theta_s - \boldsymbol{u}_s\cdot\hat{\boldsymbol{n}}\,, \tag{3.29a}$$

$$\Lambda_{ss} - \eta^{-1}\theta_s^2\Lambda = -\eta^{-1}\theta_s^4 + 3\theta_{ss}^2 + \left(3+\eta^{-1}\right)\theta_s\,\theta_{sss} + \eta^{-1}\,\boldsymbol{u}_s\cdot\hat{\boldsymbol{t}}\,, \tag{3.29b}$$

solved in the two sub-domains and with boundary conditions Eqs. (3.24)-(3.28).

3.2.1 Numerical implementation of the jump conditions

To numerically solve Eqs. (3.29) and Eqs. (3.24)-(3.28), we firstly discretize them with second-order finite differences, and then use the IMEX method described in Sec. 3.1.2. The challenge lies in the implementation of the jump conditions.

We tackle this difficulty by the usage of fictitious nodes. We commence our analysis by considering the equation for the Lagrange multiplier, namely Eq. (3.29b). We define the node on the mesh grid where the point force is located s_{0_i}, the adjacent fictitious (or ghost)

nodes slightly before and after $s_{0_{g-}}$ and $s_{0_{g+}}$, respectively, and the corresponding Lagrange multiplier Λ_i, Λ_{g-} and Λ_{g+}. Solving the discretized equations in the two separate domains and then trying to converge to the solution that satisfies the jump conditions could be a complex task. Instead, we directly solve the linear system in the whole domain. To do so, we firstly Taylor expand the discretized Lagrange multiplier around the fictitious points

$$\Lambda_{i-2} \approx \Lambda_{g-} - 2\Delta s \frac{\partial \Lambda_{g-}}{\partial s} + 2\Delta s^2 \frac{\partial^2 \Lambda_{g-}}{\partial s^2}, \tag{3.30}$$

$$\Lambda_{i-1} \approx \Lambda_{g-} - \Delta s \frac{\partial \Lambda_{g-}}{\partial s} + \frac{\Delta s^2}{2} \frac{\partial^2 \Lambda_{g-}}{\partial s^2}, \tag{3.31}$$

$$\Lambda_{i+1} \approx \Lambda_{g+} + \Delta s \frac{\partial \Lambda_{g+}}{\partial s} + \frac{\Delta s^2}{2} \frac{\partial^2 \Lambda_{g+}}{\partial s^2}, \tag{3.32}$$

$$\Lambda_{i+2} \approx \Lambda_{g+} + 2\Delta s \frac{\partial \Lambda_{g+}}{\partial s} + 2\Delta s^2 \frac{\partial^2 \Lambda_{g+}}{\partial s^2}. \tag{3.33}$$

Then we discretize the jump conditions, that become

$$\Lambda_{g+} - \Lambda_{g-} = -\Gamma, \tag{3.34}$$

$$\frac{\partial \Lambda_{g+}}{\partial s} - \frac{\partial \Lambda_{g-}}{\partial s} = 0. \tag{3.35}$$

This yields to a system of six equations in six unknowns that can be easily solved, thus returning the expressions for the Lagrange multiplier at the fictitious nodes, which read

$$\Lambda_{g-} = -\frac{1}{6}\Lambda_{i-2} + \frac{2}{3}\Lambda_{i-1} + \frac{2}{3}\Lambda_{i+1} - \frac{1}{6}\Lambda_{i+2} + \frac{\Gamma}{2\Delta s^2}, \tag{3.36}$$

$$\Lambda_{g+} = -\frac{1}{6}\Lambda_{i-2} + \frac{2}{3}\Lambda_{i-1} + \frac{2}{3}\Lambda_{i+1} - \frac{1}{6}\Lambda_{i+2} - \frac{\Gamma}{2\Delta s^2}. \tag{3.37}$$

Such expressions will then be substituted into the original discretized equations and the resulting linear system for the Lagrange multiplier solved.

Similarly, the discretized equation for the filament configuration with the corresponding jump condition can be derived. Equations only involving the delta function and not its derivative are fairly common in physics and their numerical treatment can be found in the literature (e.g. [110]). Hence, there is no need to solve the equation for θ using fictitious nodes. Both implementations were validated against analytical results, such as the case of a straight filament with a point force at s_0 and the 1D diffusion and hyperdiffusion problems with a Dirac delta force in the domain.

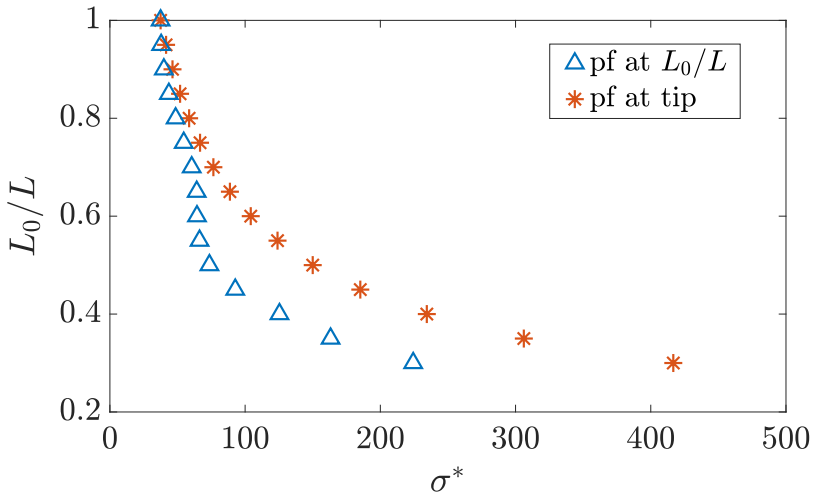

Fig. 3.5 Numerical comparison of how σ^* varies with L_0/L. The onset of the self-sustained oscillations arises earlier for the filament with the point force located somewhere other than at the tip (blue triangles) compared to a shorter filament with a concentrated load at its tip (red stars) as the unloaded part of the filament experiences an extra force that compresses it further.

3.2.2 Results

The governing equations were numerically solved using the SBDF scheme mentioned earlier. Despite the complexity associated with solving the equations for a follower force located somewhere other than at the tip of the filament, the resulting qualitative dynamics is unchanged as the now familiar three different dynamical regimes can be observed. But how does the location of the point force affect the critical value of the control parameter? Fig. 3.5 shows the numerical results of how σ^* varies when positioning the point force closer to the clamped end (blue triangles) compared to a filament with the concentrated force at its tip but length L_0/L (red stars). For the latter, the numerical results are consistent with the theoretical value $\sigma^*_{L_0}$ that can be derived from σ^*. In fact, as the critical load is $\Gamma^* = \sigma^* A/L^2$, we have that $\Gamma^*_{L_0} = \sigma^* A/L_0^2$, which leads to $\Gamma^*_{L_0} = \Gamma^*(L/L_0)^2$, or, alternatively, $\sigma^*_{L_0} = \sigma^*(L/L_0)^2$. It might be mistakenly thought that the two curves should overlap as, for each point in the graph, the distance of the point force from the wall is the same. However, it should be noticed that the filament with the point force not seated at its tip experiences an extra force since the remaining part, with length $1 - L_0/L$, is dragged in the fluid and is subject to both the viscous and elastic forces. Such a force augments the total compressive force thus leading to an earlier transition to the unstable regime, i.e. smaller values of σ^*.

3.3 Line distribution of follower forces

Typically, many motors simultaneously walk along the same MT. To capture this instance, we consider the case of a line distribution of follower forces located along the filament (Fig. 3.4b). The time evolution of the filament configuration then reads

$$\boldsymbol{r}_t = \frac{1}{\zeta_\perp}\left[A\left(\kappa_{ss} - \kappa^3\right) + \kappa\Lambda\right]\hat{\boldsymbol{n}} + \frac{1}{\zeta_\parallel}\left(3A\kappa\kappa_s - \Lambda_s - \gamma\right)\hat{\boldsymbol{t}}\,, \tag{3.38}$$

where γ is the *constant* force per unit length exerted by the point forces on the filament, obviously acting tangentially. After rescaling lengths by L, time by the relaxation time $\zeta_\perp L^4/A$, and the Lagrange multiplier by the elastic force A/L^2, Eq. (3.38) expressed in dimensionless units becomes

$$\boldsymbol{r}_t = \left(\kappa_{ss} - \kappa^3 + \kappa\Lambda\right)\hat{\boldsymbol{n}} + \eta\left(3\kappa\kappa_s - \Lambda_s - \Sigma\right)\hat{\boldsymbol{t}}\,, \tag{3.39}$$

with Σ being the control parameter defined as

$$\Sigma \equiv \frac{\gamma L^3}{A}\,. \tag{3.40}$$

For a line distribution of fluid-entraining follower forces, we must add to the previous equations the total fluid flow generated, namely $\boldsymbol{u} = 1/(8\pi\mu)\int_0^L \boldsymbol{G}\cdot\gamma\hat{\boldsymbol{t}}\,\mathrm{d}s$. Such an integral can be discretized using N_{elem} equal elements with length $\Delta l = L/N_{\mathrm{elem}}$, each with a point force in the middle at s_{0_k}, strength $\gamma\Delta l$, and direction $\hat{\boldsymbol{t}}^k \equiv \hat{\boldsymbol{t}}(s_{O_k})$. Hence, by exploiting the linearity of Stokes equations, we can calculate the total velocity field by linear superposition of the fluid flows created by a finite number of point forces. The background flow then becomes

$$\boldsymbol{u} = \frac{1}{8\pi\mu}\int_0^L \boldsymbol{G}\cdot\gamma\hat{\boldsymbol{t}}\,\mathrm{d}s \approxeq \frac{\gamma\Delta l}{8\pi\mu}\sum_{k=1}^{N_{\mathrm{elem}}}\boldsymbol{G}^k\cdot\hat{\boldsymbol{t}}^k\,, \tag{3.41}$$

where $\boldsymbol{G}^k \equiv \boldsymbol{G}(s;s_{O_k})$. This approach proves to be particularly attractive in this context as the flows for the geometries considered can be computed analytically, thus reducing the computational complexities associated with solving Stokes equations numerically. Again, we must regularize the Green's function, which will be denoted $\tilde{\boldsymbol{G}}$. In dimensionless units this yields to

$$\boldsymbol{u} \approxeq \xi\,\Sigma\Delta\tilde{l}\sum_{k=1}^{N_{\mathrm{elem}}}\tilde{\boldsymbol{G}}^k\cdot\hat{\boldsymbol{t}}^k \equiv \xi\,\Sigma\Delta\tilde{l}\,\tilde{\boldsymbol{u}}\,, \tag{3.42}$$

where $\Delta\tilde{l} = 1/N_{\text{elem}}$ and $\tilde{\boldsymbol{u}}$ is the total regularised flow. To conclude, the governing equations for a line distributions of follower forces read

$$\theta_t = -\theta_{ssss} - \left[\Lambda - 3\,(\eta+1)\,\theta_s^2\right]\,\theta_{ss} - \left[(\eta+1)\,\Lambda_s + \eta\Sigma\right]\,\theta_s - \xi\,\Sigma\Delta\tilde{l}\,\tilde{\boldsymbol{u}}_s\cdot\hat{\boldsymbol{n}}\,, \tag{3.43a}$$

$$\Lambda_{ss} - \eta^{-1}\theta_s^2\Lambda = -\eta^{-1}\theta_s^4 + 3\theta_{ss}^2 + \left(3+\eta^{-1}\right)\theta_s\,\theta_{sss} + \eta^{-1}\,\xi\,\Sigma\Delta\tilde{l}\,\tilde{\boldsymbol{u}}_s\cdot\hat{\boldsymbol{t}}\,. \tag{3.43b}$$

Notice that in the equation for the Lagrange multiplier there is no term explicitly associated with the follower forces; this is because γ is constant, and the term Σ_s that would appear is identically zero.

The boundary conditions for a clamped free filament with a line distribution of forces read

$$\theta(0,t) = 0\,, \tag{3.44}$$

$$\theta_{sss}(0,t) - \theta_s(0,t)^3 + \theta_s(0,t)\,\Lambda(0,t) + \xi\,\Sigma\Delta\tilde{l}\,\tilde{\boldsymbol{u}}(0,t)\cdot\hat{\boldsymbol{n}}(0,t) = 0\,, \tag{3.45}$$

$$\theta_s(1,t) = 0\,, \tag{3.46}$$

$$\theta_{ss}(1,t) = 0\,, \tag{3.47}$$

for the filament configuration, and

$$\Lambda_s(0,t) - 3\,\theta_s(0,t)\,\theta_{ss}(0,t) - \eta^{-1}\xi\,\Sigma\Delta\tilde{l}\,\tilde{\boldsymbol{u}}(0,t)\cdot\hat{\boldsymbol{t}}(0,t) + \Sigma = 0\,, \tag{3.48}$$

$$\Lambda(1,t) = 0\,, \tag{3.49}$$

for the Lagrange multiplier. To better understand these conditions we can create an analogy with a chain that is held from one end under the only effect of gravity. At its free end, the tension is zero as no force is applied, while at the pinned end, the tension reaches its maximum value as it experiences the weight of all the links in the chain. Similarly, in a straight filament with a line distribution of no-fluid-entraining follower forces the tension linearly increases from zero, at the free end, to Σ, or, equivalently, the Lagrange multiplier linearly decreases from zero to $-\Sigma$.

3.3.1 Results

The same numerical scheme discussed previously in this Chapter was used to numerically solve Eqs. (3.43) with the associated boundary conditions. The number of elements N_{elem} to discretize the integral for the background flow was chosen to ensure that the relative error was below 2% compared to the case of setting N_{elem} equal to the number of grid points.

Motors	Hydrodynamic case	Critical value
Line distribution of point forces	no-fluid-entraining	$\Sigma^* = 74.3$
	fluid-entraining with wall	$\Sigma^* = 124.2$
	fluid-entraining with no wall	$\Sigma^* = 261.1$

Table 3.2 Summary of the critical values of the control parameter for the onset of self-sustained oscillations for a filament subject to a line distribution of follower forces.

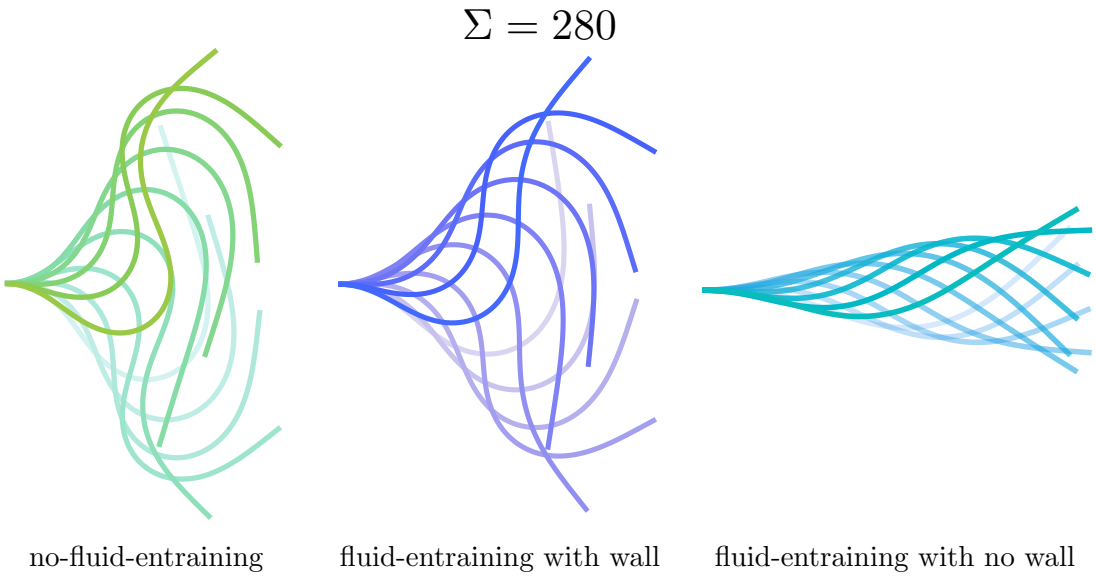

Fig. 3.6 Comparison of the time-lapse of the self-sustained oscillations for a filament subject to a line distribution of point forces for $\Sigma = 280$. The filament with no-fluid-entraining follower forces has the largest amplitudes, while the one with fluid-entraining follower forces in absence of a hydrodynamic wall has the smallest. This is caused by the fluid flow created by the point forces which diminishes the tension on the filament, thus delaying the onset of the instability.

Again, the filament shows three regimes depending on Σ: it returns to its original straight shape, shows oscillations that then die out, undergoes self-sustained oscillations. Table 3.2 summarises the critical value Σ^* at which the filament becomes unstable for the no-fluid-entraining follower forces and the fluid-entraining follower forces both in the presence and absence of a hydrodynamic wall. Similar conclusions can be drawn about the magnitude of these values by considering how the tension varies for the instances considered. If we then compare the filament dynamics for the three cases when $\Sigma = 280$, we see that, as expected, when no hydrodynamic wall is present the oscillations are the narrowest as the value of

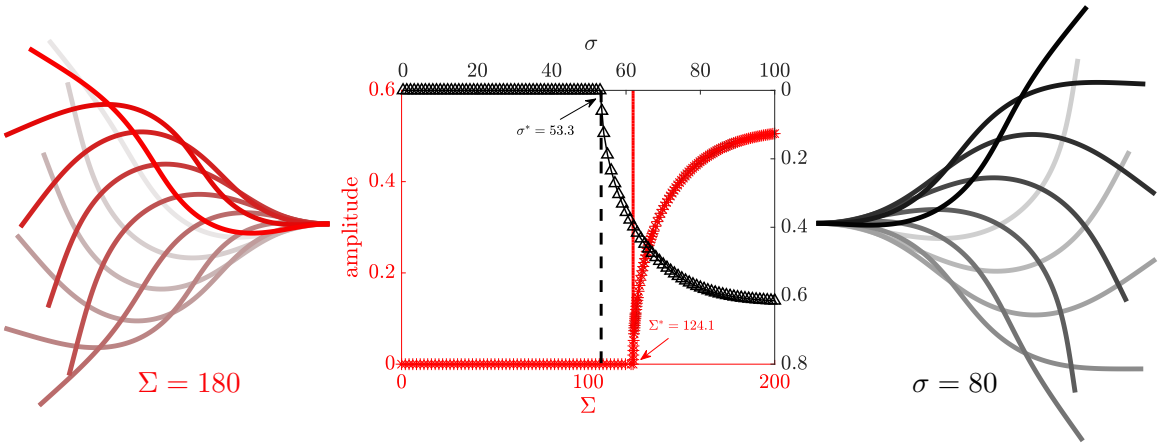

Fig. 3.7 Comparison of Hopf bifurcations for a filament with a line distribution of fluid-entraining follower force in the presence of a hydrodynamic wall (red) and with only one of such a point force at the tip (black). Left and right plots are the corresponding time-lapses of the flapping motion for values of the control parameter $\approx 80\%$ of the critical one. The amplitude of the oscillations is larger when a single point force acts on the filament compared to a line.

the control parameter is the closest to its Σ^* (Fig. 3.6). The amplitude of the oscillations increases for the fluid-entraining case with the wall as the flows decay faster, thus reducing the tension along the filament and anticipating the transition, and becomes the widest when the filament is subject to no-fluid entraining follower forces (smaller Σ^*). Fig. 3.7 compares the Hopf bifurcations for a filament with a line distribution and a single fluid-entraining follower forces in presence of a wall. The amplitude for the case of a single point force at the tip is larger when the filament is acted on by a single point force (see also left and right plots in which the time-lapses of the filament dynamics are shown for values of the control parameter $\approx 80\%$ of the critical one).

3.4 Conclusions

In this chapter we have extended the framework developed in Chapter 2 in order to more accurately describe the real *Drosophila* oocyte. In particular, we have considered the case where the point force not only exerts a force on the filament, but also generates a fluid flow, scenario that typically occurs when motors translocate along MTs and the cargo pushes the surrounding fluid. We computed the control parameter using the data of the real oocyte and showed that it is beyond the critical value found by our numerical experiments. This suggests that the waving motion observed at stage 9 might be explained by our model. Then, we

considered the cases where the motor was located anywhere along the filament and presented a framework to numerically implement the jump condition. Finally, we studied the dynamics of a filament subject to a line distribution of follower forces and showed that the resulting dynamics is qualitatively unaltered.

Chapter 4

The collective dynamics of an array of filaments

After studying the dynamics of a filament compressed by follower forces that can entrain fluid flow and be located anywhere along the filament, we extend the framework to the multi-filament case in order to study the collective buckling. Apart from the specific case of *Drosophila* oocytes, in nature it is fairly rare to find a single filament, so studying the collective behaviour might be of interest and applicable to other biological systems as well. The main difficulty in tackling such a problem stands in the numerics. When the n filaments hydrodynamically interact, they mutually affect each other, thus resulting in a typical n-body problem, which requires order n^2 computations at each time step. In Sec. 4.1, we formulate the multi-filament problem and, in Sec. 4.2, explain the numerical implementation adopted to minimize the computational time. We then study the dynamics of two elastic filaments subject to a single and a line distribution of fluid-entraining follower forces and show that the hydrodynamic interactions can lead to synchronization of the beating motion in Sec. 4.3.1. Sec. 4.3.2 presents the results for more than two filaments. We show that a multitude of such filaments can synchronize their motion and that the filament density is crucial in determining the system dynamics as a symmetry-breaking mechanism can also arise.

4.1 Equations of motion

We initially consider two parallel slender elastic filaments with length L and radius b ($L \gg b$) and no intrinsic curvature. They are attached to a wall and moving in a 2D-plane surrounded by a fluid with viscosity μ. The distance at $s = 0$ between the filaments is d and each of them is subject to a single follower force at the tip, $\mathbf{\Gamma}$, while the other end is clamped (Fig. 4.1).

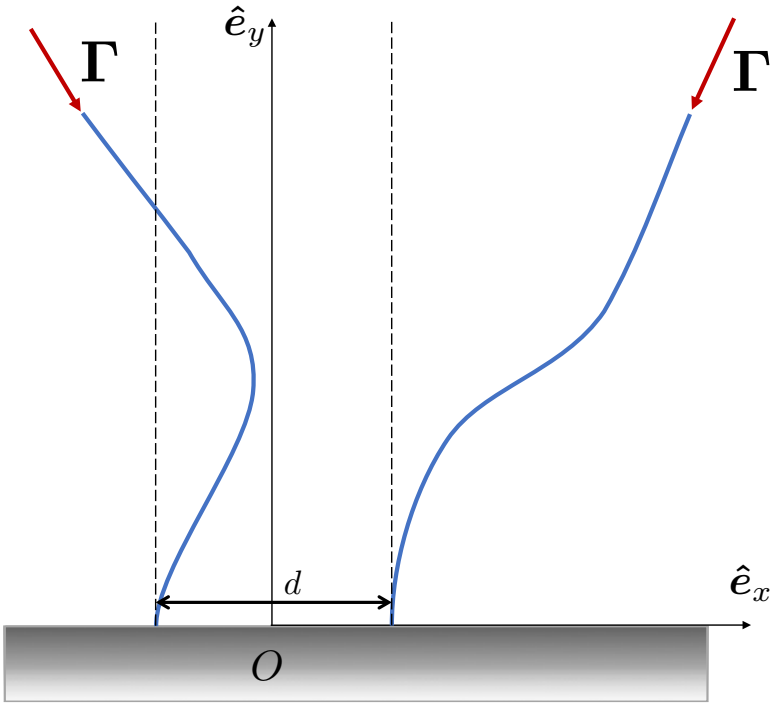

Fig. 4.1 Two filaments acted on by two fluid-entraining follower forces at their tips that hydrodynamically interact. The mean distance between them is denoted by d.

We denote by $\boldsymbol{r}(s,t)$ the filament configuration parametrized by its arclength $0 \leq s \leq L$. At low Reynolds number inertia is negligible, thus the total force on the filament must sum to zero. By exploiting the RFT framework to capture the viscous drag, thus neglecting nonlocal effects, and the classic Euler-Bernoulli theory for an elastic inextensible filament, the governing equations for a single filament, derived in detail in the previous chapters, read

$$\left(\zeta_{\parallel}\hat{\boldsymbol{t}}\hat{\boldsymbol{t}} + \zeta_{\perp}\hat{\boldsymbol{n}}\hat{\boldsymbol{n}}\right)\cdot(\boldsymbol{r}_t - \boldsymbol{u}) + A\boldsymbol{r}_{ssss} + (\Lambda \boldsymbol{r}_s)_s = \boldsymbol{0}, \tag{4.1}$$

where subscripts denote differentiation, $\zeta_{\parallel}, \zeta_{\perp}$ are the drag coefficients, $\hat{\boldsymbol{t}}$ and $\hat{\boldsymbol{n}}$ the tangent and normal unit vectors, A the bending modulus, and Λ the Lagrangian multiplier used to impose inextensibility. The background flow $\boldsymbol{u}$ is the velocity field on the filament centreline produced by a fluid-entraining follower force located at the filament tip ($s = L$).

When two filaments subject to fluid-entraining follower forces are next to each other, they hydrodynamically interact. Such an interaction comes from three contributions: (i) the fluid flow produced by the point force located on the filament considered, $\boldsymbol{u}^{(j)}$, (ii) the fluid flow created by the point force on the other filament, $\boldsymbol{u}^{(i)\to(j)}$, (iii) the presence of the other filament that will then induce a fluid flow, $\boldsymbol{v}^{(i)\to(j)}$. Take two filaments with no point forces

acting on them, one bent (i) and one straight (j). The contribution $\boldsymbol{v}^{(i)\to(j)}$ accounts for the hydrodynamic interaction: the bent filament (i) will straighten up thus inducing a flow that will affect filament j, which will in turn affect the first one. They will slightly oscillate until returning to a straight configuration.

The governing equations for the filament j interacting with the filament i can therefore be described by

$$\left(\zeta_{\parallel}\hat{\boldsymbol{t}}^{(j)}\hat{\boldsymbol{t}}^{(j)}+\zeta_{\perp}\hat{\boldsymbol{n}}^{(j)}\hat{\boldsymbol{n}}^{(j)}\right)\cdot\left(\boldsymbol{r}_t^{(j)}-\boldsymbol{U}^{(j)}\right)=-A\boldsymbol{r}_{ssss}^{(j)}-\left(\Lambda^{(j)}\boldsymbol{r}_s^{(j)}\right)_s, \tag{4.2}$$

where the total background flow is given by

$$\boldsymbol{U}^{(j)}=\boldsymbol{u}^{(j)}+\boldsymbol{u}^{(i)\to(j)}+\boldsymbol{v}^{(i)\to(j)}, \tag{4.3}$$

with

$$\boldsymbol{u}^{(j)}(s,t)=\frac{1}{8\pi\mu}\boldsymbol{G}(\boldsymbol{r}^{(j)}-\boldsymbol{r}_0^{(j)})\cdot\Gamma\hat{\boldsymbol{t}}(\boldsymbol{r}_0^{(j)}), \tag{4.4}$$

$$\boldsymbol{u}^{(i)\to(j)}(s,t)=\frac{1}{8\pi\mu}\boldsymbol{G}(\boldsymbol{r}^{(j)}-\boldsymbol{r}_0^{(i)})\cdot\Gamma\hat{\boldsymbol{t}}(\boldsymbol{r}_0^{(i)}), \tag{4.5}$$

$$\boldsymbol{v}^{(i)\to(j)}(s,t)=\frac{1}{8\pi\mu}\int_0^L\boldsymbol{G}(\boldsymbol{r}^{(j)}-\boldsymbol{r}^{(i)})\cdot\boldsymbol{f}(\boldsymbol{r}^{(i)})\,\mathrm{d}s, \tag{4.6}$$

in which $\boldsymbol{G}$ is the Green's tensor, $\boldsymbol{r}_0^{(j)}$ the location of the fluid-entraining follower force on the filament j, and $\boldsymbol{f}(\boldsymbol{r}^{(i)})$ the total force per unit length acting on filament i, i.e. $\boldsymbol{f}(\boldsymbol{r}^{(i)})=-A\boldsymbol{r}_{ssss}^{(i)}-(\Lambda^{(i)}\boldsymbol{r}_s^{(i)})_s$.

In this model we neglect higher order contributions. In fact, when calculating the flow induced by the movement of the other filament, $\boldsymbol{v}^{(i)\to(j)}$, we only consider the flow produced by the stokeslets, but not the one from the doublets [56]. Moreover, by using the local RFT framework, we neglect that the filament can interact with itself. Slender-body theory provides the necessary mathematical framework to include self-interactions. This would entail a more complex formulation involving integral equations that present singularities which would need to be regularized. For the sake of simplicity, we neglect nonlocal effects. However, we include the presence of the other filaments $\boldsymbol{v}^{(i)\to(j)}$ since, as discussed already, without the fluid flows set by the fluid-entraining follower forces, $\boldsymbol{u}^{(i)\to(j)}$, filaments would not be able to hydrodynamically interact as opposed to the single filament case where hydrodynamic forces would still be experienced instead via RFT.

After rescaling the lengths by the filament length L, the time by the relaxation time $\zeta_{\perp}L^4/A$, and the Lagrange multiplier by the elastic force A/L^2, the governing equations in

dimensionless form read

$$\left(\eta^{-1}\hat{\boldsymbol{t}}^{(j)}\hat{\boldsymbol{t}}^{(j)}+\hat{\boldsymbol{n}}^{(j)}\hat{\boldsymbol{n}}^{(j)}\right)\cdot\left(\boldsymbol{r}_t^{(j)}-\boldsymbol{U}^{(j)}\right)=-\boldsymbol{r}_{ssss}^{(j)}-\left(\Lambda^{(j)}\boldsymbol{r}_s^{(j)}\right)_s, \tag{4.7}$$

and the total background flow becomes

$$\begin{aligned}\boldsymbol{U}^{(j)}=\xi\Big\{\sigma\left[\boldsymbol{G}(\boldsymbol{r}^{(j)}-\boldsymbol{r}_0^{(j)})\cdot\hat{\boldsymbol{t}}(\boldsymbol{r}_0^{(j)})+\boldsymbol{G}(\boldsymbol{r}^{(j)}-\boldsymbol{r}_0^{(i)})\cdot\hat{\boldsymbol{t}}(\boldsymbol{r}_0^{(i)})\right]\\+\int_0^1\boldsymbol{G}(\boldsymbol{r}^{(j)}-\boldsymbol{r}^{(i)})\cdot\boldsymbol{f}(\boldsymbol{r}^{(i)})\,\mathrm{d}s\Big\},\end{aligned} \tag{4.8}$$

with $\eta=\zeta_\perp/\zeta_\parallel$, $\xi=\zeta_\perp/8\pi\mu$, and $\sigma=\Gamma L^2/A$. Since the first term in Eq. (4.8) is singular at $\boldsymbol{r}^{(j)}=\boldsymbol{r}_0^{(j)}$, we use the regularized stokeslet proposed by Cortez et al. [104] instead, denoted $\tilde{\boldsymbol{G}}$ throughout. The regularization parameter is chosen such that the velocity of the molecular motor equals the velocity of the fluid flow at the location of the point force as described in Chapter 3.

4.1.1 The multi-filament case

If we have more than two filaments, say N_{fil}, each of them with N_{pf} fluid-entraining follower forces located at $\boldsymbol{r}_{0,k}$, where $k=1,\ldots,N_{\mathrm{pf}}$, the total background flow will include the velocity fields produced by all point forces as well as the fluid flow induced by the presence of all the filaments. This translates into the following expression for the total nondimensional background flow on filament j

$$\begin{aligned}\boldsymbol{U}^{(j)}=\xi\Bigg\{\sigma\left[\sum_{k=1}^{N_{\mathrm{pf}}}\tilde{\boldsymbol{G}}(\boldsymbol{r}^{(j)}-\boldsymbol{r}_{0,k}^{(j)})\cdot\hat{\boldsymbol{t}}(\boldsymbol{r}_{0,k}^{(j)})+\sum_{\substack{i=1\\i\neq j}}^{N_{\mathrm{fil}}}\sum_{k=1}^{N_{\mathrm{pf}}}\boldsymbol{G}(\boldsymbol{r}^{(j)}-\boldsymbol{r}_{0,k}^{(i)})\cdot\hat{\boldsymbol{t}}(\boldsymbol{r}_{0,k}^{(i)})\right]\\+\sum_{\substack{i=1\\i\neq j}}^{N_{\mathrm{fil}}}\int_0^1\boldsymbol{G}(\boldsymbol{r}^{(j)}-\boldsymbol{r}^{(i)})\cdot\boldsymbol{f}(\boldsymbol{r}^{(i)})\,\mathrm{d}s\Bigg\}.\end{aligned} \tag{4.9}$$

Similarly, for a line distribution of fluid-entraining follower forces with force per unit length γ, if we discretized it with N_{pf} as shown in Sec. 3.3, we would obtain the same expression except for replacing σ with $\Sigma\Delta\tilde{l}$, where $\Sigma=\gamma L^3/A$ and $\Delta\tilde{l}=1/N_{\mathrm{elem}}$.

4.1.2 Fluid flow considerations

Compared to the individual dynamics, the multi-filament problem is intrinsically linked to the significant computational cost to simulate the equations of motion. In fact, each filament

affects the dynamics of all the others and vice versa. If we consider the case $N_{\text{pf}} = 1$, we see that the bottleneck is the term $\boldsymbol{v}^{(i)\to(j)}$ in the total background flow. For every filament, the integral in Eq. (4.9) needs to be numerically computed $(N_{\text{fil}} - 1)$ times, thus resulting in approximately N_{fil}^2 computations at each time step. In other words, the computational cost grows quadratically with the number of filaments.

Before tackling this complexity, we investigate whether this contribution, i.e. the presence of the other filaments, might be neglected at all. For this aim, we considered the case $N_{\text{fil}} = 2$ and performed an asymptotic analysis for two extreme cases: the dilute and close-by limits. Such an analysis showed that the velocity field produced by the point forces on the other filaments is of the same order as the one associated with the movement of the filaments themselves, i.e. $|\boldsymbol{u}^{(i)\to(j)}| \sim |\boldsymbol{v}^{(i)\to(j)}|$. Thus the total background flow must include all the terms in (4.3), and the computational difficulty remains and must be handled.

There might still be a question about the total force $\boldsymbol{f}(\boldsymbol{r}^{(i)})$ appearing in Eq. (4.6). Specifically, what is this 'total' force? Shall we include the compressive follower force in addition to the elastic force and tension so that $\boldsymbol{f}(\boldsymbol{r}^{(i)}) = -\boldsymbol{r}^{(i)}_{ssss} - (\Lambda^{(i)}\boldsymbol{r}^{(i)}_s)_s - \sigma\,\delta(s-s_0)\boldsymbol{r}^{(i)}_s$? When the point force is at the tip, as its contribution does not appear in the equations of motion but only in the boundary conditions, we have that, in dimensionless units, $\boldsymbol{f}(\boldsymbol{r}^{(i)}) = -\boldsymbol{r}^{(i)}_{ssss} - (\Lambda^{(i)}\boldsymbol{r}^{(i)}_s)_s$. The question then turns to what happens when the point force is somewhere else or it is replaced by a line distribution of point forces. In Sec. 3.2 we showed the equivalence of including the point force in the equations of motion through a Delta function compared to having it in the boundary conditions. Here, we use this result to numerically investigate three cases for two parallel filaments with the same initial perturbed configuration subject to no-fluid-entraining follower forces so that the total background flow is simply given by Eq. (4.6), as $\boldsymbol{u}^{(j)} = \boldsymbol{u}^{(i)\to(j)} = \boldsymbol{0}$. Specifically, we consider the cases when (i) the follower force enters through the boundary conditions, (ii, iii) it appears in the equations of motion and the Delta function term is omitted or present in the definition of $\boldsymbol{f}(\boldsymbol{r}^{(i)})$, respectively. By quantitatively comparing the resulting dynamics and timescales, we infer that the compressive force should not be included in the total force. By doing so we would double-count its contribution thus enhancing the hydrodynamic interactions and triggering the onset of the dynamical behaviours observed in Sec. 4.3 earlier.

4.2 Numerical implementation

As previously mentioned, the computational cost to numerically simulate the multi-filament problem is significant. n-body problems have been widely studied and several techniques have been proposed to reduce the overall cost and speed up the algorithms. Among them,

Fast Multiple Method (FMM) stands out for reducing the amount of work to compute the pairwise interactions from order n^2 to order n [111]. This made such an algorithm attractive in large-scale problems encountered in fluid dynamics, molecular dynamics, and celestial mechanics. The underlying idea, initially proposed for electromagnetic problems, is to use a multiple expansion to expand the system's Green's function. This allows to approximate the effects of distant clusters of bodies on a local group by a simpler representation, i.e. a hierarchical decomposition of space is used to define ever-larger clusters as distances increase.

Despite being based on a relatively simple idea, the numerical implementation is complicated. There are implementations available on the Internet from the Courant Institute for low Reynolds number problems where the Green's function considered is the one for a point force in an unbounded domain (stokeslet), or bounded by a wall (stokeslet near a wall) [112]. Here, since we ultimately want to study the multi-filament problem inside a sphere and such an implementation is missing, we decided to proceed through a different route based on computational optimization and reasoning.

4.2.1 Algorithm optimization

The coupled system of PDEs is numerically solved using the same algorithms as presented in Chapter 2 and 3. In particular, the equations are decoupled by considering the values at the previous time steps and the numerical stiffness bypassed through the SBDF scheme. Also, the background flow is computed by evaluating the Green's function for the specific geometry simulated (point force in unbounded domain or bounded by a wall), thus requiring the filament configuration to be in Cartesian coordinates. With regard to the presence of the other filaments, since their contribution is included by substituting the filaments with a line distribution of fluid-entraining follower forces, the integral of Eq. (4.9) is discretized using a number of elements N_{elem} such that the accuracy is bounded to 2% compared to the case where each grid point has a point force.

The multi-filament problem we are solving can be summarized in the following algorithm. Algorithm 1 represents a brute-force approach to the problem. Smarter ways of tackling it are in fact possible and faster. We initially implemented the algorithm in Matlab, then transitioned to Python and C++ (exploiting the 'Eigen' library). After inspecting the algorithm's performance with timers to identify potential bottlenecks and performing several optimization tests, we brought these changes.

Notoriously, Matlab and Python are particularly slow when dealing with for-loops and element-wise operations. For this, vectorial operations were used, even for computing derivatives by multiplying the vectors by the matrices with the coefficients of the finite

Algorithm 1 Multi-filament problem

1: Initialize vectors and matrices
2: Compute perturbed initial configurations
3: **function** SIMULATE FILAMENTS DYNAMICS
4: **while** $t <$ # time steps **do**
5: **for** $j = 1$ to N_{fil} **do** ▷ solve the equations of motion for each filament
6: **for** $k = 1$ to N_{pf} **do**
7: Compute velocity field produced by kth point force of jth filament by evaluating the *regularized* Green's function for the specific geometry
8: **for** $i = 1$ to N_{fil} and i $\neq$ j **do**
9: **for** $k = 1$ to N_{pf} **do**
10: Compute velocity field produced by the kth point force of the ith filament on jth filament by evaluating the Green's function for the specific geometry
11: **for** $i = 1$ to N_{fil} and k $\neq$ j **do**
12: Compute velocity field produced by presence of ith filament by:
13: (i) computing $\boldsymbol{f}(\boldsymbol{r}^{(i)})$
14: (ii) evaluating Green's function for the specific geometry N_{elem} times
15: Compute total background flow and derivatives
16: Solve equation for Lagrange multiplier
17: Solve PDE for filament configuration using SBDF method
18: Integrate filament arclength to obtain the configuration in Cartesian coordinates for the calculation of the background flow

differences. Moreover, it turned out that it is faster to run the outer for-loops N_{fil} times (line 5) than solving a larger system $(NN_{\text{fil}}) \times (NN_{\text{fil}})$. It is also significantly more efficient to use the programming languages' built-in functions, for instance to integrate the filament configuration at each time step, compared to writing them on our own. Lastly, one should notice that the total forces acting on each filament could be computed only once, as they do not vary. What changes are the evaluation points. This translates into moving line 13 to line 5 in the algorithm 1.

After all these improvements, which we label as 'Matlab optimized', the algorithm ran fairly faster. However, the main bottlenecks associated with the 'for-loops' at lines 6, 8, and 11 remained. We initially decided to use a combination of OpenCL and MPI for the C++ code. The former to parallelize nested loops as in lines 8 and 11, the latter to parallelize the outer loop at line 5. Despite using one node per filament, the improvement obtained was not at all satisfactory. This was because each node had to wait for the others before advancing in time, thus slowing down the whole algorithm. This alternative is computationally attractive only when the number of filaments is very large, i.e. $O(100)$. For this, we decided to transition to Python. In fact, a smart implementation allowed us to completely avoid the 'for-loops' related to the calculation of the background flow, which were replaced by simple

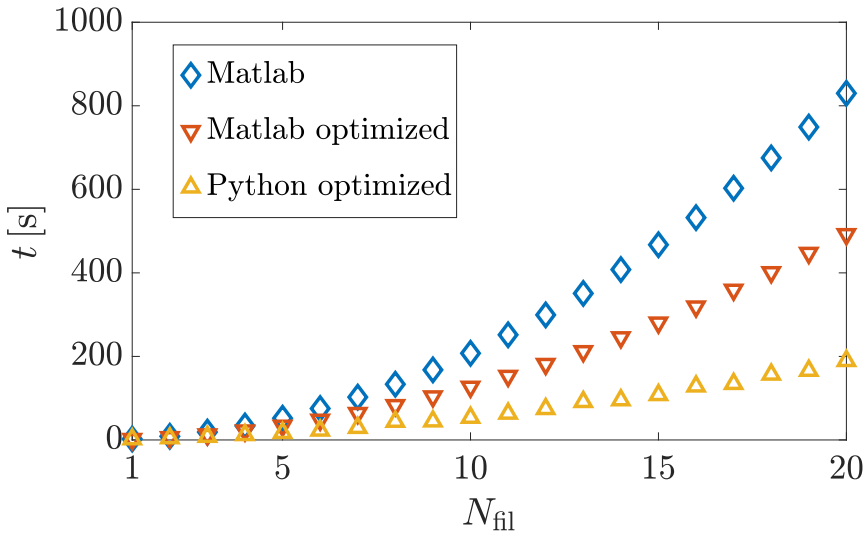

Fig. 4.2 Comparison between incremental optimized implementations to study the multi-filament problem. The data points were obtained running the algorithms for a line distribution of fluid-entraining follower forces with no wall for 1000 time steps. For this experiment, we used the same machine and took the best of three runs. The Python optimized implementation outperform the other ones in Matlab as it is up to 4.5 and 2.6 times faster, respectively.

dot products. This led to a considerable improvement, as we can see in Fig. 4.2. The plot compares the times required for the three implementations to run the algorithms for a line distribution of fluid-entraining follower forces with no wall 1000 time steps when varying the number of filaments. The Python optimized implementation as compared to Matlab and Matlab optimized is already 3 and 2 times faster, respectively with $N_{\text{fil}} = 5$ and reaches a 4.5 and 2.6 speed-up with $N_{\text{fil}} = 20$. The implementations were appropriately tested and cross-validated. Lastly, in all the simulations, the initial configurations of the filaments were randomly perturbed using a combination of sine and cosine waves with amplitudes in the hundredth-range of the filament length.

4.3 Results

4.3.1 The case of two filaments

Single fluid-entraining follower force

When an elastic filament is subject to a fluid-entraining follower force at its tip, beyond a certain value of the control parameter $\sigma^*_{N_{\text{fil}}=1}$ the system enters a limit cycle characterized by self-sustained oscillations. But what happens when two of such filaments are positioned next

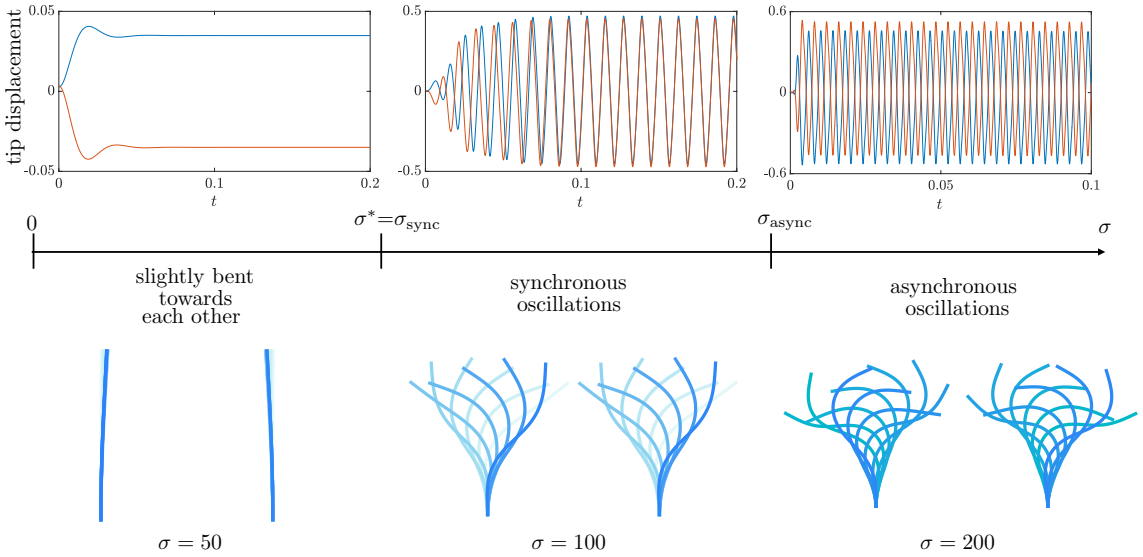

Fig. 4.3 Dynamics of a pair of parallel filaments with a single fluid-entraining follower force at their tips. Top row depicts the time evolution of the tip displacement, while the bottom row the time-lapse of the corresponding dynamics. Depending on σ, three distinct dynamics can be found. (i) The fluid flows set up by the point force entrain the filaments and push them towards each other, until they reach a steady, slightly bent, configuration. (ii) The filaments, thanks to the hydrodynamic coupling, synchronize their oscillations. (iii) For larger σ, the system exhibits oscillations, in which, depending on the value of the control parameter and the distance d, the difference in the phases of oscillation remains constant over time past a transient or reaches π.

to each other? By numerically solving the equations of motion including the appropriate fluid flows, we discover that the filaments can remarkably show *synchronous* beats. The value of the control parameter for which the filaments buckle and start self-sustained oscillations is only slightly larger than the one for the case of a single filament, $\sigma > \sigma^*_{N_{\text{fil}}=1}$, the reason being that the extensional fluid flow is larger (the total background flow includes the flows from both filaments), hence delaying the Hopf bifurcation. As we would expect, when the distance between the filaments increases, σ^* becomes closer to $\sigma^*_{N_{\text{fil}}=1}$ as the contribution coming from the fluid-entraining follower force on the other filament becomes weaker. As shown in Fig. 4.3, for $\sigma < \sigma^*$, the initial perturbations die out towards a steady configuration in which the filaments are slightly bent towards each other. This behaviour arises because the fluid flows in the region between the filaments mutually entrain them, thus leading to leaning filaments. After undergoing the Hopf bifurcation, the filaments enter their oscillatory regime and, past a transient, their phases of oscillation synchronize. Importantly, such

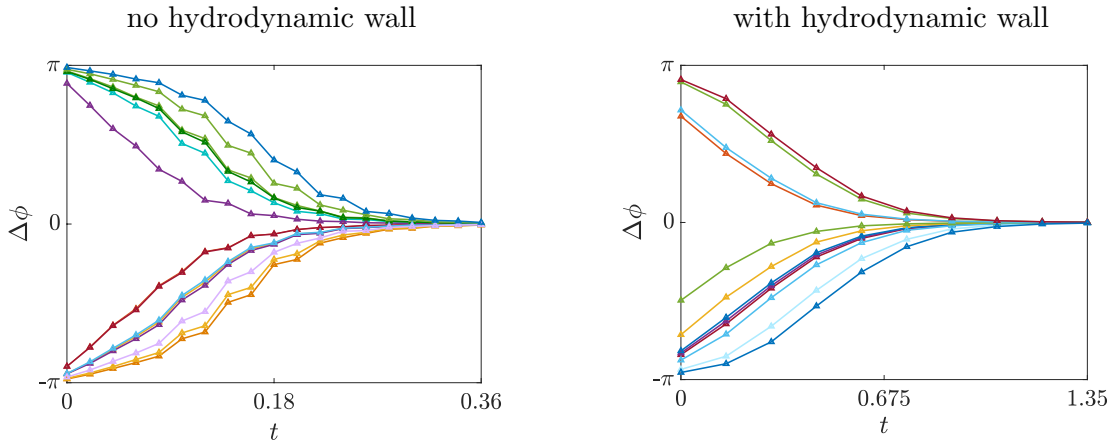

Fig. 4.4 Time evolution of phase difference for two filaments with fluid-entraining follower forces at their tips and distance $d = 1.4$ in the absence (a) and presence (b) of a hydrodynamic wall for $\sigma = 100$. All the 12 different initial perturbations considered yield to vanishing phase difference thus showing the robustness of the synchronization mechanism. When in the presence of a hydrodynamic wall, the filaments require longer times to synchronize their phases as the flows decay faster.

a synchronization is just the result of hydrodynamical coupling since, in our model, the filaments can only interact through the fluid. When the control parameter is sufficiently large, the compressive effect of the fluid-entraining follower force at the tip overcomes the hydrodynamic interactions. In this regime, depending on the strength of σ and the distance between the filaments, the difference in the phases of oscillation $\Delta\phi \equiv \phi_1 - \phi_2$ can either remain constant over time past a transient or, for larger values, reach π, thus corresponding to anti-phase synchronization. This result arises because the combination of the relative distance and the strength of the control parameter can lead to an equilibrium state in which the filaments are able to keep $\Delta\phi$ fixed or to one where equilibrium is found only by beating in anti-phase.

In order to show the robustness of the in-phase synchronization, we simulated the dynamics of 12 pairs of filaments with distance $d = 1.4$, all having different initial perturbations. We considered both the cases of fluid-entraining follower forces in the presence and absence of the wall, setting $\sigma = 100$ (well beyond σ^*). Fig. 4.4 shows that $\Delta\phi$ vanishes over time in both settings. If the wall is present, the flow decays faster ($1/r^2$ vs $1/r$ for a stokeslet in an unbounded domain), so the hydrodynamic coupling becomes weaker and the phase difference goes to zero more slowly.

Fig. 4.5 depicts how the synchronization time t_{sync} varies with the distance d and the control parameter σ. For large d, the background flow experienced by one filament sets up by the other one becomes smaller, and the time to synchronize t_{sync} increases. When keeping

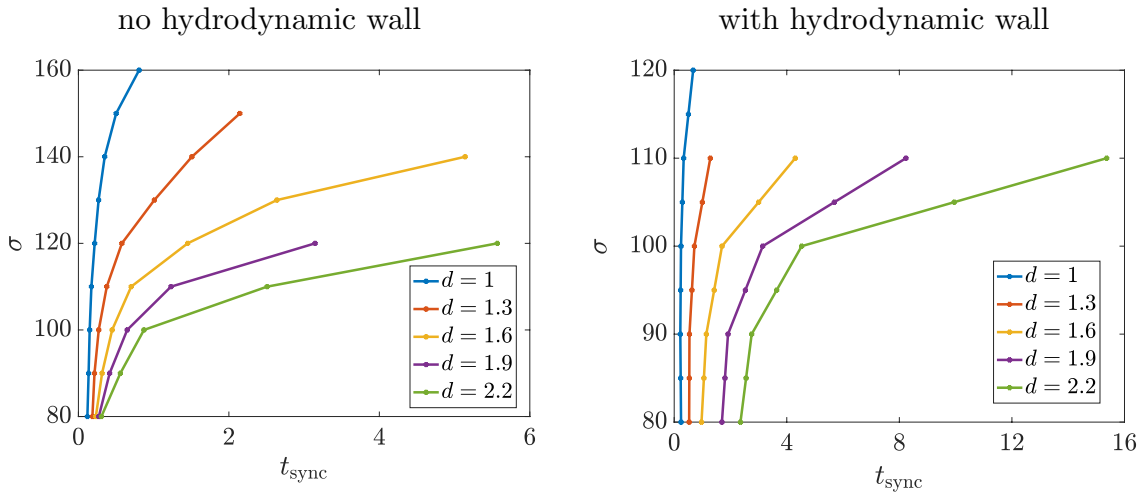

Fig. 4.5 Effect of distance on synchronization time for a filaments pair subject to a single fluid-entraining follower force while varying the control parameter σ. As the fluid flows in the wall case decay faster, the filaments need longer time to synchronize. When d is increased, the background flow experienced by one filament sets up by the other one becomes smaller, and t_{sync} increases. When keeping fixed d and varying the control parameter σ, we notice that for large σ the synchronization is delayed as the system approaches the value at which filaments exhibit asynchronous oscillations instead (σ_{async}).

fixed d and varying the control parameter σ, we notice that for large σ the synchronization is delayed as the system approaches the value at which filaments exhibit asynchronous oscillations instead (σ_{async}). Again, as the fluid flows in the wall case decay faster, the filaments need longer time to synchronize.

Line of fluid-entraining follower forces

We now turn to the study of a system with the same set-up as in the previous section, but this time the fluid-entraining follower force at the tip is replaced by a line of them. Also in this case we discover that the two filaments can synchronize their beating motion. Our numerical results show that the emerging dynamics vary depending on the geometry considered for the flow, i.e. either unbounded or bounded by a wall.

If the wall is present, three possible dynamical regimes can be identified when progressively increasing the control parameter Σ (Fig. 4.6). (i) The initial random perturbations decay and the filaments reach an equilibrium configuration where they are slightly bent towards each other, assuming a concave configuration with their tips closer than any other point. (ii) The filaments buckle and enter a limit cycle with self-sustained oscillations in which, after a transient, they synchronize in-phase their beats ($\Sigma^* \equiv \Sigma^{in}_{sync}$). Lastly, (iii)

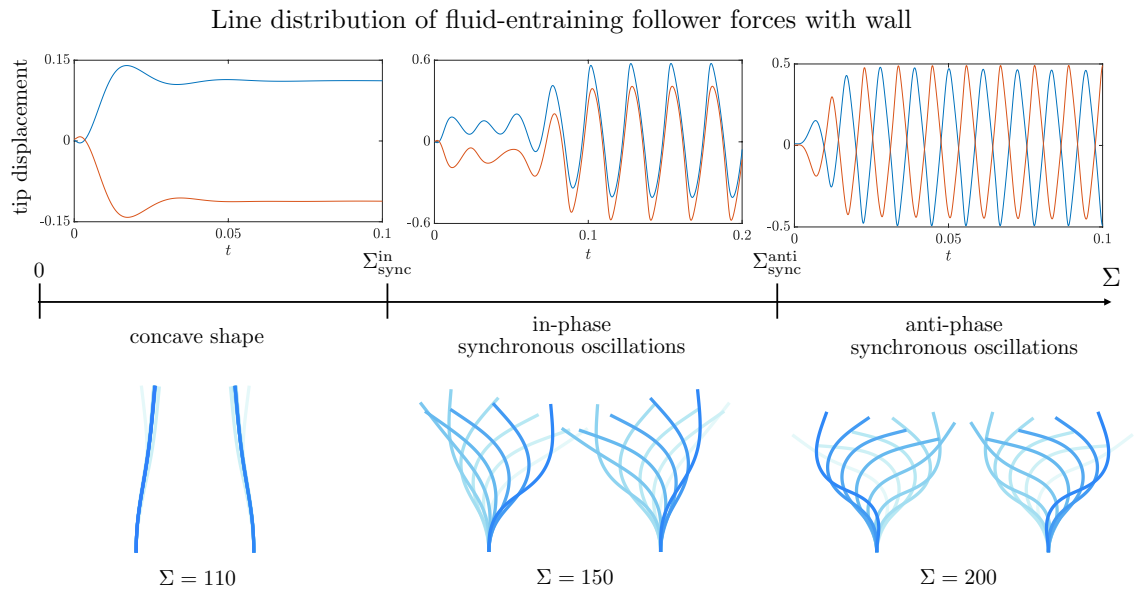

Fig. 4.6 Dynamics of a pair of filaments with a line distribution of fluid-entraining follower forces in the presence of a wall. Top row depicts the time evolution of the tip displacement, while the bottom row the timelapse of the corresponding dynamics. Three regimes can be identified for increasing values of Σ: (i) the filaments lean towards each other, reaching a steady concave shape; (ii) they buckle and, past a transient, they synchronize in-phase their motion; (iii) when the compressive effects overcome the hydrodynamic coupling, they exhibit anti-phase synchronous oscillations.

anti-phase synchronous self-sustained oscillations arise for $\Sigma \geq \Sigma^{\text{anti}}_{\text{sync}}$. To test the robustness of the synchronizations, we considered 12 distinct initial configurations, set the distance $d = 1$ and the control parameter $\Sigma = 140$ and $\Sigma = 180$, i.e. within the range for in-phase and anti-phase oscillations, respectively. As shown in Fig. 4.8a, the initial perturbations do not affect the resulting dynamics as the phase difference $\Delta\phi$ always vanishes or reaches π.

When there is no such a wall, the filaments hydrodynamically interact differently. Specifically, as depicted in Fig. 4.7, for increasing values of the control parameter Σ, (i) the perturbations die out and the filaments reach a steady convex configuration with the tips further apart than some middle point in their bodies. (ii) In the second dynamical regime, the filaments buckle and begin to oscillate, quickly synchronizing their motion to beat in *anti-phase* ($\Delta\phi = \pi$). So, $\Sigma^* \equiv \Sigma^{\text{anti}}_{\text{sync}}$. (iii) Lastly, when Σ is increased further, the filaments synchronize their motion with the phase difference going to zero. The physical explanation behind the convex shape being assumed is the different background flow acting on the filaments. In the presence of a wall, the velocity field in the direction perpendicular to the straight configuration (i.e. in the x-direction) is always pushing the filaments towards each

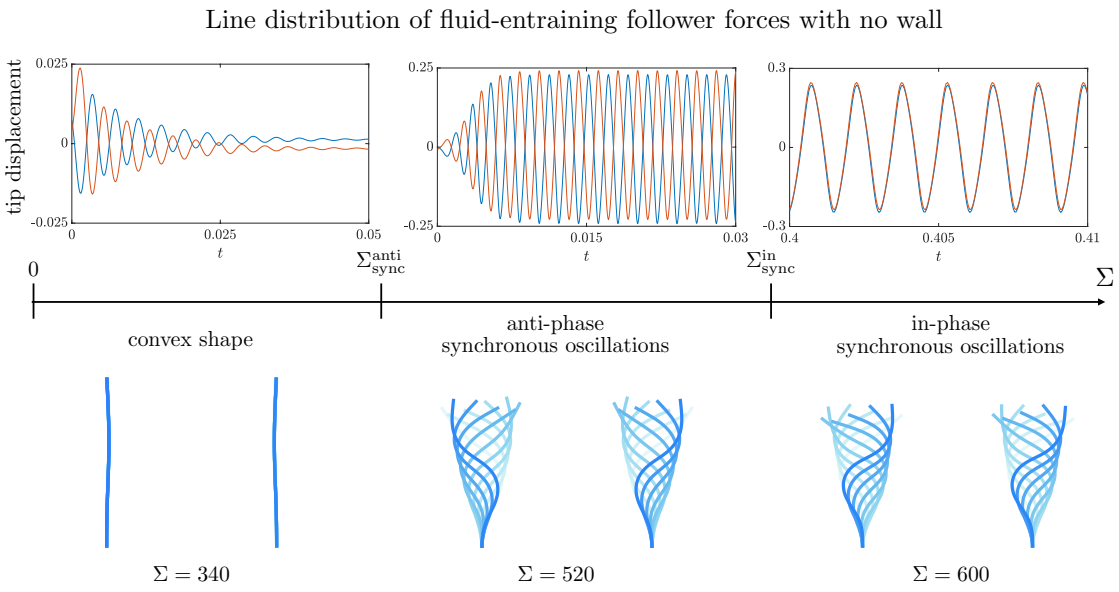

Fig. 4.7 Dynamics of a pair of filaments with a line distribution of fluid-entraining follower forces in the absence of a wall. Top row depicts the time evolution of the tip displacement, while the bottom row the timelapse of the corresponding dynamics. Similarly to the wall-case, three regimes emerge. However, because of the different fluid flows, these are different. (i) The filaments experience attractive flows in the first half of their length, and repulsive ones in the second half. This leads to a convex shape, with the tips pointing in opposite direction. (ii) The dynamics post-buckling consists in anti-phase synchronous motion. (iii) For larger Σ, the filaments can eventually synchronize in-phase.

other, monotonically increasing its strength from $s = 0$ to $s = 1$. The same behaviour is found when there is only a single point force acting at the tip, regardless of the Green's function used. It is only by combining a collection of point forces and the no-wall condition that the velocity field drastically change. In the region $0 \leq s \lessapprox 1/2$, the fluid flow pushes the filaments towards each other, while it pushes them away when $1/2 \lessapprox s \leq 1$. This is because at $s \approx 1/2$, the velocity field changes sign yielding to filaments that are entrained in the first half of their length and diverted in the second half.

To prove the robustness of the anti- and in-phase synchronization, we again simulated 12 pairs of filaments with fixed distance $d = 1$ and random initial perturbations and set $\Sigma = 480$ and 600. Fig. 4.8b shows that for all the pairs the phase difference always reaches π or 0, respectively. Notice that the self-sustained oscillations, because of the high Σ and the line distribution of forces that compress the filaments, show S-shape beats, similar to snakes' serpentine motion. Also, at $\Sigma \approx 2800$, the compressive force becomes strong enough to almost make the filaments collapse on themselves.

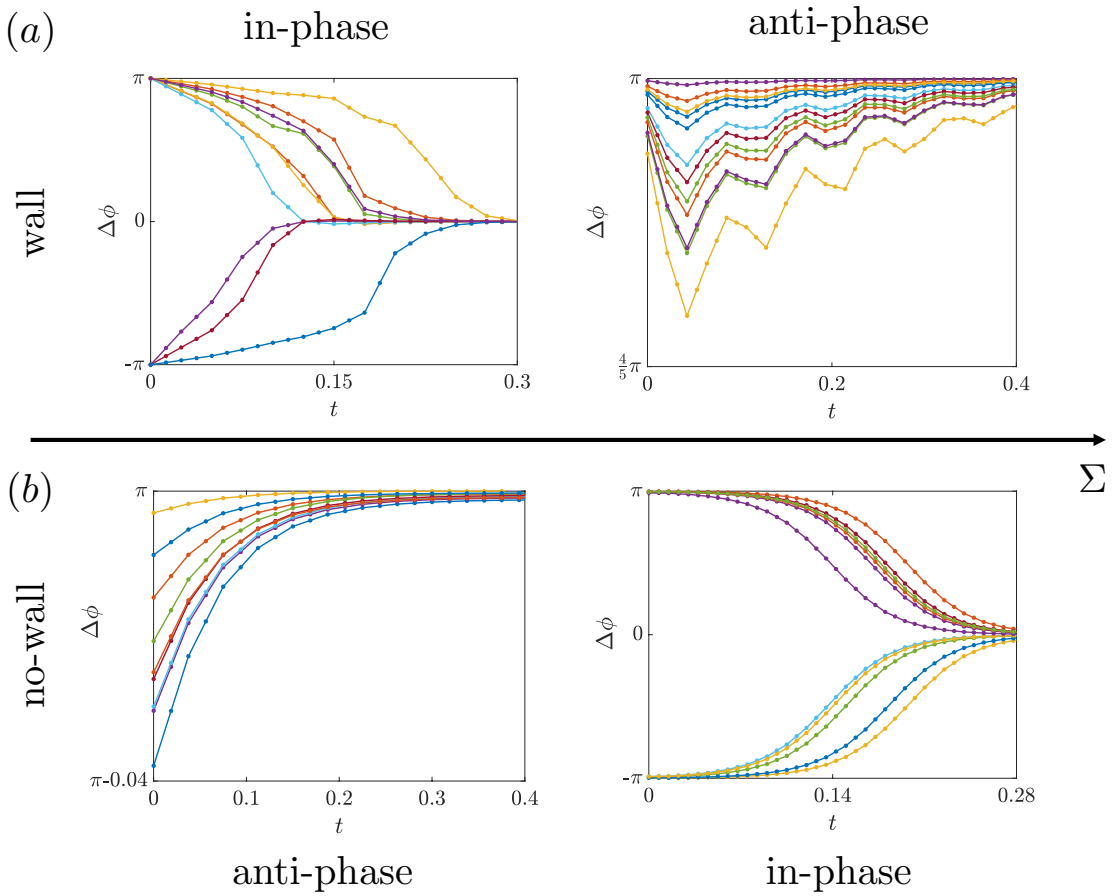

Fig. 4.8 Independence on initial configuration for the dynamics of two parallel filaments with a line distribution of fluid-entraining follower forces. Top row shows the results for the wall-case with $d = 1$, $\Sigma = 140, 180$, while the bottom row for the no-wall case with again $d = 1$, but $\Sigma = 480, 600$, left to right. For both in-phase and anti-phase synchronization in the two geometries considered, the phase difference of all the different random perturbations imposed converges to either 0 or π.

But why do we observe these opposite behaviours for the two geometries? The reason lies in the fluid flows being created. For the wall-case, each filament initially assumes a concave shape in which the velocity field induced by the other one tends to push them towards each other. After buckling, the filaments are therefore more prone to synchronizing as the fluid flows are already favouring this. On the other hand, in the no-wall case, the filaments have a convex configuration and the fluid flows favour in-phase oscillations only in the first half of the filament length. It is therefore required to pass a 'hydrodynamic barrier' to allow in-phase motion, and this can only occur for larger Σ.

For a filaments pair with a line distribution of fluid-entraining follower forces, the geometry considered can significantly affect the value of the control parameter at which

Distance d	$\Sigma^{\text{in}}_{\text{sync}}$
1	580
1.3	610
1.6	630
1.9	640
2.2	650

Table 4.1 Critical values of the control parameter Σ for in-phase synchronization for a pair of filaments subject to a line distribution of fluid-entraining follower forces.

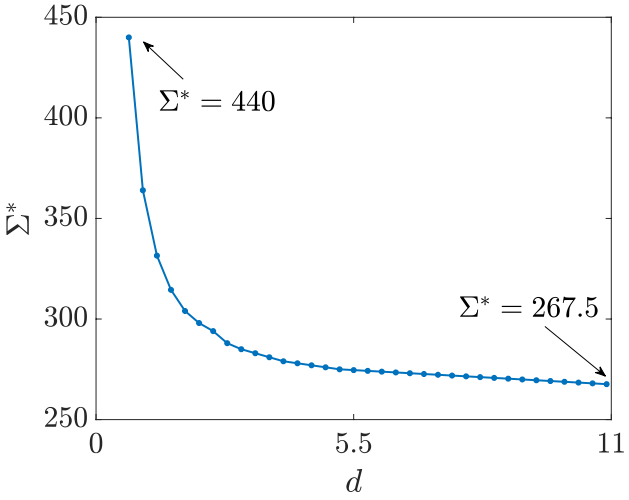

Fig. 4.9 Dependence of the critical value of the control parameter on the distance between the filaments for the no-wall-case. The slowly decaying flows significantly affect Σ^*: for $d = 0.7$, $\Sigma^* \approx 440$, while for $d = 11$, $\Sigma^* = 267.5$, i.e. close to $\Sigma^*_{N_{\text{fil}}=1} = 261.1$.

the Hopf bifurcation occurs. In the presence of the wall, the flows rapidly decay and $\Sigma^* \approx \Sigma^*_{N_{\text{fil}}=1} = 124.2$, regardless of the distance d. Conversely, in an unbounded domain, the slowly decaying flows yield Σ^* to range from $\Sigma^* = 440$ for $d = 0.7$, about 1.5 times larger than $\Sigma^*_{N_{\text{fil}}=1} = 261.1$, to $\Sigma^* = 267.5$, when the distance is increased to 11 times the filament length, as we can see in Fig. 4.9. Similarly, while for the wall case the values at which the filaments synchronize in-phase and anti-phase are fairly independent on the distance d, being approximately $\Sigma^{\text{in}}_{\text{sync}} \approx 130$ and $\Sigma^{\text{anti}}_{\text{sync}} \approx 170$, for the no-wall case, these are considerably affected by d as summarized in Table 4.1.

Fig. 4.10 presents how the time at which the filaments synchronize in-phase, t_{sync}, varies with the distance between the filaments for both geometries considered. In the absence of the wall, the in-phase oscillations are followed by no other dynamical regime, so we observe

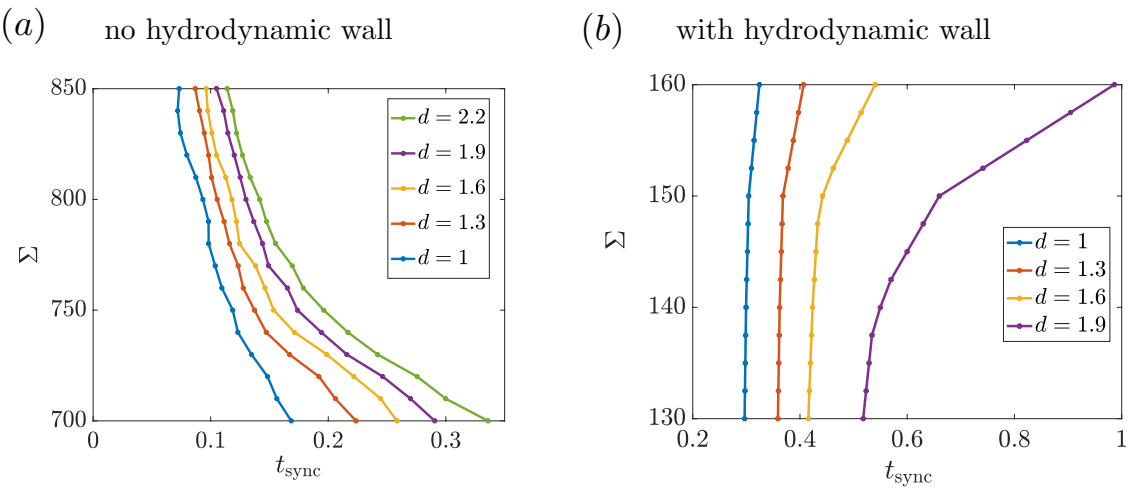

Fig. 4.10 As the filaments are further apart, the fluid flows induced become weaker, so requiring longer time to synchronize. (a) In the absence of the wall, the in-phase oscillations are followed by no other regime. The synchronization time decreases when the filaments are closer to each other and the control parameter is larger. (b) For the wall-case, t_{sync} increases for larger Σ as the system approaches $\Sigma^{\text{anti}}_{\text{sync}}$ at which anti-phase oscillations arise instead.

that the synchronization time decreases when the filaments are closer to each other and the control parameter is larger. On the other hand, in the presence of the wall, t_{sync} increases for larger Σ as the system approaches the anti-phase synchronous dynamical regime.

4.3.2 The case of many filaments

After a study of the dynamics of two filaments acted on by fluid-entraining follower forces, we now tackle the collective buckling for $N_{\text{fil}} > 2$. We follow the same structure of the previous section in which we firstly examine the instance where the filaments have only a single fluid-entraining follower force at their tip and then proceed with a line distribution of such forces. In this problem, there are many degrees of freedom, from the ratio d/L, to the relative distance between the filaments. Here, we keep the distance d between them fixed and set it to a value such that overlapping cannot occur, and consider the no-wall case so that the hydrodynamic interactions are maximum. We find that already in this set-up, the emerging dynamics are various and peculiar.

Single fluid-entraining follower force

The case $N_{\text{fil}} = 2$ reveals that the hydrodynamic interactions can yield to synchronized beating motion. For higher filament density, we studied a system with $N_{\text{fil}} = 3, \ldots, 10$,

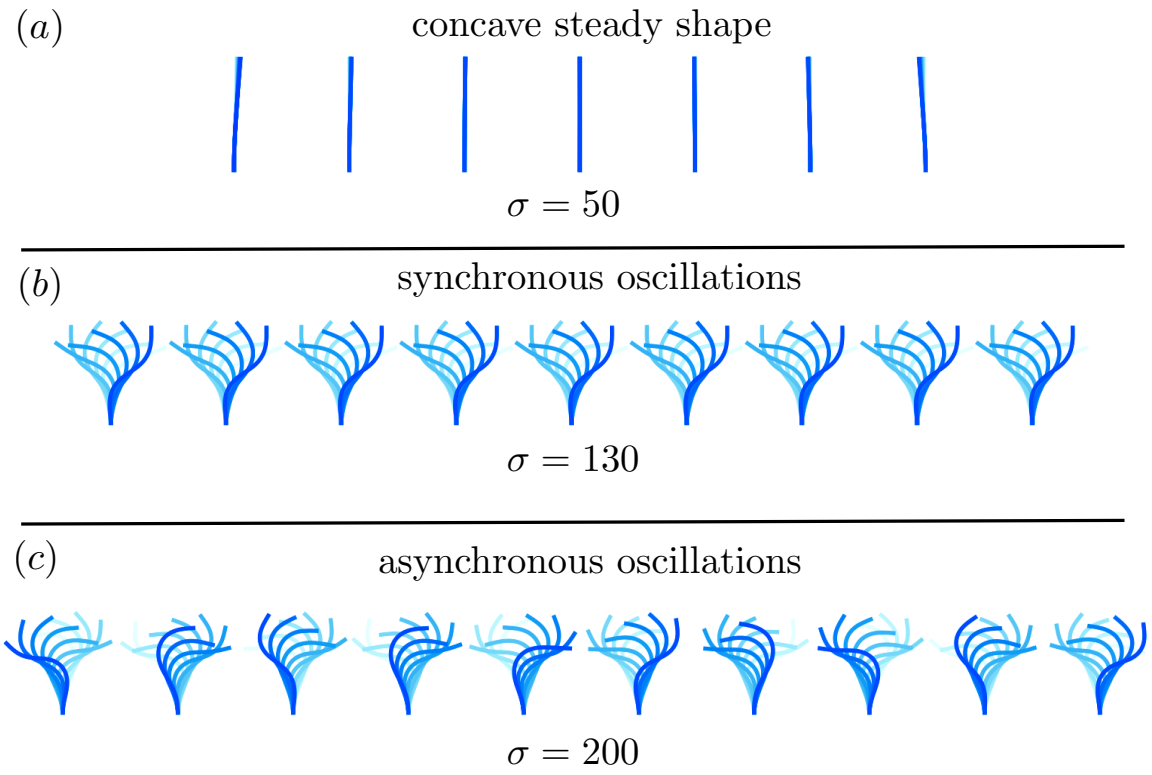

Fig. 4.11 Time-lapse of the possible dynamics for an array of filaments subject to a single fluid-entraining follower force at the tip with no-wall. (a) The filaments are entrained by the fluid flows and lean towards the centre in a symmetric fashion, assuming a concave steady bent shape. (b) After buckling, the fluid-structure interaction allows the filaments to synchronize their oscillations. (c) For larger values of the control parameter, the compressive effect of the fluid-entraining forces dominates over the hydrodynamic coupling, thus yielding asynchronous oscillations.

distance between them $d = 1.4$, and varied the control parameter in the range $0 < \sigma < 300$. We discovered the existence of the same three regimes observed for two filaments, depicted in Fig. 4.11. For $\sigma < \sigma^*$, the filaments reach a stationary concave configuration, showing a mirror symmetry with respect to the $x = 0$ axis (Fig. 4.11a). If N_{fil} is odd, then, as we would expect, the filament in the middle returns to a straight configuration instead (the velocities in the x-direction are equal and opposite and therefore cancel out). When $\sigma \geq \sigma^*$, self-sustained oscillations arise and the filaments synchronize (Fig. 4.11b, 4.12a). Unsurprisingly, the critical value of the control parameter at which the filaments buckle and begin to oscillate increases with the number of filaments. This is due to the extensional flows that act opposite to the compressive force and become more vigorous with N_{fil}, thus delaying the onset of the Hopf bifurcation. We also notice that when σ approaches σ_{async}, the time to synchronize

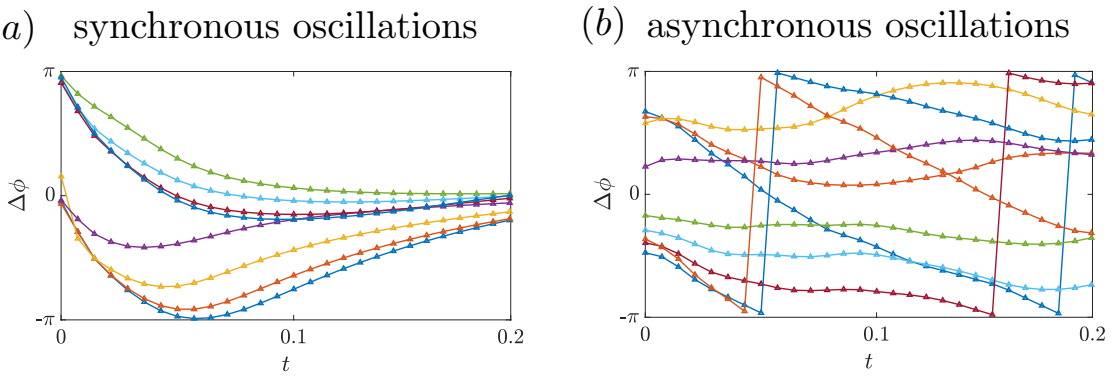

Fig. 4.12 Time evolution of the phase difference $\Delta\phi$ computed as $\phi_i - \phi_1$ for $i = 2,\ldots,9$. (a) After a transient that depends on the initial configuration, all the filaments synchronize and $\Delta\phi$ goes to zero. (b) In the asynchronous regime, every filament moves independently and the phase difference constantly varies. N.B. The discontinuities are because, for graphical purposes, we constrained $\Delta\phi$ to be in the range $[-\pi,\pi]$.

increases. Despite creating stronger flows, higher σ also corresponds to stronger compressive effects. It is this 'tug-of-war' mechanism, in which hydrodynamics prevails, that postpones the synchronization. From $\sigma = \sigma_{\text{async}}$, the compressive forces dominate instead, thus leading to asynchronous oscillations in which each filament beats independently and defining the third dynamical regime (Fig. 4.11c). In this case, the phase difference constantly changes over time as presented in Fig. 4.12b. Again, σ_{async} increases when the filaments become more abundant.

Line of fluid-entraining follower forces

The more vigorous background flows set up by a line distribution of fluid-entraining follower forces give rise to unexpected dynamics. We considered a system with a number of filaments ranging from 3 to 10 and distance $d = 0.7$ and varied the control parameter $0 < \Sigma < 2500$.

We identified five regimes, summarized in Fig. 4.13. The values of Σ at which the transition from one to the next occurs are independent on the initial conditions, similarly to what was presented for a filament pair. When studied a single filament, the possibility for the system to present hysteresis at the Hopf bifurcation was investigated and it was found that it did not occur. We believe that hysteresis would not occur also for the multi-filament case.

The common regime independent on the filament density is the one where the filaments slightly bend towards each other assuming a convex shape and keeping a mirror symmetry. The filament curvature increases from the middle filaments to the outer ones because of the progressive sideways imbalance of the flows experienced by the filaments themselves

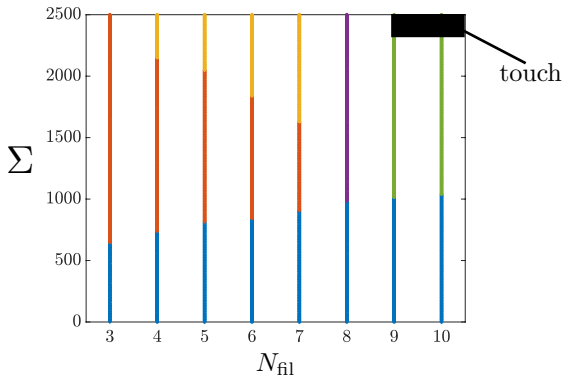

	Σ							
N_{fil}	3	4	5	6	7	8	9	10
✳ convex steady	< 650	< 740	< 815	< 845	< 910	< 985	< 1015	< 1040
✳ in-phase sync. oscill.	≥ 650	740-2150	815-2050	845-1840	910-1630	–	–	–
✳ anti-phase sync. oscill.	–	≥ 2150	≥ 2050	≥ 1840	≥ 1630	–	–	–
✳ bent w/ oscillations	–	–	–	–	–	≥ 985	–	–
✳ bent steady	–	–	–	–	–	–	≥ 1015	≥ 1040

Fig. 4.13 Summary of the possible dynamics for an array of filaments subject to a line distribution of fluid-entraining follower forces. Both the control parameter Σ and the filament density play a key role in determining the resulting dynamics. The filaments can synchronize in-phase and anti-phase, as well as lead to a symmetry-breaking mechanism in which they all bend in the same direction.

(Fig. 4.14a). After buckling, for $3 \leq N_{\text{fil}} \leq 7$, the filaments begin to oscillate describing the S-shape undulatory motion previously mentioned for $N_{\text{fil}} = 2$, and synchronize in-phase (Fig. 4.14b). However, despite beating in synchrony, differently from all the previous cases encountered, the filament shapes cannot be superimposed. In fact, by reason of the flows imbalance mentioned above, the filaments at the sides have progressively more 'curly' shapes than the central ones; this becomes even more pronounced with higher filament density. For $N_{\text{fil}} = 3$, the regimes just described are the only possible ones, while for $4 \leq N_{\text{fil}} \leq 7$ another dynamics emerges. For larger Σ, the filaments show anti-phase synchronous oscillations; these are mirrored with respect to the $x = 0$ axis if N_{fil} is odd, as depicted in Fig. 4.14c. If N_{fil} is even instead, the central filament randomly synchronizes in phase with one of the two sides. For $N_{\text{fil}} \geq 8$, after the convex-shape regime, the stronger background flows created by the fluid-entraining follower forces amplify the initial perturbations and yield to a *spontaneous symmetry breaking* mechanism. As shown in Fig. 4.14d, when $N_{\text{fil}} = 8$ and $\Sigma \geq 1050$, all the filaments bend in the same direction until reaching a configuration characterized by high-frequency, small-amplitude oscillations around a bent shape (Fig. 4.14d, inset). Also,

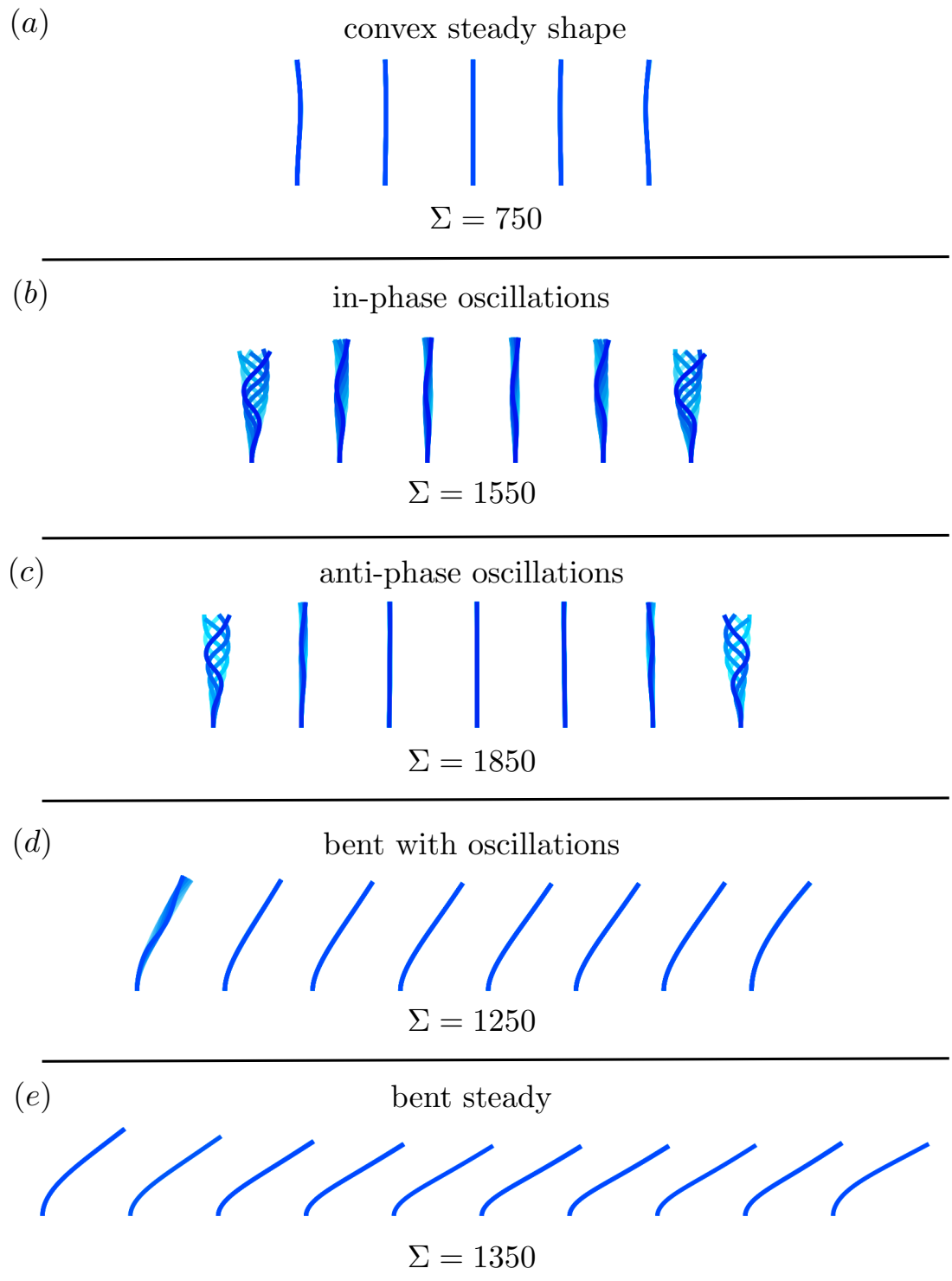

Fig. 4.14 Time-lapse of the possible dynamics for an array of filaments with a line distribution of fluid-entraining follower forces. (a) Before buckling, the filaments reach a convex steady shape as the total fluid flow set up by the point forces is such that it pushes towards each other the first half length of each filament and away the second half. (b)-(c) After buckling, the filaments begin to oscillate describing S-shape configurations and eventually synchronize their motion in-phase or anti-phase. (d)-(e) Above a certain filament density, the filaments lean all in the same direction and reach either a steady bent configuration or one with small-amplitude, high-frequency oscillations around a bent state.

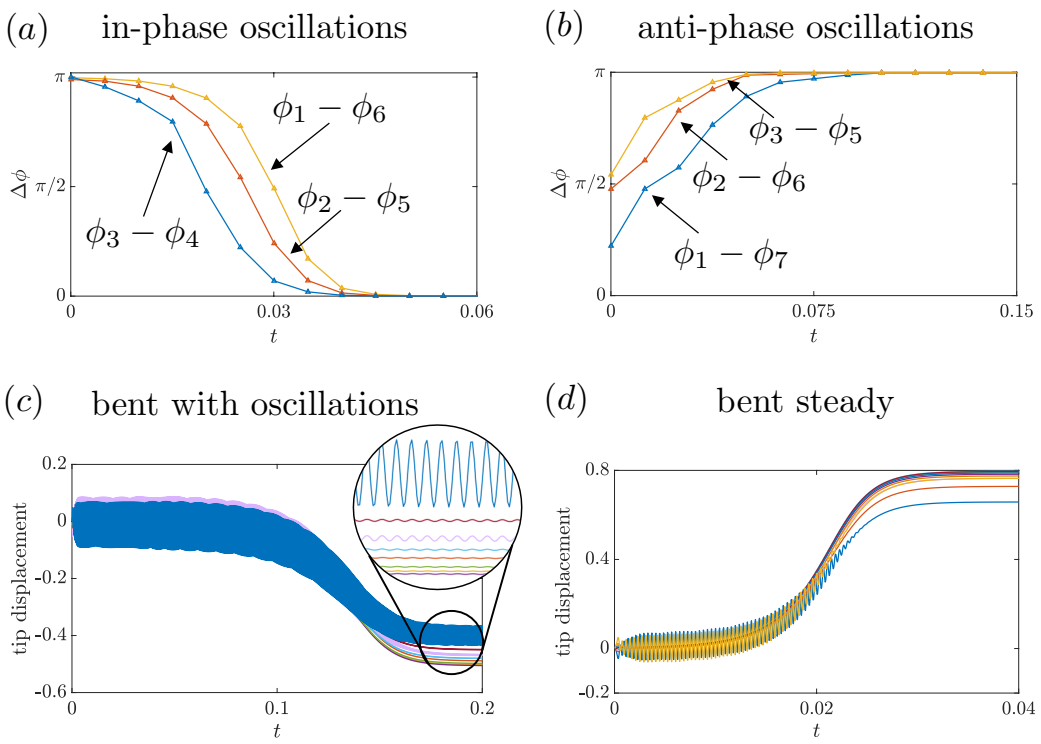

Fig. 4.15 (a), (b) The phase difference for each pair of opposite filaments (numbered from left to right) vanishes over time or reaches π, corresponding to in-phase and anti-phase synchronous oscillations. Results computed for an array of $N_{\text{fil}} = 6$ and $\Sigma = 1550$, and $N_{\text{fil}} = 7$ and $\Sigma = 1850$, respectively. (c) Time evolution of the tips displacement. The filaments spontaneously bend towards the same direction, thus breaking the system's symmetry, while oscillating. They eventually reach a configuration where they exhibit small-amplitude, high-frequency oscillations around a bent state. Data shown are for $N_{\text{fil}} = 8, \Sigma = 1250$. (d) For $N_{\text{fil}} \geq 9$, fluid-structure interactions give rise to a spontaneous symmetry breaking mechanism in which they lean in the same direction and reach a steady bent configuration. Data shown are for $N_{\text{fil}} = 10, \Sigma = 1350$. Notice that we favoured plotting the tip displacement instead of the phase difference for instances (c) and (d) as we thought it was more representative of the dynamics as $\Delta\phi$ goes to zero in both cases.

the curvature of the filaments increases in the direction they are bent towards since the fluid flows are more vigorous. For $N_{\text{fil}} = 9$ and $\Sigma > 1050$ and $N_{\text{fil}} = 10$ and $\Sigma > 1000$, the system undergoes a similar transition but, in this instance, all the filaments achieve a *steady* bent configuration instead. In both regimes, the direction the filaments lean towards (right or left) is random and dictated by the ones at the extremes of the array, in which one prevails on the other thus triggering this instability.

Fig. 4.15a-b plot the time evolution of the phase difference for opposite filaments, from the external to the internal ones (filaments are numbered from left to right). As previously

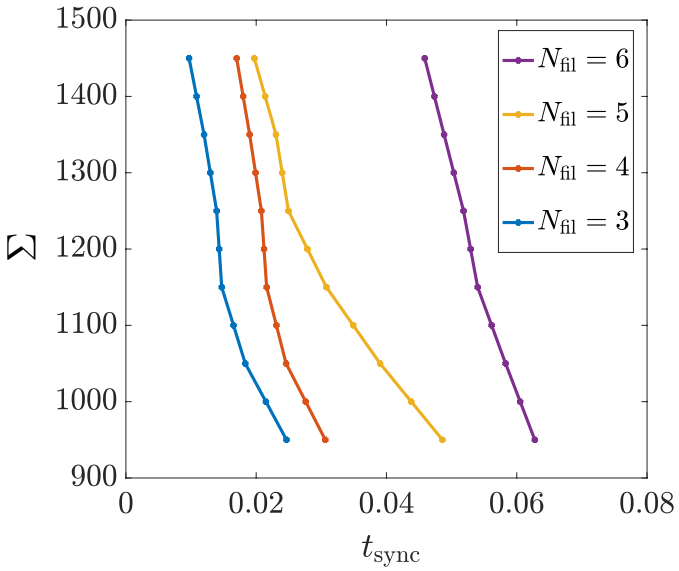

Fig. 4.16 Effect of filament density and the control parameter on in-phase synchronization time. When Σ increases, the background flows become more vigorous thus anticipating the synchronization. Interestingly, higher filament density corresponds to larger t_{sync}. This behaviour occurs because the hydrodynamic coupling needs to be experienced by the whole array of filaments, so the longer the array, the larger the synchronization time is.

mentioned, $\Delta\phi$ either vanishes or reaches π, scenarios corresponding to in-phase and anti-phase synchrony. The results shown are for an array of $N_{\text{fil}} = 6$ with $\Sigma = 1550$, and $N_{\text{fil}} = 7$ with $\Sigma = 1850$, respectively. Fig. 4.15c-d show how the tip displacement evolves over time for both the case with filaments oscillating around a bent configuration and steadily reaching a bent shape. The filament density is crucial in determining which regime will occur.

Fig. 4.16 compares how t_{sync} varies with the number of filaments for a wide range of values of the control parameter. When Σ increases, the background flows become more vigorous thus anticipating the synchronization. Interestingly, higher filament density corresponds to larger t_{sync}. This behaviour occurs because the hydrodynamic coupling needs to be experienced by the whole array of filaments, so the longer the array, the larger the synchronization time is. It should be stressed that the initial conditions of the filaments configuration do not affect the values of the control parameter at which the transitions occur, but they bear upon the timescales. For this, all results related to times comparison were obtained imposing the same initial conditions.

Concerning the bent steady configuration, larger Σ and N_{fil} lead to both the system reaching the equilibrium more swiftly and more bent shapes, as displayed in Fig. 4.17, eventually causing the filaments to touch and overlap. This occurs at $\Sigma = 2450$ and 2350 for $N_{\text{fil}} = 9$ and 10, respectively.

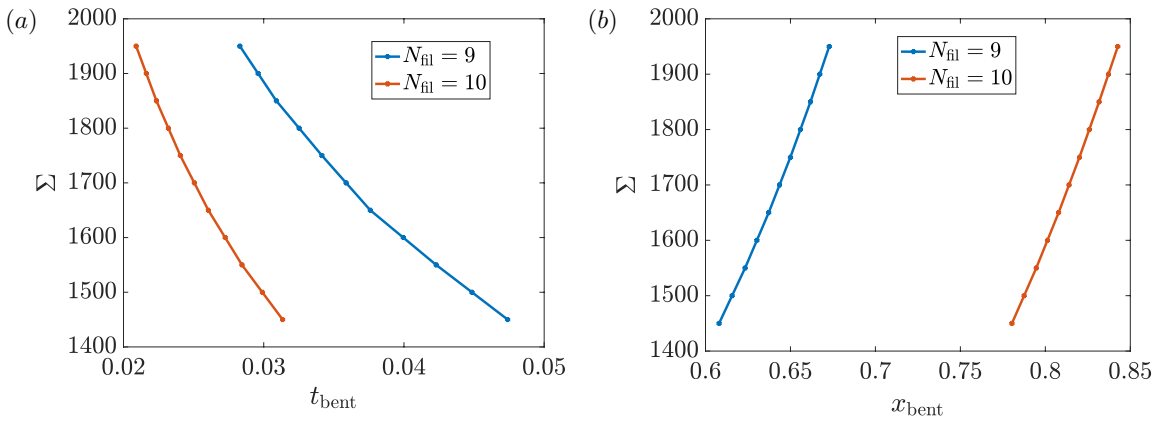

Fig. 4.17 Beyond a certain filament density, the system undergoes a spontaneous symmetry-breaking mechanism in which filaments lean in the same direction and eventually reach a steady bent configuration. (a) The flows become more vigorous for both larger Σ and N_{fil}, resulting in lower t_{bent}. (b) Similarly, the filaments become progressively more bent when varying the same parameters. The figure plots the tip displacement of the last filament to the right, i.e. the one most bent.

4.3.3 Periodic boundary conditions

When tackling the multi-filament problem, if the number of filaments is very large, one could consider the limit case of a set of filaments subject to fluid-entraining follower forces with periodic boundary conditions. This would translate into using the Green's function for a point force with periodic boundary conditions. Again, a regularization should be used to properly account for the fluid flow. This approach would clearly reduce the computational cost as fewer filaments would need to be simulated. However, it is worth noting that the choice of the number of filaments with periodic boundary conditions would prove crucial to avoid excluding dynamical regimes. In fact, by considering, for instance, only two filaments, we would not capture the bent phases, which we showed arises beyond a certain filament density. All in all, despite being attractive in terms of reducing the operations involved, we decided not to follow this approach to characterize the collective dynamics of interacting filaments.

4.4 Discussion

The mathematical model we have developed and employed to tackle the collective buckling for an array of parallel filaments unveiled a wide range of dynamics. Despite its reductionist nature, our model includes all the key features that appear in the real biological system,

among which the fluid flows induced by the presence of the other filaments. Our numerical study showed that the hydrodynamic coupling can remarkably lead to synchronized motion and give rise to a new symmetry-breaking mechanism. In particular, when subject to a single fluid-entraining follower force at the tip, the filaments can synchronize their self-sustained oscillations. For a line distribution of such forces, the filaments can spontaneously lean in the same direction, thus breaking the system's symmetry, and ultimately reach a steady bent configuration. Crucially, the filament density appears to be the key parameter for the onset of such phenomenon. To explain the mechanism underpinning all the dynamics observed, we proposed physical considerations based on the mutual entrainment in the flows set up by the filaments. The study of an array of filaments subject to fluid-entraining follower forces revealed interesting dynamics, but what happens when such filaments are inside a sphere? How does the geometry affect the emerging dynamics? Chapter 5 presents and thoroughly discusses this analysis.

Chapter 5

The motion of filaments inside a sphere

After developing a robust and efficient algorithm to study the fluid-structure interaction of a multitude of filaments subject to fluid-entraining follower forces, we can now tackle the multi-filament problem inside a sphere. In this chapter, we investigate the role of confinement; specifically, how it affects the filaments dynamics and whether it can lead to phenomena similar to the ones found experimentally in *Drosophila* oocytes, discussed in detail in Chapter 1. Sec. 5.1 summarizes the modelling assumptions and introduces the system set-up, Sec. 5.2 presents the results for both a single and a line distribution of fluid-entraining follower forces, and Sec. 5.3 discusses our findings and their biological relevance.

5.1 System set-up

The framework developed so far is now applied and extended to a simplified and tractable model of the real oocyte. Its shape is approximated by a sphere, MTs are represented by inextensible elastic slender filaments confined to moving in its mid-plane, and the motor-cargo ensemble is treated as a fluid-entraining follower force. Also, the same 2D description presented in the previous chapters for the filaments is used to model their dynamics and the linearity of Stokes equations is exploited to compute the total background flow. The cytoplasmic streaming is appropriately modelled by superimposing the fluid flows created by the fluid-entraining follower forces on all the filaments as well as the ones induced by their movement. Fig. 5.1 depicts the schematic representation of the system.

5.1.1 Point force inside a sphere

By modelling the motor-cargo ensemble with fluid-entraining follower forces and approximating the system geometry by a spherical container, we can take advantage of the analytical

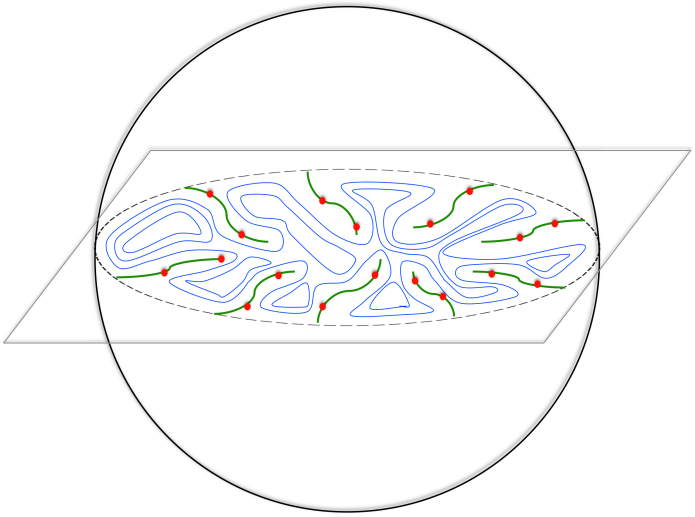

Fig. 5.1 Schematic of the multi-filament system inside a sphere. In red are the fluid-entraining follower forces, in green the filaments, and in blue the fluid flow.

solution for the velocity field of a point force with magnitude F_{pf}, located at $\boldsymbol{x}_0$ inside a sphere with unit radius, $a = 1$ [113, 114]. These simplifications allow us to compute the background flow by evaluating the analytic solution directly, instead of numerically solving Stokes equations for the fluid flow. Using the appropriate Green's function, which satisfies the no-slip boundary conditions at the sphere wall, obviates the need to discretize the sphere. This reduces the complexity of the simulations and, most importantly, the computational time, while still capturing the physics of the real system.

The m$^{\mathrm{th}}$ component of the velocity field reads

$$u_{\mathrm{pf_m}} = \frac{F_{\mathrm{pf_m}}}{8\pi\mu}\left[G_{\mathrm{jm}}\left(\boldsymbol{x}-\boldsymbol{x}_0\right)+\bar{G}_{\mathrm{jm}}\left(\boldsymbol{x}\right)\right], \tag{5.1}$$

where μ is the dynamic viscosity of the fluid, G_{jm} the Green's function, defined by

$$G_{\mathrm{jm}}\left(\boldsymbol{x}-\boldsymbol{x}_0\right) = \frac{\delta_{\mathrm{jm}}}{r}+\frac{\left(x_{\mathrm{j}}-x_{0_{\mathrm{j}}}\right)\left(x_{\mathrm{m}}-x_{0_{\mathrm{m}}}\right)}{r^3}, \tag{5.2}$$

and

$$\begin{aligned}\bar{G}_{\mathrm{jm}}(\boldsymbol{x}) = \hat{e}_{\mathrm{m}}\hat{e}_{\mathrm{k}}\Bigg\{ & \frac{1-3R_0^2}{2R_0^3}\, G_{\mathrm{jk}}(\boldsymbol{x}-\bar{\boldsymbol{x}}_0) - \frac{1-R_0^2}{R_0^4}\, \hat{e}_{\mathrm{l}}\, G_{\mathrm{jk},l}(\boldsymbol{x}-\bar{\boldsymbol{x}}_0) \\ & - \frac{(1-R_0^2)^2}{4R_0^5}\, \nabla^2 G_{\mathrm{jk}}(\boldsymbol{x}-\bar{\boldsymbol{x}}_0) \Bigg\} + (\delta_{\mathrm{km}} - \hat{e}_{\mathrm{k}}\hat{e}_{\mathrm{m}}) \Bigg\{ \frac{3R_0^2-5}{2R_0^3}\, G_{\mathrm{jk}}(\boldsymbol{x}-\bar{\boldsymbol{x}}_0) \\ & + \frac{(1-R_0^2)^2}{4R_0^5}\, \nabla^2 G_{\mathrm{jk}}(\boldsymbol{x}-\bar{\boldsymbol{x}}_0) \Bigg\} + \frac{1-R_0^2}{R_0^4}\, \hat{e}_{\mathrm{k}}\,(\delta_{\mathrm{lm}} - \hat{e}_{\mathrm{l}}\hat{e}_{\mathrm{m}})\, G_{\mathrm{jk},l}(\boldsymbol{x}-\bar{\boldsymbol{x}}_0) \\ & - \frac{3(R_0^2-1)}{R_0^3} \frac{\left(\delta_{\mathrm{jm}} - \hat{e}_{\mathrm{j}}\hat{e}_{\mathrm{m}}\right)}{\bar{r}} + \left(R^2-1\right)(\delta_{\mathrm{km}} - \hat{e}_{\mathrm{k}}\hat{e}_{\mathrm{m}})\, \frac{\partial \varphi_{\mathrm{k}}}{\partial x_{\mathrm{j}}}\,, \end{aligned} \tag{5.3}$$

with

$$\varphi_{\mathrm{k}} = -\frac{3(R_0^2-1)}{2R_0^3}\, \frac{x_{\mathrm{k}}}{\bar{r}}\, \frac{R - \bar{R}_0 \cos\alpha + \bar{r}\cos\alpha}{R\bar{R}_0^2 \sin^2\alpha}\,. \tag{5.4}$$

In the previous equations, R_0 and $\bar{R}_0$ are the Euclidean norms of $\boldsymbol{x}_0$ and its image $\bar{\boldsymbol{x}}_0$, respectively; $\hat{\boldsymbol{e}}$ is the unit vector indicating the axial direction $\hat{\boldsymbol{e}} = \boldsymbol{x}_0/R_0$; $r = |\boldsymbol{x}-\boldsymbol{x}_0|$; $\bar{r} = |\boldsymbol{x}-\bar{\boldsymbol{x}}_0|$; R is the Euclidean norm of $\boldsymbol{x}$; δ_{jm} is the Kronecker delta; α is the angle between $\boldsymbol{x}$ and $\hat{\boldsymbol{e}}$. The numerical implementation of this velocity field is tedious because of the many terms involving partial derivatives which should be computed analytically, thus great care should be taken especially while vectorizing it.

To evolve the filaments configuration in time we use the equations of motion presented in Chapter 4, namely Eqs. (4.7), (4.9) with the appropriate boundary conditions, in which the Green's function is the one for a point force inside a sphere. For a filament subject to a collection of fluid-entraining follower forces, the corresponding equations and boundary conditions are used instead.

Regularization

In order to avoid overestimating the strength of the velocity field in the neighbourhood of the singularity, which may result in erroneous results, a regularization is required. We were not aware of any regularized velocity field for a point force inside a spherical container in the literature. Therefore, we developed an *ad hoc* technique based on excluding the region near the point force and replacing it with an elliptic 'bubble'. The shape of the bubble was chosen to be elliptical because the velocity field is stronger in the direction of the point force and weaker perpendicularly to it. The velocity field evaluated at the points outside the bubble were used to extrapolate the values inside in a way to ensure that the first derivative was continuous and the maximum value was independent on the number of grid points used for

Ratio L/a	σ^*	Σ^*
1.5	22.7	39.8
1.4	26.8	50.2
1.3	31.8	64.3
1.2	38.1	83.7
1.1	46.3	111.6
1	57.1	152.6
0.9	71.8	213.9
0.8	92.4	311.2
0.7	122.7	475.6
0.6	170.1	776.1
0.5	249.5	1389.0

Table 5.1 Summary of the critical values of the control parameters for the onset of self-sustained oscillations when varying the ratio between the filament length and the radius of the sphere. As expected, the larger the ratio, the lower σ^* and Σ^* are.

the simulation, similar to the reasoning in Sec. 3.1.1. This heuristic technique was tested and validated successfully against Cortez's regularized stokeslets in free-space and near the wall [104, 106].

5.2 Results

5.2.1 Role of confinement on a single filament

In the previous chapters, we studied the dynamics of a single filament and a multitude of them in the presence or absence of a hydrodynamic wall. In such instances, the only length scale of the problem was the length L of the filament. Here, the filaments are located inside a spherical container with radius a, and the obvious parameter that enters the problem is the dimensionless ratio L/a.

When simulating the filament dynamics, despite the closed geometry, we still observe the same three regimes as for all the former cases, i.e. the recirculation does not lead to the onset of any new dynamical regime. Depending on σ, we have that the initially perturbed filament returns to a straight configuration, shows oscillations that die out, and undergoes a Hopf bifurcation in which exhibits self-sustained oscillations. To allow a comparison with the previous cases studied, we initially address the question of how confinement affects the onset of the transition for a filament with $L/a = 1$. For this geometry, the critical value of the control parameter is $\sigma^* \approx 57.1$, which stands between $\sigma^* \approx 53.3$ and $\sigma^* \approx 67.7$ referring to

the cases in presence or absence of a flat wall, respectively. When the filament is subject to a fluid-entraining follower force without the wall, the velocity field decays as $\sim 1/r$ with r being the distance from the point force. In the presence of the wall, the flow decays as $\sim 1/r^2$ instead. By inspecting Eq. (5.1), it is possible to identify that the order of r at which the fluid flow created by a point force inside a sphere falls off is a non-integer value between 1-2 because of the presence of the complex image system. This creates a tension on the filament that is lower than the unbounded, but larger than the bounded case, thus explaining the intermediate value of σ^* for the spherical container. Similar conclusions can be drawn for a line distribution of fluid-entraining follower forces where in fact $\Sigma^*_{\text{wall}} < \Sigma^*_{\text{sphere}} < \Sigma^*_{\text{nowall}}$.

When varying the parameter L/a, the qualitative dynamics remain unaltered, but the critical values σ^* and Σ^* of course change, as summarized in Table 5.1. It should be noticed that the analysis carried in Sec. 3.2, which expressed $\sigma^*_{L_0}$ in terms of σ^* and the ratio L/L_0, cannot be extended in this context as the parameter L/a non-trivially modifies the velocity field, and thus the tension on the filament. In fact, the relation $\sigma^*_{L/a} = \sigma^*_{L/a=1}(a/L)^2$ overestimates the critical value when the parameter is greater than one and underestimates it when lower than one.

In the limit case where the radius $a \to \infty$, thus $L/a \to 0$, we would recover the case of a fluid-entraining follower force with wall and obtain the same critical values of the control parameters, σ^* and Σ^*, as in Chapter 3. In fact, we would be left with only one length scale in the system, the filament length L, and the velocity field would be the one of a Stokeslet near a planar wall. Conversely, Table 5.1 shows that for smaller, but finite, L/a ratios, the critical values increase. This is because locating the point forces closer to the wall, in order to satisfy the no-slip boundary condition, the flow must decay fast and larger values of the control parameters are necessary to trigger the instability.

5.2.2 Role of confinement for the multi-filament case

In the following analyses, we only consider an equidistant odd number of filaments, thus a system possessing radial symmetry, with $L/2a = 1/4$, since in the real biological system MTs have a length about a fourth of the oocyte size. Choosing an even number of filaments would lead to filament configurations where the fluid-entraining follower forces would act along the same line but in opposite directions, thus possibly causing cancellation effects. For the sake of completeness, we investigated this instance as well, but here we only report the results for an odd number of filaments for the aforementioned reason.

	σ				
N_{fil}	3	5	7	9	11
✳ return to straight config.	< 245	< 235	< 225	< 205	< 195
✳ synchronized oscillations	245 – 700	235 – 480	225 – 460	205 – 400	195 – 400
✳ independent oscillations	> 700	> 480	> 460	–	–

Table 5.2 Summary of the values at which the system constituted by filaments subject to a single fluid-entraining follower force at their tips transitions to different dynamical regimes.

Single fluid-entraining follower force

We investigate the case where filaments are actuated by a single fluid-entraining follower force at their tips. We simulate the dynamics for an increasing number of filaments and discover the existence of three distinct behaviours (Fig. 5.2). Below a certain value of the control parameter σ, the initial perturbations imposed to the filaments configurations decay, either immediately or after some oscillations. For an intermediate value of σ, the filaments start oscillating independently but, after a transient period, they *synchronize* their beats. When σ is large enough, the filaments beat asynchronously instead.

Table 5.2 summarizes how σ varies with the number of filaments for the three regimes. A visual representation is shown in the centre of Fig. 5.2. We notice that the value of the control parameter for synchronization decreases for larger N_{fil}. This is because the background flow becomes more vigorous, thus enhancing the hydrodynamic coupling. Fig. 5.2a displays the synchronous beat for $N_{\text{fil}} = 9$ and that the phase difference $\Delta\phi$, defined as $\Delta\phi = (\phi_1 - \phi_i)/2\pi$ with $\phi(t) = \theta(1,t) - \theta(0,t)$, vanishes over time. In the case of asynchronous oscillations, $\Delta\phi$ constantly varies in time and each filament beats independently, as presented in Fig. 5.2b for $N_{\text{fil}} = 3$. This is because hydrodynamic coupling is not strong enough compared to the force that actuates the filaments. Despite the closed geometry that intensifies the background flow, the compressive effect of the follower force that leads to self-sustained oscillations dominates over the hydrodynamic force. For $N_{\text{fil}} = 9, 11$, when $\sigma > 400$ the filaments oscillations become wide enough to touch the wall, thus the numeric results lose validity as non-penetration forces are not included in the employed model.

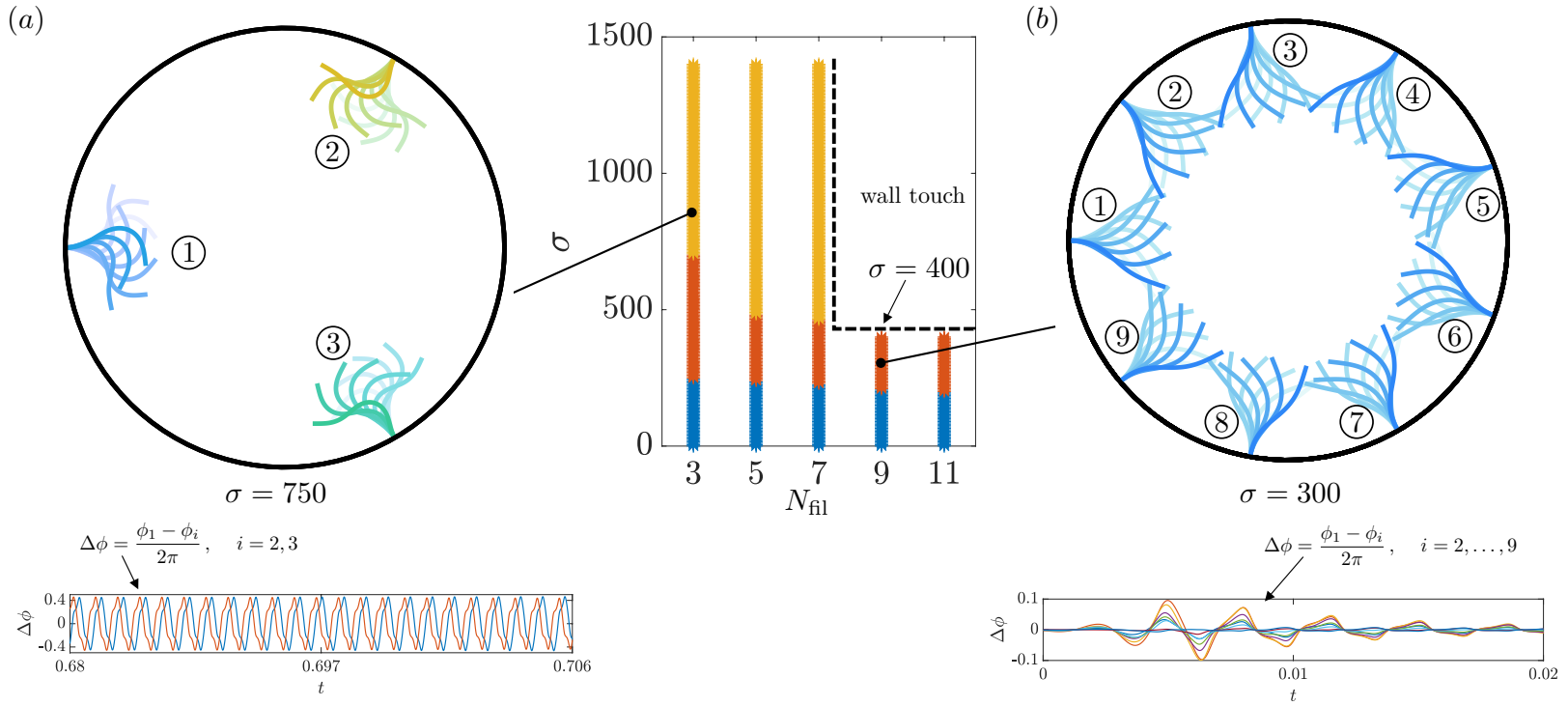

Fig. 5.2 Schematic summarizing the dynamics of filaments inside a sphere actuated by a single fluid-entraining follower force at their tips. Three different regimes can be identified depending on the filament density and the control parameter σ. The colour map used is the same as the one in Table 5.2. (i) The filaments return to their original configuration; (ii) the filaments show oscillations that eventually synchronize after a transient; (iii) the filaments exhibit independent oscillations. The synchronous oscillations are the result of the hydrodynamic coupling. However, if σ is large enough, the oscillations coming from the compressive force dominate over the hydrodynamic interaction thus preventing any synchronization. (a) Asynchronous oscillations for $N_{\text{fil}} = 3$. Clearly, the phase difference $\Delta\phi_i$ constantly changes over time. (b) Synchronous oscillations for $N_{\text{fil}} = 9$. The phase difference vanishes after a transient period.

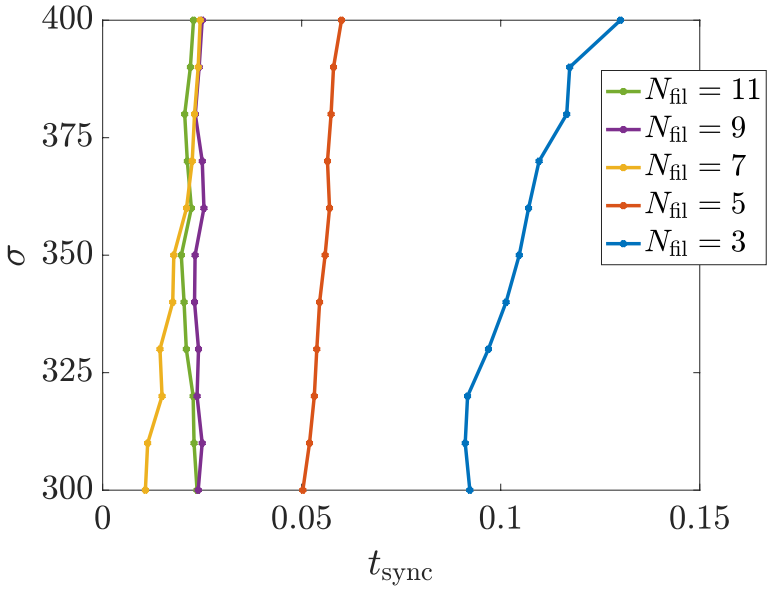

Fig. 5.3 The time for the filaments to synchronize diminishes when the number of filaments increases as the hydrodynamic interactions become more vigorous. The time for synchronization is fairly independent on the control parameter.

Fig. 5.3 shows the time taken by the filaments to synchronize, t_{sync}, increases with σ and decreases with N_{fil}. This is the result of the physical considerations discussed above. In particular, as the control parameter increases, so does the compressive contribution thus leading to longer transients. On the other hand, the presence of more filaments results in a stronger background flow that facilitates synchronization. Interestingly, for $N_{\text{fil}} = 9, 11$, t_{sync} is larger than for the case with $N_{\text{fil}} = 7$. This might be due to the more densely packed filament configuration, whose effect is to induce flows that delay the synchronization.

Line distribution of fluid-entraining follower forces

A much more dynamical problem is the case with a line distribution of fluid-entraining follower forces. This instance presents seven different behaviours depending on both the number of filaments and the strength of the control parameter Σ, as summarized in Table 5.3, whose graphical representation is plotted in Fig. 5.4. Contrary to the single fluid-entraining follower force case, here we separate the regimes in which the filaments return to their straight configuration. The reason for this will become apparent during the analysis.

When $N_{\text{fil}} = 3, 5$, the initial perturbations decay immediately or grow before dying out, reminiscent of the single filament case where the growth rate becomes complex with a negative real part. For larger Σ, the filaments undergo a Hopf bifurcation and start exhibiting

	Σ					
N_{fil}	3	5	7	9	11	13
✳ return to straight config.	< 850	< 550	< 190	< 130	< 115	< 105
✳ oscillations to straight config.	850 – 1340	550 – 1225	1000 – 1100	–	–	–
✳ synchronized oscillations	1340 – 2150	1225 – 2000	1100 – 2085	1310 – 2180	–	–
✳ independent oscillations	> 2150	> 2000	> 2085	> 2180	–	–
✳ bent configuration	–	–	190 – 1000	130 – 1200	115 – 1300	105 – 1400
✳ oscillations to bent config.	–	–	–	1200 – 1310	1300 – 1975	1400 – 2105
✳ metachronal wave	–	–	–	–	> 1975	> 2105

Table 5.3 Depending on the number of filaments and the control parameter Σ, seven dynamical regimes can be observed for filaments subject to a line distribution of fluid-entraining follower forces inside a sphere. Among the possible dynamics, the filaments can bend in the same direction laying down on the sphere's surface.

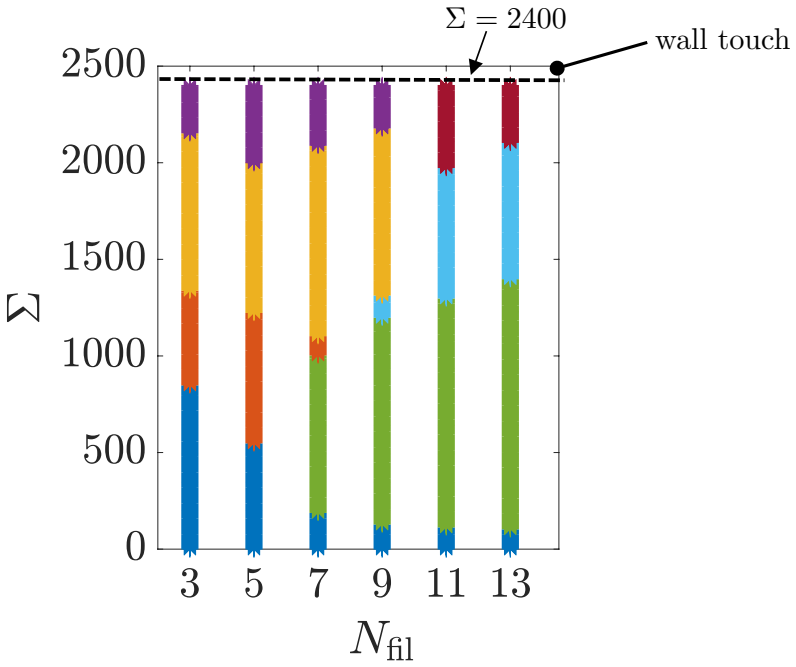

Fig. 5.4 Graphical representation of the possible filament dynamics observed for a line distribution of fluid-entraining follower forces inside a sphere. The same colour map as Table5.3 is used. The regimes are dictated by Σ and the filament density. Namely, the filaments can return to their straight configuration, show decaying oscillations, synchronize, exhibit asynchronous oscillations, reach a bent-steady shape towards the sphere's surface, show oscillations that decay towards the bent-steady shape, and present metachronal waves.

self-sustained oscillations. Because of the hydrodynamic coupling, the filaments eventually synchronize as shown in Fig. 5.5a. When Σ is large enough, the compressive follower forces

dominate over hydrodynamic forces, yielding asynchronous oscillations, similarly to that observed in the previous section.

A new instability occurs for $N_{\text{fil}} \geq 7$. In this case, we observe a *spontaneous symmetry breaking mechanism* in which all the filaments reach an equilibrium configuration where they assume a *steady* bent shape. This instability, that occurs before the filaments start oscillating, is displayed in Fig. 5.5b. We can notice the evident similarity to the MT meshwork observed at stage 11 of *Drosophila* oogenesis. By looking at the evolution of the filaments tip angle, we see that the filaments almost immediately synchronize and then bend simultaneously all together until steadily laying down towards the boundary of the sphere. This phenomenon is a result of the higher filament density. In fact, as the distance between them is smaller, the fluid flow they experience is stronger. The initial perturbations, instead of decaying, amplifies because of this more vigorous background flow, which ultimately lead to the steady bent state. Importantly, when we studied in Sec. 4.3.2 an array of filaments with a line distribution of fluid-entraining follower forces, we observed that they still leaned in the same direction, but assumed different bent shapes. Here, the confinement is crucial as it is responsible for recirculating the fluid flows and rearranging the filaments so that they all reach the same steady configuration. The final filament arrangement is such that a large stationary swirl is created inside the sphere, similar to the fluid flow of a rigid body rotation, visualized in Fig. 5.7a. For this, we define this novel mechanism *swirling instability*.

For $N_{\text{fil}} = 7$, after the steady-bent-shape regime, the filaments show, for increasing σ, (i) oscillations that die out, (ii) synchronous beats, and (iii) asynchronous self-sustained oscillations. For $N_{\text{fil}} = 9$, the initial oscillations, instead of bringing the filament to a straight configuration, decay towards the bent shape. Similar behaviours are observed for $N_{\text{fil}} = 11, 13$ but for a wider range of Σ. This is due to a combination of densely packed filaments and the confinement that establishes a background flow strong enough to amplify the initial perturbations.

Lastly, another regime appears when $N_{\text{fil}} = 11, 13$, namely the onset of pseudo-metachronal waves. As displayed in Fig. 5.5c, the filaments, instead of beating in synchrony, create a wave around the bent shape. We believe that this exotic behaviour is not representative of any real situation since it might be due to the specific filament density, the geometry, and the mathematical model we developed where sliding and /or filaments overlap was neglected.

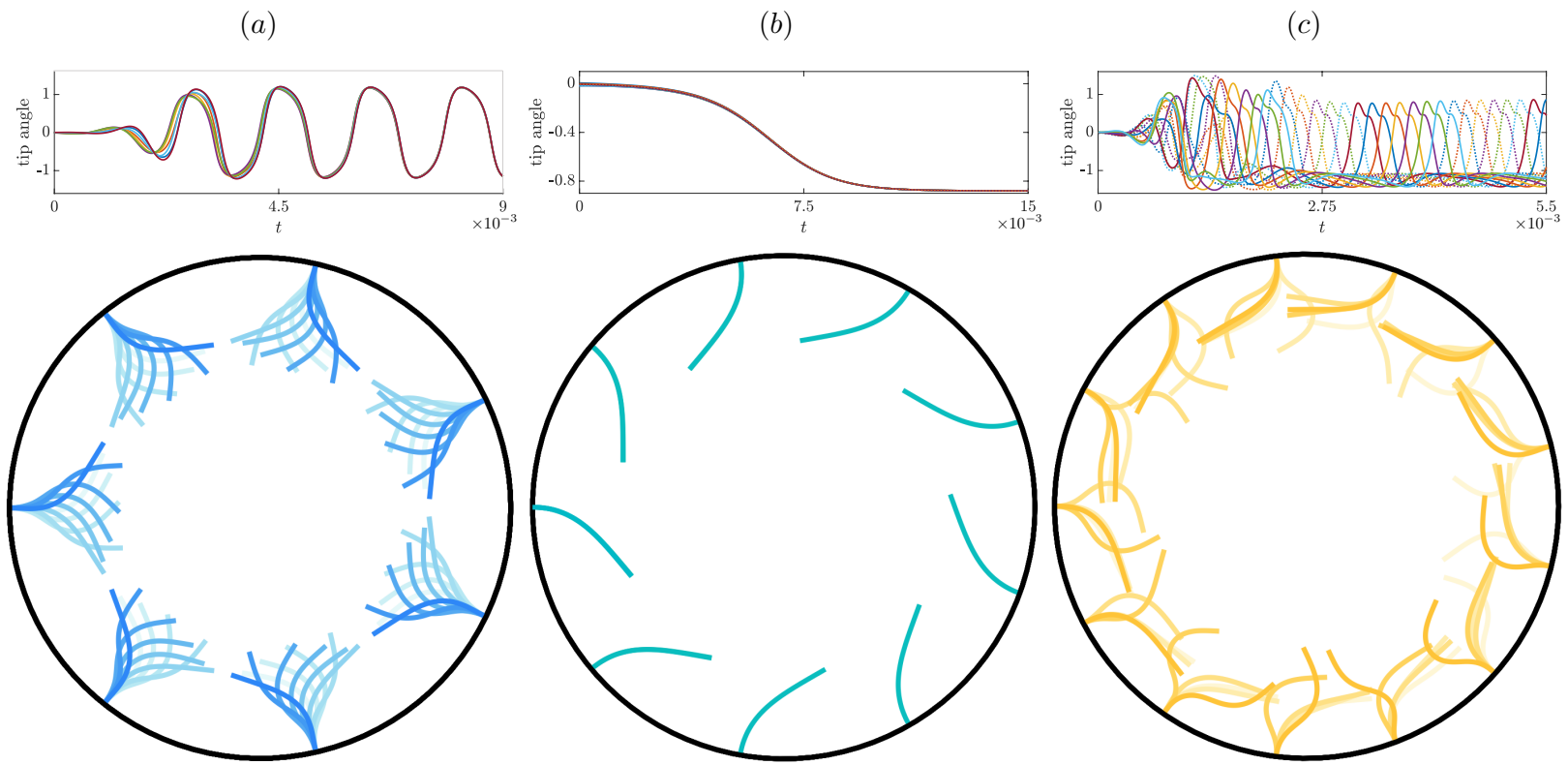

Fig. 5.5 Selected regimes for filaments with line of fluid-entraining follower force. (a) Hydrodynamic interactions allow the filaments beat to synchronize. (b) Before the onset of decaying oscillations, the filaments can reach an equilibrium configuration where they remain steadily bent towards the sphere boundary. This arises consequently to the vigorous background flow that leads to a spontaneous symmetry-breaking mechanism. We term this phenomenon *swirling transition*. (c) When the number of filaments is sufficiently large, the oscillations together with the strong background flow responsible for bending the filaments can couple yielding a regime reminiscent of metachronal waves.

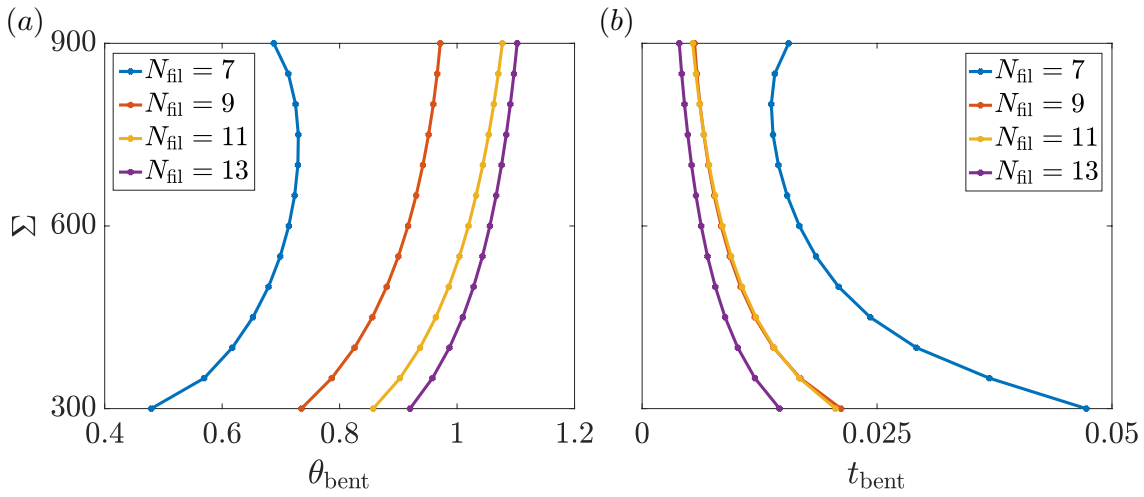

Fig. 5.6 Tip angle of (a) and time for (b) the filaments to reach the final bent shape. Filaments bend more and more swiftly reach a steady-state when the number of filaments increases since the hydrodynamic interactions become more vigorous.

Swirling instability

The swirling instability deserves to be explored in more detail due to its biological relevance. In Fig. 5.6a, we show how Σ affects the final steady bent shape. As expected, for higher filament density and larger values of the control parameter, the time at which the filaments reach the final state, t_{bent}, diminishes, while $\theta_{\text{bent}} = \theta(1, t_{\text{bent}})$ increases (Fig. 5.6). It should be noticed that when $N_{\text{fil}} = 7$, for large Σ, θ_{bent} and t_{bent} diminishes and increases, respectively. This is because it is the only case in which the swirling instability is followed by perturbations that die out to the straight filament case.

As already discussed, after the filaments reach the steady bent configuration, the resulting fluid flow shows a circulatory pattern with the centre of the sphere being a stagnation point (Fig. 5.7a). The velocity field in the x- and y-direction is given in Fig. 5.7b where we see that, as previously mentioned, its strength increases with the number of filaments. We can notice that the fluid flow initially moves towards the centre of the sphere and then towards the boundary before rapidly vanishing to satisfy the no-slip boundary condition.

5.3 Discussion

The chapter builds on the models and findings presented and discussed in the previous parts of this thesis. After regularizing the velocity field for a point force inside a sphere, we simulated the filaments dynamics for the single as well as the line distribution of fluid-entraining

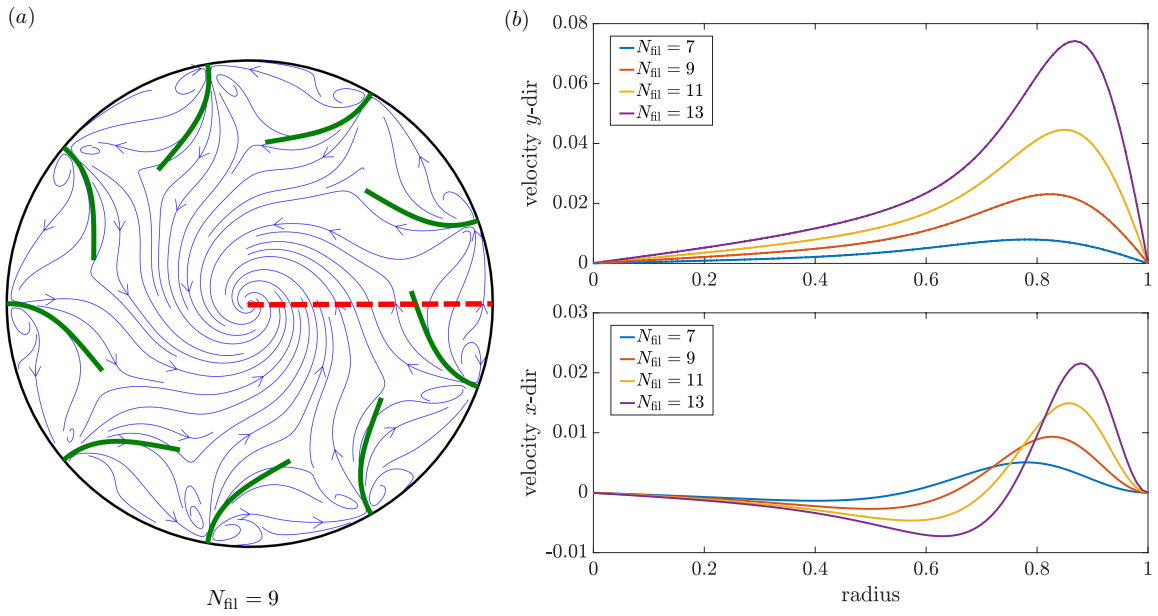

Fig. 5.7 (a) Filaments overlaid with streamlines for swirling instability. The filaments remain steadily bent towards the sphere wall and the anchored fluid-entraining follower forces generate a large swirl, similar to a rigid body rotation, that induces a net flow. (b) Velocity field in x- and y-directions at the red dotted line in (a). The fluid flow moves towards the centre of the sphere creating the swirl, then inverts its direction and moves towards the boundary before rapidly vanishing to satisfy the no-slip boundary condition.

follower forces. We found that the filaments can synchronize for a wide range of values of the control parameters in both cases and that when σ and Σ are large enough, the compressive effect of the actuating forces dominates on the hydrodynamics, leading to asynchronous oscillations.

Importantly, for a line distribution of fluid-entraining follower forces we discovered the existence of a new instability, defined swirling instability, that arises beyond a critical filament density. This instability is characterised by the filaments reaching a bent steady configuration towards the wall of the container and the fluid flow showing a circulatory pattern, qualitatively matching the velocity field and the underlying microtubular meshwork observed at stage 11 of *Drosophila* oogenesis.

The confinement provided the necessary radial symmetry for all the filaments to reach the same bent configuration as opposed to the array-case presented in Sec. 4.3.2. For vanishing L/a, we would recover the planar wall case with periodic boundary conditions. The spherical geometry triggered earlier onsets of the instabilities as the fluid flows generated by the

fluid-entraining follower forces enhanced the compression, thus yielding lower values of the critical control parameters.

In Ch. 1, we presented two open questions about *Drosophila* oogenesis: (i) why MTs undergo waving motion and (ii) what is the physics underlying the transition between stage 9 and 11 in which MTs reorient and the fluid flows show a coherent circulatory motion. For the first query, we discovered that buckling of slender filaments subject to a follower force at low Reynolds number yields to self-sustained oscillations. For the second question, we showed that fluid-structure interactions can lead to a swirling transition and explained the nature of the symmetry breaking mechanism. After progressively developing more sophisticated and accurate models, we now relate these findings to the real biological system.

When we tackled the collective dynamics inside the sphere, we deliberately simulated filaments with $L/2a = 1/4$, this being more representative of *Drosophila*. Using its typical biophysical values (Table 2.1), we find that $\Sigma \approx 600$, thus standing within the range we found numerically to observe the spontaneous symmetry breaking mechanism which led to bent filaments. With regard to the speed of the fluid flow inside the sphere, we find that viscosity plays a key role. Using the values calculated by [1] at stage 9, we obtain a speed of about 20 pm/s, while if we consider that at stage 11 the actin meshwork dissolves and assume that the viscosity of water can be used instead [115], the speed increases of three orders of magnitude, i.e. 20 nm/s. However, this still slightly underestimates the speed measured experimentally that was in the 120-130 nm/s range. Importantly, we showed that the mechanical coupling between the fluid motion and the orientation of the MTs can lead to a transition to coherent, unidirectional motion within the oocyte. The viscosity simply dictates the time scale for the coherent motion to develop. This may mean that the oocyte at stage 9 would be already able to transition but the high viscosity due to the actin filaments significantly slows down the process. Only once the viscosity drops the coherent motion can rapidly develop.

In our numerical experiments, the direction of the bent filaments and, therefore, of the velocity field were just random, depending on the initial conditions: a more perturbed filament would trigger the transition and dictate the chirality of the microtubular meshwork and of the flow. In *Drosophila* it seems that the chirality is also random and that the dorsal-ventral symmetry does not play any role. Our spherical setup omitted any asymmetry in the oocyte shape and showed that the swirling transition can in fact take place regardless.

In the spirit of developing a tractable model, several assumptions and simplifications were made, so it is surprising that the quantitative comparison between our model and the real system showed only a decent agreement. However, this approach allowed us to separate the elements constituting the complex oocyte and focus only on some, so that the underlying physics could be explored and understood. All in all, our fluid-structure interaction model

was able to capture the essence and physics of the waving motion as well as the transition observed in *Drosophila* oogenesis.

Chapter 6

Summary and future directions

The lack of an appropriate mathematical formulation and the biological relevance of the complex dynamics observed at stage 9 and 11 of *Drosophila* oogenesis were the drivers and motivations behind the work presented in this thesis. Two main questions were presented in Chapter 1: (i) why filaments oscillate at stage 9 and (ii) what governs the transition from oscillations to a final steady bent configuration, with a corresponding circulatory fluid motion, at stage 11.

We addressed these questions by developing a mathematical framework with an increasing level of complexity and higher fidelity of the real oocyte. The foundation of the model is a mechanism of fluid-structure interaction at low Reynolds number, inspired by recent experimental work that showed the correlation between the fluid flow and the underlying MT meshwork. With the aim of developing the simplest, yet complete model, we adopted a reductionist approach in which we identified and included only the key features for each element of the oocyte. The molecular motor-cargo ensemble was modelled as a fluid-entraining follower force, i.e. a point force that always acts tangentially and compresses the filament while entraining fluid. The MT was instead approximated by an elastic inextensible filament.

Our investigation started with studying the individual dynamics of a filament acted on by a no-fluid-entraining follower force (a force that only compresses tangentially the filament) located at its tip. We discovered that the dynamics is governed by a control parameter that represents the ratio between the external forcing and the elastic force. Beyond a certain value of such parameter, the filament buckles and undergoes a Hopf bifurcation with the corresponding onset of self-sustained oscillations. We explained the physics of this behaviour with a combination of linear stability analysis and by exploiting a lower dimensional model constituted solely of two rigid links connected by torsion springs. In particular, we showed

that the follower force, which is naturally nonconservative, constantly injects and withdraws energy into the system, thus leading to a self-sustained dynamics.

Molecular motors entrain fluid while moving along MTs. Hence, we extended the model to fluid-entraining follower forces. Since we considered motors walking towards the free end of MTs, the flow they set points in the same direction, thus creating an effective flow-induced tension and delaying the onset of the self-sustained oscillations. Although the details of buckling were quantitatively different in the presence of this induced fluid flow, the physics was essentially the same. We then contextualized our findings in the biological system that inspired this work and concluded that the resulting value of the control parameter was such that the oscillatory behaviour can indeed occur. Our model was therefore able to capture the wave-like motion observed experimentally at stage 9, thus answering the first question.

The more representative instances of the real system where the follower force was not located at the filament tip or a multitude of them were anchored to the filament were also studied. We developed the appropriate theoretical frameworks, which were then numerically implemented, to handle these more challenging cases. Unsurprisingly, the same qualitative dynamics was seen when the point force was at the tip. In summary, buckling of an elastic filament subject to different types, location, and number of follower forces in creeping flows can lead to self-sustained oscillations.

After fully characterizing the individual dynamics, we turned to the multi-filament problem and the study of collective buckling. We initially focused on the dynamics of two parallel filaments anchored at one end with a fluid-entraining follower force at their tip. We showed that the hydrodynamic interactions can lead to robust synchronization independent on the initial perturbations. However, when the filaments were sufficiently far apart, the flow set by the other filament became small and the filaments exhibited asynchronous oscillations instead. The same asynchrony was observed when the control parameter was large enough as the self-induced oscillations would overcome the hydrodynamic coupling. Interestingly, before entering the synchronous regime, for smaller values of the control parameter, the filaments would bend towards each other. This was the result of the flows set by each follower force that entrained fluid and therefore pushed the filaments closer until reaching a stable bent configuration. The same qualitative results were observed for two filaments with a line distribution of fluid-entraining follower forces in the presence of a wall. Different scenarios appeared instead for the no-wall case in which in-phase synchronized oscillations appeared only after a regime characterized by anti-phase oscillations.

In order to tackle the significant computational cost involved in the multi-filament problem, we developed an algorithm that, thanks to the vectorization and the avoidance of ‘for’ loops, was able to reduce the amount of work up to about five times compared to a vectorized

but brute-force-based algorithm. Also, the geometry we exploited (unbounded, bounded by a flat wall and spherical domains) allowed us to take advantage of analytical solutions to calculate the velocity fields, thus by-passing the computational effort to solve Stokes equations. We simulated an array of up to 10 parallel filaments for both a single and a line distribution of fluid-entraining follower forces. The numerical results for the single force showed that the dynamics obtained for the two-filament case reappeared in this set-up, namely the filaments slightly bent towards each other maintaining a mirror symmetry (the farther apart the filament, the more pronounced the bent configuration was), and exhibited (ii) synchronous and (iii) asynchronous oscillations. Richer dynamics were observed for the line distribution of forces. Depending on the filament density, the filaments showed both in-phase and anti-phase synchronized oscillations, the latter arising for larger values of the control parameter, as well as a spontaneous symmetry breaking mechanism, in which they all leaned in the same direction until reaching a steady bent configuration. Such a novel mechanism was caused by the vigorous background flows that entrained the filaments and amplified their initial random perturbations.

Progressively, we further developed our model to resemble the real oocyte more closely. As a last step, we located the filaments inside a spherical container to study how the confinement affects both the individual and collective dynamics. The natural parameter representing the ratio between the filament length and the radius of the sphere was used to determine how the critical value of the control parameter for the onset of the self-sustained oscillations would change. We showed that the complex image system of the analytic solution for a point force inside a sphere was responsible for affecting the control parameter in a nontrivial fashion compared to the case of no-fluid-entraining follower force.

Finally, we focused on the collective buckling inside a sphere. We considered a set-up close to the *Drosophila* oocyte: filaments anchored to the boundary with length equal to a fourth of the sphere radius. When the filaments were subject to a single fluid-entraining follower force at their tips, they could synchronize their oscillations. However, if the control parameter was large enough, the compressive effects would overcome the hydrodynamic interactions, thus preventing the filaments to synchronize. A wider spectrum of scenarios was observed for a line distribution of fluid-entraining follower forces. In fact we identified seven different regimes based on the filaments dynamics, among which the *swirling instability*. In this instability, the filaments, from being slightly perturbed around a straight configuration, would spontaneously bend and lay down towards the surface of the sphere all in the same direction. The system would then reach an equilibrium configuration with the filaments assuming a steady bent shape and the fluid flow exhibiting a circulatory motion, similar to a swirl. Such an instability was the result of the vigorous background flow created by the

fluid-entraining follower forces and the closed domain, which allowed the flows to recirculate, rearranging the filaments configuration. Remarkably, despite the reductionist approach and the simplicity of our model, we showed that the fluid-mechanical coupling between the fluid motion and the orientation of the filaments led to the same transition to coherent motion within the oocyte observed experimentally at stage 11. The typical physical quantities for a *Drosophila* oocyte were used to compare its control parameter and velocity field to our numerical results, providing a decent quantitative agreement.

This thesis shed light on some of the complex dynamics observed during *Drosophila* oogenesis. By using a combination of theory and simulations it made advances in understanding the wave-like motion of MTs and the interplay between the fluid flow and the microtubular meshwork that can lead to the directed motion inside the oocyte observed in experiments. In order to better describe the biological dynamics, possible extensions of this work are based on the following considerations: (i) molecular motors stochastically bind and unbind to the filaments, providing stochasticity to both the long-range forces in the fluid and the localised forces to the filaments; (ii) microtubules undergo rescue and catastrophe events, affecting both the fluid flows and the overall microtubular meshwork; (iii) microtubules move in 3D and are typically found densely packed, hence opening up new potential instabilities. Considering the ubiquity of multi-filament instances in biology where fluid-structure interactions play a key role, we hope that the model and findings presented and discussed here will not only provide a fundamental basis to tackle these extensions for *Drosophila*, but will also stimulate future research on the dynamics of complex systems in biophysics.

References

[1] S. Ganguly, L. S. Williams, I. M. Palacios, and R. E. Goldstein. Cytoplasmic streaming in Drosophila oocytes varies with kinesin activity and correlates with the microtubule cytoskeleton architecture. *Proc. Natl. Acad. Sci. USA*, 109:15109–15114, 2012.

[2] A. N. Becalska and E. R. Gavis. Lighting up mRNA localization in Drosophila oogenesis. *Development*, 136(15):2493–2503, 2009.

[3] J. Howard. *Mechanics of motor proteins and the cytoskeleton*. Sinauer Associates Sunderland, MA, 2001.

[4] B. Alberts, A. Johnson, J. Lewis, M. Raff, K. Roberts, and P. Walter. *Molecular Biology of the Cell, 4th ed.* Garland Science, 2002.

[5] R. D. Vale and R. A. Milligan. The way things move: looking under the hood of molecular motor proteins. *Science*, 288(5463):88–95, 2000.

[6] F. Jülicher, A. Ajdari, and J. Prost. Modeling molecular motors. *Rev. Mod. Phys.*, 69:1269–1282, Oct 1997.

[7] M. Schliwa and G. Woehlke. Molecular motors. *Nature*, 422(6933):759–765, 2003.

[8] F. Gittes, E. Meyhöfer, S. Baek, , and J. Howard. Directional loading of the kinesin motor molecule as it buckles a microtubule. *Biophys. J.*, 70:418–429, 1996.

[9] Y.-N. Young. Dynamics of a semiflexible polar filament in Stokes flow. *Phys. Rev. E*, 82:016309, 2010.

[10] R. E. Isele-Holder, J. Elgeti, and G. Gompper. Self-propelled worm-like filaments: spontaneous spiral formation, structure, and dynamics. *Soft Matter*, 11:7181–7190, 2015.

[11] A. Chaudhuri and D. Chaudhuri. Forced desorption of semiflexible polymers, adsorbed and driven by molecular motors. *Soft Matter*, 12:2157–2165, 2016.

[12] P. Gosselin, H. Mohrbach, I. M. Kulić, and F. Ziebert. On complex, curved trajectories in microtubule gliding. *Physica D*, 318-319:105–111, 2016.

[13] G. Jayaraman, S. Ramachandran, S. Ghose, A. Laskar, M. S. Bhamla, P. B. S. Kumar, and R. Adhikari. Autonomous motility of active filaments due to spontaneous flow-symmetry breaking. *Phys. Rev. Lett.*, 109(15):158302, 2012.

[14] M. J. Shelley. The dynamics of microtubule/motor-protein assemblies in biology and physics. *Ann. Rev. Fluid Mech.*, 48:487–506, 2016.

[15] L. Bourdieu, T. Duke, M. B. Elowitz, D. A. Winkelmann, S. Leibler, and A. Libchaber. Spiral defects in motility assays: a measure of motor protein force. *Phys. Rev. Lett.*, 75:176–179, 1995.

[16] R. D. Allen, D. G. Weiss, J. H. Hayden, D. T. Brown, H. Fujiwake, and M. Simpson. Gliding movement of and bidirectional transport along single native microtubules from squid axoplasm: evidence for an active role of microtubules in cytoplasmic transport. *J. Cell Biol.*, 100(5):1736–1752, 1985.

[17] B. Corti. *Osservazione Microscopiche sulla Tremella e sulla Circulazione del Fluido in Una Planto Acquaguola*. Appresso Giuseppe Rocchi, Lucca, Italy, 1774.

[18] R. E. Goldstein and J.-W. van de Meent. A physical perspective on cytoplasmic streaming. *Interface Focus*, 5:20150030, 2015.

[19] I. Foissner and G. O. Wasteneys. Microtubule disassembly enhances reversible cytochalasin-dependent disruption of actin bundles in characean internodes. *Protoplasma*, 214:33–44, 2000.

[20] F. G. Woodhouse and R. E. Goldstein. Cytoplasmic streaming in plant cells emerges naturally by microfilament self-organization. *Proc. Natl. Acad. Sci. USA*, 110:14132–14137, 2013.

[21] W. E. Theurkauf, S. Smiley, M. L. Wong, and B. M. Alberts. Reorganization of the cytoskeleton during Drosophila oogenesis: implications for axis specification and intercellular transport. *Development*, 115 (4):923–936, 1992.

[22] N. Hirokawa, S. Niwa, and Y. Tanaka. Molecular motors in neurons: transport mechanisms and roles in brain function, development, and disease. *Neuron*, 68:610–638, 2010.

[23] A. M. Arias. Drosophila melanogaster and the development of biology in the 20th century. In *Drosophila*, volume 420 of *Methods in Molecular Biology*, pages 1–25. Humana Press, 2008.

[24] J. B. Glotzer, R. Saffrich, M. Glotzer, and A. Ephrussi. Cytoplasmic flows localize injected oskar RNA in Drosophila oocytes. *Curr. Biol.*, 7(5):326–337, 1997.

[25] A. C. Spradling. Developmental genetics of oogenesis. *The development of Drosophila melanogaster*, 1:1–70, 1993.

[26] B. Alberts, D. Bray, K. Hopkin, A. Johnson, J. Lewis, M. Raff, K. Roberts, and P. Walter. *Essential cell biology*. Garland Science, 2014.

[27] H. Gutzeit and R. Koppa. Time-lapse film analysis of cytoplasmic streaming during late oogenesis of Drosophila. *J. Embryol. Exp. Morph.*, 67(1):101–111, 1982.

[28] W. E. Theurkauf. Premature microtubule-dependent cytoplasmic streaming in cappuccino and spire mutant oocytes. *Science*, 265(5181):2093–2096, 1994.

[29] I. M. Palacios and D. St. Johnston. Kinesin light chain-independent function of the kinesin heavy chain in cytoplasmic streaming and posterior localisation in the Drosophila oocyte. *Development*, 129(23):5473–5485, 2002.

[30] M. K. Gardner, M. Zanic, and J. Howard. Microtubule catastrophe and rescue. *Curr. Opin. Cell Biol.*, 25(1):14–22, 2013.

[31] J. Howard and A. A. Hyman. Dynamics and mechanics of the microtubule plus end. *Nature*, 422(6933):753, 2003.

[32] D. Fygenson, E. Braun, and A. Libchaber. Phase diagram of microtubules. *Phys. Rev. E*, 50(2):1579, 1994.

[33] J. Brugues, V. Nuzzo, E. Mazur, and D. J. Needleman. Nucleation and transport organize microtubules in metaphase spindles. *Cell*, 149(3):554–564, 2012.

[34] J.-M. Kugler and P. Lasko. Localization, anchoring and translational control of oskar, gurken, bicoid and nanos mRNA during Drosophila oogenesis. *Fly*, 3(1):15–28, 2009.

[35] A. Ephrussi, L. K. Dickinson, and R. Lehmann. Oskar organizes the germ plasm and directs localization of the posterior determinant nanos. *Cell*, 66(1):37–50, 1991.

[36] A. Ephrussi and R. Lehmann. Induction of germ cell formation by oskar. *Nature*, 358(6385):387–392, 1992.

[37] E. R. Gavis and R. Lehmann. Localization of nanos RNA controls embryonic polarity. *Cell*, 71(2):301–313, 1992.

[38] F. S. Neuman-Silberberg and T. Schüpbach. The Drosophila dorsoventral patterning gene gurken produces a dorsally localized RNA and encodes a TGFα-like protein. *Cell*, 75(1):165–174, 1993.

[39] C. Wang, L. K. Dickinson, and R. Lehmann. Genetics of nanos localization in Drosophila. *Dev. Dynam.*, 199(2):103–115, 1994.

[40] E. R. Gavis, S. Chatterjee, N. R. Ford, and L. J. Wolff. Dispensability of nanos mRNA localization for abdominal patterning but not for germ cell development. *Mech. Develop.*, 125(1):81–90, 2008.

[41] D. T. Bergstralh and D. St. Johnston. Epithelial cell polarity: what flies can teach us about cancer. *Essays Biochem.*, 53(1):129–140, 2012.

[42] W. E. Theurkauf, S. Smiley, M. L. Wong, and B. Alberts. Reorganization of the cytoskeleton during Drosophila oogenesis: implications for axis specification and intercellular transport. *Development*, 115(4):923–936, 1992.

[43] B.-J. Cha, L. R. Serbus, B. S. Koppetsch, and W. E. Theurkauf. Kinesin i-dependent cortical exclusion restricts pole plasm to the oocyte posterior. *Nature cell biology*, 4(8):592–598, 2002.

[44] R. M. Parton, R. S. Hamilton, G Ball, L. Yang, C. F. Cullen, W. Lu, H. Ohkura, and I. Davis. A PAR-1–dependent orientation gradient of dynamic microtubules directs posterior cargo transport in the Drosophila oocyte. *J. Cell Biol.*, 194(1):121–135, 2011.

[45] L. R. Serbus, B.-J. Cha, W. E. Theurkauf, and W. M. Saxton. Dynein and the actin cytoskeleton control kinesin-driven cytoplasmic streaming in Drosophila oocytes. *Development*, 132(16):3743–3752, 2005.

[46] W. Thielicke and E. Stamhuis. PIVlab-time-resolved digital particle image velocimetry tool for matlab. *Published under the BSD license, programmed with MATLAB*, 7(0.246):R14, 2010.

[47] T. T. Weil, K. M. Forrest, and E. R. Gavis. Localization of bicoid mRNA in late oocytes is maintained by continual active transport. *Dev. Cell*, 11(2):251 – 262, 2006.

[48] K. S. Sinsimer, R. A. Jain, S. Chatterjee, and E. R. Gavis. A late phase of germ plasm accumulation during Drosophila oogenesis requires lost and rumpelstiltskin. *Development*, 138(16):3431–3440, 2011.

[49] G. K. Batchelor. The stress system in a suspension of force-free particles. *J. Fluid Mech.*, 41(3):545–570, 1970.

[50] C. Pozrikidis. *Boundary integral and singularity methods for linearized viscous flow*. Cambridge University Press, 1992.

[51] C. Pozrikidis. *Introduction to theoretical and computational fluid dynamics*. Oxford university press, 2011.

[52] S. Kim and S. J. Karrila. *Microhydrodynamics: principles and selected applications*. Courier Corporation, 2013.

[53] J. Gray and G.J. Hancock. The propulsion of sea-urchin spermatozoa. *J. Exp. Biol.*, 32(4):802–814, 1955.

[54] G. K. Batchelor. Slender-body theory for particles of arbitrary cross-section in Stokes flow. *J. Fluid Mech.*, 44(3):419–440, 1970.

[55] R. G. Cox. The motion of long slender bodies in a viscous fluid. Part 1. General theory. *J. Fluid Mech.*, 44(04):791–810, 1970.

[56] R. E. Johnson. An improved slender-body theory for Stokes flow. *J. Fluid Mech.*, 99(2):411–431, 1980.

[57] J. Lighthill. Flagellar hydrodynamics. *SIAM Rev.*, 18(2):161–230, 1976.

[58] A. T. Chwang and T. Y. T. Wu. Hydromechanics of low-Reynolds-number flow. 2. Singularity method for Stokes flows. *J. Fluid Mech.*, 67:787–815, 1975.

[59] E. Lauga and T.R. Powers. The hydrodynamics of swimming microorganisms. *Rep. Prog. Phys.*, 72(9):096601, 2009.

[60] J. B. Keller and S. Rubinow. Slender-body theory for slow viscous flow. *J. Fluid Mech.*, 75(4):705–714, 1976.

[61] G. J. Hancock. The self-propulsion of microscopic organisms through liquids. In *P. Roy. Soc. A-Math. Phy.*, volume 217, pages 96–121. The Royal Society, 1953.

[62] L. D. Landau and E. M. Lifshitz. *Theory of Elasticity, vol. 7*. Elsevier, New York, 1986.

[63] B. Audoly and Y. Pomeau. *Elasticity and geometry: from hair curls to the non-linear response of shells*. Oxford University Press, 2010.

[64] R. E. Goldstein and S. A. Langer. Nonlinear dynamics of stiff polymers. *Phys. Rev. Lett.*, 75(6):1094, 1995.

[65] S. Timoshenko and J. M. Gere. *Theory of Elastic Stability, 2ed.* Tata McGraw-Hill Education, 1970.

[66] J. F. Brady and G. Bossis. Stokesian dynamics. *Ann. Rev. Fluid Mech.*, 20(1):111–157, 1988.

[67] S. Klumpp and R. Lipowsky. Cooperative cargo transport by several molecular motors. *Proc. Natl. Acad. Sci. USA*, 102(48):17284–17289, 2005.

[68] C. Leduc, O. Campàs, K. B. Zeldovich, A. Roux, P. Jolimaitre, L. Bourel-Bonnet, B. Goud, J.-F. Joanny, P. Bassereau, and J. Prost. Cooperative extraction of membrane nanotubes by molecular motors. *Proc. Natl. Acad. Sci. USA*, 101(49):17096–17101, 2004.

[69] C. B. Korn, S. Klumpp, R. Lipowsky, and U. S. Schwarz. Stochastic simulations of cargo transport by processive molecular motors. *J. Chem. Phys.*, 131(24):12B624, 2009.

[70] K. Svoboda, C. F. Schmidt, B.J. Schnapp, and S. M. Block. Direct observation of kinesin stepping by optical trapping interferometry. *Nature*, 365(6448):721, 1993.

[71] A. F. Huxley. Muscle structure and theories of contraction. *Prog. Biophys. Biophys. Chem*, 7:255–318, 1957.

[72] K. Svoboda and S. M. Block. Force and velocity measured for single kinesin molecules. *Cell*, 77(5):773–784, 1994.

[73] T. Guérin, J. Prost, P. Martin, and J.-F. Joanny. Coordination and collective properties of molecular motors: theory. *Curr. Opin. Cell Biol.*, 22(1):14–20, 2010.

[74] F. Jülicher and J. Prost. Cooperative molecular motors. *Phys. Rev. Lett.*, 75(13):2618, 1995.

[75] P. Khuc-Trong, H. Doerflinger, J. Dunkel, D. St. Johnston, and R. E. Goldstein. Cortical microtubule nucleation can organise the cytoskeleton of Drosophila oocytes to define the anteroposterior axis. *eLife*, 4, 2015.

[76] I. Drechsler, M. Palacios. Private communication. 2015.

[77] C. Kural, H. Kim, S. Syed, G. Goshima, V.I. Gelfand, and P.R. Selvin. Kinesin and dynein move a peroxisome in vivo: a tug-of-war or coordinated movement? *Science*, 308(5727):1469–1472, 2005.

[78] M. Müller, S. Klumpp, and R. Lipowsky. Tug-of-war as a cooperative mechanism for bidirectional cargo transport by molecular motors. *Proc. Natl. Acad. Sci. USA*, 105(12):4609–4614, 2008.

[79] D. Houtman, I. Pagonabarraga, C. P. Lowe, A. Esseling-Ozdoba, A. Emons, and E. Eiser. Hydrodynamic flow caused by active transport along cytoskeletal elements. *EPL-Europhys. Lett.*, 78(1):18001, 2007.

[80] A. Laskar and R. Adhikari. Filament actuation by an active colloid at low Reynolds number. *New J. Phys.*, 19:033021, 2017.

[81] G. Herrmann and R. W. Bungay. On the stability of elastic systems subjected to nonconservative forces. *J. Appl. Mech.*, 31:435–440, 1964.

[82] M. A. Langthjem and Y. Sugiyama. Dynamic stability of columns subjected to follower loads: a survey. *J. Sound Vib.*, 238:809–851, 2000.

[83] I. Elishakoff. Controversky associated with the so-called “follower forces": critical overview. *Appl. Mech. Rev.*, 58:117–142, 2005.

[84] P. V. Bayly and S. K. Dutcher. Steady dynein foces induce flutter instability and propagating waves in mathematical models of flagella. *J. R. Soc. Interface*, 13:20160523, 2016.

[85] F. Gittes, B. Mickey, J. Nettleton, and J. Howard. Flexural rigidity of microtubules and actin filaments measured from thermal fluctuations in shape. *J. Cell Biol.*, 120(4):923–934, 1993.

[86] O. S. Pak, W. Gao, J. Wang, and E. Lauga. High-speed propulsion of flexible nanowire motors: Theory and experiments. *Soft Matter*, 7(18):8169–8181, 2011.

[87] R. E. Johnson and C. J. Brokaw. Flagellar hydrodynamics. A comparison between resistive-force theory and slender-body theory. *Biophys. J.*, 25(1):113–127, 1979.

[88] C. H. Wiggins and R. E. Goldstein. Flexive and propulsive dynamics of elastica at low Reynolds number. *Phys. Rev. Lett.*, 80(17):3879, 1998.

[89] C. H. Wiggins, D. Riveline, A. Ott, and R. E. Goldstein. Trapping and wiggling: Elastohydrodynamics of driven microfilaments. *Biophys. J.*, 74(2):1043–1060, 1998.

[90] V. Kantsler and R. E. Goldstein. Fluctuations, dynamics, and the stretch-coil transition of single actin filaments in extensional flows. *Phys. Rev. Lett.*, 108(3):038103, 2012.

[91] Y.-N. Young and M. J. Shelley. Stretch-coil transition and transport of fibers in cellular flows. *Phys. Rev. Lett.*, 99(5):058303, 2007.

[92] L. E. Becker and M. J. Shelley. Instability of elastic filaments in shear flow yields first-normal-stress differences. *Phys. Rev. Lett.*, 87(19):198301, 2001.

[93] A. Iserles. *A first course in the numerical analysis of differential equations*. Cambridge University Press, 1996.

[94] N. Quennouz, M. J. Shelley, O. du Roure, and A. Lindner. Transport and buckling dynamics of an elastic fibre in a viscous cellular flow. *J. Fluid Mech.*, 769:387–402, 2015.

[95] C. Brennen and H. Winet. Fluid mechanics of propulsion by cilia and flagella. *Annu. Rev. of Fluid Mech.*, 9(1):339–398, 1977.

[96] D. Bigoni. *Nonlinear solid mechanics: bifurcation theory and material instability*. Cambridge University Press, 2012.

[97] L. Guglielmini, A. Kushwaha, E. S. G. Shaqfeh, and H. A. Stone. Buckling transitions of an elastic filament in a viscous stagnation point flow. *Phys. Fluids*, 24(12):123601, 2012.

[98] M. Deng, L. Grinberg, B. Caswell, and G. E. Karniadakis. Effects of thermal noise on the transitional dynamics of an inextensible elastic filament in stagnation flow. *Soft matter*, 11(24):4962–4972, 2015.

[99] L. Euler. *Methodus lnveniendi Lineas Curvas Maximi Minimive Proprietate Gaudentes (Appendix, De curvis elasticis)*. Lausanne and Geneva: Marcum Michaelem Bousquet, 1774.

[100] M. Beck. Die knicklast des einseitig eingespannten, tangential gedrückten stabes. *Z. Angew. Math. Phys.*, 3(3):225–228, 1952.

[101] H. Ziegler. Die stabilitätskriterien der elastomechanik. *Arch. Appl. Mech.*, 20(1):49–56, 1952.

[102] J. R. Dormand and P. J. Prince. A family of embedded Runge-Kutta formulae. *J. Comput. Appl. Math.*, 6(1):19–26, 1980.

[103] R. Cortez. The method of regularized Stokeslets. *SIAM J. Scientific Comp.*, 23(4):1204–1225, 2001.

[104] J. Ainley, S. Durkin, R. Embid, P. Boindala, and R. Cortez. The method of images for regularized Stokeslets. *J. Comput. Phys.*, 227:4600–4616, 2008.

[105] J. R. Blake and A. T. Chwang. Fundamental singularities of viscous-flow. Part 1. Image systems in vicinity of a stationary no-slip boundary. *J. Eng. Math.*, 8:23–29, 1974.

[106] R. Cortez and D. Varela. A general system of images for regularized Stokeslets and other elements near a plane wall. *J. Comput. Phys.*, 285:41–54, 2015.

[107] U. M. Ascher, S. J. Ruuth, and B. T. R. Wetton. Implicit-explicit methods for time-dependent partial differential equations. *SIAM J. Numer. Anal.*, 32(3):797–823, 1995.

[108] E. Nazockdast, A. Rahimian, D. Needleman, and M. Shelley. Cytoplasmic flows as signatures for the mechanics of mitotic positioning. *Mol. Biol. Cell*, 28(23):3261–3270, 2017.

[109] E. Nazockdast, A. Rahimian, D. Zorin, and M. Shelley. A fast platform for simulating semi-flexible fiber suspensions applied to cell mechanics. *J. Comput. Phys.*, 329:173–209, 2017.

[110] C. Pozrikidis. *Numerical computation in science and engineering*, volume 6. Oxford University Press, 1998.

[111] L. Greengard and V. Rokhlin. A fast algorithm for particle simulations. *J. Comput. Phys.*, 73(2):325 – 348, 1987.

[112] L. Greengard and Z. Gimbutas. STFMMLIB3D software, 2012.

[113] C. W. Oseen. *Hydrodynamik*. Mathematik und ihre anwendungen in monographien und lehrbüchern. Akad. Verl.-Ges., 1927.

[114] C. Maul and S. Kim. Image systems for a Stokeslet inside a rigid spherical container. *Phys. Fluids*, 6:2221–2223, June 1994.

[115] A. Mogilner and A. Manhart. Intracellular fluid mechanics: Coupling cytoplasmic flow with active cytoskeletal gel. *Ann. Rev. Fluid Mech.*, 50(1):347–370, 2018.